Development of Pixelated HgI_2 Radiation Detectors for Room Temperature Gamma-Ray Spectroscopy

by

James E. Baciak

A dissertation submitted in partial fulfillment
of the requirements for the degree of
Doctor of Philosophy
(Nuclear Engineering & Radiological Sciences)
in The University of Michigan
2004

Doctoral Committee:

Professor Zhong He, Chairperson
Professor Ronald Fleming
Professor W. Leslie Rogers
Professor David K. Wehe

For my grandfathers, Richard Trudgeon
and Sigmund Zychowski

Acknowledgments

First and foremost I would like to thank my advisor, Professor Zhong He, for his neverending support. He always tried to keep me focused on the goals and helped me keep in mind the overall "big picture" of this work. I would have never accomplished this without his encouragement. We may have never won a coveted water bottle from AASA, but we sure had fun trying.

I would also like to thank my other committee members (Professor Ronald Fleming, Professor W. Leslie Rogers, and Professor David K. Wehe) for taking time out of their busy schedules to help me complete my dissertation and Ph.D. work. Their guidance and support were greatly appreciated. Thanks are also due to my fellow students, both former and current, including Dr. Wen Li, Dr. Yanfeng Du, Dr. Clair Sullivan, Carolyn Lehner, Feng Zhang, Dan Xu, Ben Sturm and Scott Kiff. They provided a great deal of positive support and assistance to this work.

Appreciation goes out to Professor Zhong He, Professor David K. Wehe, and Professor Donald P. Umstatder. I would not have chosen to start a career as a university faculty member if it was not for the opportunities they gave me to experience teaching at a university level. A special thanks goes to Professor Glenn F. Knoll for not only his encouragement over the years, but also for introducing me to Professor Zhong He. Thanks goes to all of the other department faculty and staff, as everyone has helped me in one way or another.

Finally, thanks goes to Dr. Scott Kovaleski and Dr. Steve Shannon for encouraging me to stay at the University of Michigan for graduate studies, and for the many tasty beverages. Last, and certainly not least, I would like to thank my parents for their love and support, and for always helping me through the tough times.

The research was supported in part by Constellation Technologies, Incorporated of Largo, Florida. The support was greatly appreciated.

Contents

List of Figures

List of Tables

Chapter 1

INTRODUCTION

There are several characteristics for an ideal gamma-ray radiation detector. An ideal detector should have high energy resolution for spectroscopy purposes, high gamma-ray detection efficiency to reduce the time required to collect spectra, and low operational costs. Scintillator crystals can operate at room temperature with good detection efficiency, but suffer from poor energy resolution due to the large mean energy required to produce one photoelectron in the photomultiplier tube. Semiconductor detectors, such as silicon, can achieve high energy resolution, but suffer from lower detection efficiency due to relatively low atomic numbers and small detector size. High purity germanium detectors can provide higher detection efficiency for higher energy gamma-rays, but must be operated at liquid nitrogen temperatures due to the small bandgap of Ge. An ideal semiconductor material would have high density, high atomic number, and a large bandgap such that room temperature operation is possible without a degradation in energy resolution.

1.1 Room Temperature Semiconductor Detector Materials

Several semiconductor materials have been investigated for the potential use as a radiation detector that can operate at room temperature. There are three compound semiconductor materials that currently receive extensive attention as potential gamma-ray spectrometers that can operate with no cooling while detecting gamma-rays several hundred keV to a few MeV in energy: mercuric iodide (HgI_2), cadmium telluride (CdTe), and cadmium zinc telluride (CZT). Table 1.1 shows the properties of these materials (atomic number, density, bandgap, average energy to

Table 1.1: Properties of Selected Materials for Room Temperature Gamma-Ray Spectroscopy

Detector Material	Atomic Number	density (g/cm^3)	bandgap (eV)	W (eV/e-h)	$(\mu\tau)_e$ (cm^2/V)	$(\mu\tau)_h$ (cm^2/V)
HgI_2	80,53	6.4	2.13	4.2	10^{-4}	4×10^{-5}
CdZnTe	48,30,52	6.1	1.7	4.7	10^{-3}	3×10^{-5}
CdTe	48,52	6.1	1.5	4.4	10^{-3}	5×10^{-5}
PbI_2	82,53	6.2	2.3	4.9	8×10^{-6}	10^{-7}
TlBr	81,35	7.6	2.7	6.5	4×10^{-6}	1.2×10^{-5}

create an electron-hole pair (W), and the charge carrier $\mu\tau$ products), along with two other room-temperature semiconductor materials, lead iodide (PbI_2) and thallium bromide (TlBr) [1] [2] [3].

While wide band-gap, high density, and high atomic number gives us a potential detector material, other properties may inhibit the material from becoming an effective radiation detector. In semiconductor detectors, the mobility-lifetime product ($\mu\tau$) determines the efficiency at which the charge generated in the detector can be collected. Charge collection efficiency can be improved by increasing the bias (electric field) applied to the detector. However, increasing the bias will increase the leakage current and noise of the detector, which is determined by the resistivity of the material. Crystal nonuniformity can also have an effect on charge transportation properties of the detector, thus changing the signal produced by the detector with the location of the interaction. This can affect the size of the detector that can be reasonably constructed.

CdTe detectors have been studied for years and have a resistivity on the order of 10^8-10^9 Ω-cm [4]. This detector material has been reported to yield energy resolutions of approximately 1.2% FWHM (7.9 keV) [5] for a ^{137}Cs gamma-ray source (662 keV). However, polarization in CdTe detectors [6] [7] has limited the use of the material. The lower resistivity of the material limits the electric field that can be applied to CdTe detectors. CdZnTe detectors, on the other hand, are relatively new to the gamma-ray spectroscopy field. This material has higher resistivity (10^{10}-10^{11} Ω-cm [2]) and a larger bandgap than CdTe. CdZnTe detectors do not show

polarization effects and single crystals can be grown several cubic centimeters in volume [8]. CdZnTe has become a very promising material in room temperature gamma-ray spectroscopy and has received much research attention over the past several years.

The large bandgap of HgI_2 (2.1 eV) means the detector crystals of this material have the highest resistivity(10^{12}-10^{13} Ω-cm) compared to CdTe and CdZnTe. Thus, HgI_2 can withstand very high electric fields. However, the poor hole mobility-lifetime product of HgI_2 and polarization effects can degrade detector performance [9]. Thus, in order to achieve better detector performance in HgI_2, several problems need to be addressed: charge trapping, material non-uniformity, and polarization.

1.2 Charge Trapping

High detection efficiency requires that thick detectors (1 cm or more) be used. However, all current room temperature semiconductor detectors suffer from poor hole transportation properties, so thick detectors generally suffer from degradation of signals from hole trapping. Thus, energy spectroscopy in room temperature semiconductor detectors can be poor, particularly for higher energy gamma-rays, where the interaction locations are spread throughout the detector. The more a signal must rely on hole movement within these detectors, the poorer the signal generated by the detector. There have been several techniques created to compensate for severe hole trapping via pulse rise time compensation [10] [11] [12] [13]. These techniques measure the pulse rise time after a gamma-ray interaction and compensate for losses in the signal generated. While these techniques have shown that improvement in energy resolution can be achieved, the results generally show a loss in active volume contributing to spectra due to the poor signals for gamma-ray events near the anode. Pulse compensation techniques cannot overcome a poor signal to noise ratio. Another technique developed within the past decade, single-polarity charge sensing, has shown that it may be able to overcome the hole trapping problem more effectively than pulse rise time compensation.

Single-polarity charge sensing overcomes the problem of severe hole trapping

by attempting to generate a signal that is independent of the depth of interaction from only the movement of electrons in the detector, similar to a Frisch grid [14] used with gas detectors. This technique has very little, if any, dependency on hole movement. In order to use single-polarity charge sensing on semiconductor detectors, the electrodes must be designed with particular geometries. The first attempt at single-polarity charge sensing in room temperature semiconductor devices was performed on CdZnTe in 1994 [15] [16]. The anode of these detectors was the coplanar design, whereby two sets of anode strips were interlaced with each other. By applying a small potential difference (much smaller than the bias applied to the cathode) between the coplanar anodes, one set of anodes will collect all of the electrons generated by the gamma-ray interaction. By reading out the difference of the signals on the two anodes, a signal is generated that is only dependent on the number of electrons that are collected by the anode. Thus, the problems of hole trapping and position dependence of the signal is avoided.

Another technique developed for single-polarity charge sensing was created in 1995 [17]. This technique involves creating a device where the size of the anode is much smaller than the detector thickness. The signal created by the anode pixel is mostly dependent on the number of electrons collected by the pixel and by movement of charge near the pixel. This technique has shown much promise on room temperature semiconductor devices despite poor hole movement within the detectors [18].

Several other techniques have attempted to make use of single-polarity charge sensing, but with limited success compared to the coplanar and pixelated anode designs. Hemispherical detectors [19] have a small anode surrounded by a cathode on the outer boundary of the half sphere. Frisch grid semiconductor detectors [20] [21] have a small set of electrodes near the anode that are biased slightly lower than the anode and will act similar to a Frisch grid in gas detectors. Cubic semiconductor detectors with an extended cathode on the sides of the detector have also been designed [22].

While single-polarity charge sensing eliminates the need to collect the holes,

electron trapping in room temperature semiconductor detectors still poses a problem. This is particularly important as the detector thickness increases. Thus, variations in the anode signal that are dependent upon the interaction location can still exist and these will cause the energy resolution of the detector to degrade, particularly for high energy gamma-rays. There are solutions to the electron trapping problem in single-polarity charge sensing radiation detectors. One method used with coplanar anodes involves the use of an adjustable gain between the collecting and non-collecting anode signals [15]. By adjusting the gain on the non-collecting anode prior to subtracting the signals, an average amount of electronic trapping is compensated. Improvements in gamma-ray spectroscopy of pixelated detectors have been performed by varying the detector bias and optimizing the amount of electron trapping to compensate for hole trapping [23]. Another solution to electron trapping is to use the depth of the gamma-ray interaction and correct the pulse for electron trapping [24]. Here, the signal for the anode (either coplanar or pixel) and the conventional planar cathode are read out simultaneously. By measuring the cathode to anode signal ratio (C/A ratio) the depth of interaction is determined and the signal can be corrected for electron trapping. Energy resolutions of 1.8% FWHM and 1.2% FWHM at 662 keV have been achieved for a 1 cm^3 CdZnTe detector with coplanar and pixelated anode designs, respectively [25] [18].

1.3 Material Non-Uniformity and Polarization

While single-polarity charge sensing has shown significant improvement over conventional readout techniques, the energy resolution on large volume semiconductor detectors can also suffer due to the quality of the crystal material. Defects and crystal non-uniformity will cause signals to fluctuate with interaction location and degrade energy resolution [26]. For coplanar anode detectors, correcting for material defects is nearly impossible since the actual 3-dimensional location of the interaction is not determined. Pixelated anode devices, along with depth sensing via the C/A ratio, can provide the actual 3-D location of a gamma-ray interaction [27]. By measuring the 3-D interaction of each gamma-ray event, the single detectors

can be broken up into many small virtual voxels and individual energy spectra can be measured from each voxel. Thus, the 3-D variation in each spectrum can measure the 3-D variations in detector response (electron trapping, material non-uniformity, and variations in single-polarity charge sensing within the detector). These variations can then be corrected, and the performance of semiconductor detectors with pixelated anodes can be improved. Another approach in pixelated detectors measures the electron drift time within the detector, since the drift time has a monotonic relationship with the depth of interaction [28]. This technique has provided similar results to the C/A ratio technique. In general, 3-D pixelated detectors should perform better than coplanar anode detectors of the same size and thickness. Fully pixelated anode CdZnTe detectors (1 cm^3 with an 11 $\times$ 11 grid of anode pixels) have yielded resolutions of approximately 1.5% FWHM at 662 keV.

Polarization produces a change in detector response as a function of time. Generally, polarization is due to the buildup of space charge in the detector from the trapping of holes and electrons, and will lead to a degradation in detector performance [29] [9]. There are many causes of polarization, including the detrapping of holes from deep-level traps, formation of dead layers, diffusion of impurities in the detector, variations in space charge that can alter the electric field, and fabrication damage among others [30]. If the polarization effects are due to the trapping of holes and electrons, increasing the detector bias may reduce these effects. When the polarization effect is slow compared with the total measurement time, the effect on the gamma-ray spectrum may only be slight and it may be possible to correct for it with proper calibration.

1.4 HgI_2 as a Room Temperature Radiation Detector

Mercuric iodide has been studied for three decades as a potential radiation detector. HgI_2 was first applied as a gamma-ray spectrometer by Willig in 1971 [31]. The high atomic numbers of mercury and iodine make the material very attractive for gamma-ray detection as does the bandgap, making room temperature operation possible. Both high energy gamma-ray [32] and x-ray spectra [33] have been ob-

tained. The performance at detecting ultra-low energy x-rays (few keV) has also been studied [34]. A 0.5 mm thick device has achieved an energy resolution of 0.6% FWHM at 662 keV [35]. The high stopping power and linearity of HgI_2 interested others in developing intelligent spectrometers [36] and imaging devices [37] [38] with imaging resolutions on the order of 1-2 mm.

In addition, HgI_2 has been investigated as a possible charged particle detector. This material has yielded energy resolutions around 10% for high energy H and He ions [39]. HgI_2 has also been proposed as a neutron detector [40]. ^{199}Hg has a thermal neutron capture cross section ($\sigma_\gamma(Hg)$) around 380 barns, and releases a 370 keV gamma-ray via an (n,γ) reaction. Since ^{199}Hg has an isotopic abundance near 16.9%, thermal neutron detection is possible with a HgI_2 detector made with natural Hg by detecting the radiation released in the neutron capture reaction.

While HgI_2 has high stopping power, the efficiency of early detectors was relatively low because the detectors were too thin. Thus significant research efforts focused on the growth of HgI_2 crystals. Early growth techniques used the traveling heater method [41], where HgI_2 in a growth ampoule moves through a temperature gradient, forming a single crystal. The primary method of HgI_2 crystal growth is now by vapor phase growth [42] [43] [44] [45]. In this method, the vapors are cooled by a controlled condensation, which helps prevent contamination of the crystal. In the temperature oscillation method used with vapor phase growth, the area of the ampoule where the crystal solidifies will vary slightly in temperature [46]. This technique helps prevent additional crystals from growing and has reduced the time needed to grow crystals. Crystal growth rates of over 10 cm^3/day can be achieved in a single growth ampule, with final HgI_2 volumes of over 150 cm^3 after two weeks. Solution-grown HgI_2 [47] crystals have also been achieved, however the volumes achieved of the detector crystals were quite small (less than 6 cm^3), and the hole transport properties $(\mu\tau)_h$ associated with these detectors were quite low (10^{-6}-10^{-7} cm^2/V) [48]. Other methods of crystal growth have also been attempted with some degree of success [49] [50]. To date, the largest single crystals of HgI_2 have been obtained with vapor transport growth, with volumes near 40

cm^3.

In order to obtain better crystals, the seed material for crystal growth was purified through multiple sublimation [51] and treatment with iodine [35]. Several different starting materials have been studied and it has been suggested that polyethylene treated precursors may be the preferred starting material for both the low amount of impurities and good stoichiometry [52].

There has been some focus upon impurity analysis in HgI_2. Polarization and non-uniformity effects can be attributed to impurities in the detector. Several elemental impurities have been identified [53] [54] along with the possibility of hydrocarbons. In addition, etching with KI can introduce defects and water vapor into the crystal [55]. Since there is a inhomogeneous distribution of impurities in HgI_2 crystals, there was an attempt to grow HgI_2 crystals in space [56], where the effects of gravity on impurity distribution would be eliminated. The impurities seemed to be more evenly distributed throughout the detector crystal due to the lack of gravity and led to improvements in hole mobility [57] [58].

Another disadvantage of mercuric iodide is its vapor pressure of 5×10^{-5} Torr at 300 degK. HgI_2 will sublimate in air at a rate of 3×10^{-5} g/cm^2-sec [59]. In order to prevent this process, an encapsulant must be used with the detector. Several encapsulants have been developed for HgI_2, including Parylene [60] and an amorphous carbon film [61].

Because of the high detection efficiency, several attempts were made at producing devices for medical, industrial and space applications. Arrays of thin HgI_2 detectors have been developed for x-ray detection [62] [63]. HgI_2 detectors arrays have been explored for use in energy-dispersive x-ray diffraction [64]. Lead detection in paint by the excitation of Pb x-rays has been explored using a mercuric iodide detector with a ^{109}Cd source [65]. A similar technique, alpha backscattering spectroscopy, has also been attempted with HgI_2 [66] for use in space missions. Devices such as these can provide in situ chemical analysis of samples, allowing for elemental identification [67]. A system for x-ray astronomy was also attempted [68], however success was limited due to the size of the detector used

in balloon flight experiments. A system for plutonium contamination monitoring was designed but suffered from poor resolution and noise [69]. Dosimetry with HgI_2 was also attempted but the tissue equivalent linearity was limited to 100-600 keV [70]. Miniature probes for in-vivo medical procedures have also been studied and showed possibilities in detecting hot spots in tissue [71].

The ability of HgI_2 to respond to light has attracted attention in the development of HgI_2 as photodiodes for scintillator systems. The response curve of HgI_2 photodiodes is fairly well matched with the output of CsI(Tl) scintillator crystals with a quantum efficiency up to 70% [72]. These detectors have shown very good energy resolution for a scintillation detector system, with a resolution as low as 4.58% being possible [73]. Hand held devices have been explored with under 6% resolution [74] along with coupling HgI_2 photodiodes with GSO for use in positron emission tomography [75]. The major advantage with HgI_2 photodiodes, in addition to resolution improvements, is the significant reduction in size over photomultiplier tubes.

Recent work has primarily focused on the development of polycrystalline mercuric iodide radiation detectors [76] [77]. These detectors should be easier to fabricate since the need for large single crystals of HgI_2 is mitigated. The electrical properties of polycrystalline HgI_2 is very near that of the single crystal devices. However, these detectors have remained quite thin and have only been used to detect low energy gamma and x-rays.

In all the previous work, several deficiencies can be inferred. Only thin detectors (less than 2 mm) can produce spectra with sufficient energy resolution, but with low detection efficiency. Thicker detectors could not produce spectra with good energy resolution (less than 3% FWHM at 662 keV). There was a trade-off between resolution and efficiency due to poor hole movement, even when pulse compensation [12] was used. Thus, it would be desirable to build a thick HgI_2 detector that can provide good energy resolution. Such a device would offer the best of both worlds: well resolved energy spectra and superior detection efficiency.

1.5 Focus of This Work

The goal of this research is to provide an understanding of the underlying principles of developing a large 3-D HgI_2 gamma-ray spectrometer with pixelated anodes. The research involved here includes the theory and modeling of 3-D HgI_2 detectors, the design of prototype detectors to provide proof of principle that the technique will be successful with HgI_2, and to obtain experimental results with pixelated HgI_2 detectors.

Chapter 2 presents the theoretical material needed to understand radiation detection with pixelated HgI_2 gamma-ray spectrometers. First, a discussion on how induced signals on the electrodes are generated using the Shockley-Ramo theorem is presented. This is followed by an introduction to single polarity charge sensing and its effects on both planar and pixelated electrodes. Next, depth sensing by measuring the C/A ratio is presented along with depth correction using the C/A ratio. The last part of Chapter 2 is a discussion on estimating the mobilities and lifetimes of charge carriers (electrons and holes) in pixelated HgI_2 detectors.

Chapter 3 presents the modeling work for pixelated HgI_2 detectors. First, simple gamma-ray spectra assuming no charge loss are simulated to investigate the detection efficiency of HgI_2. These data are compared with CZT detectors and show the better efficiency that may be possible with mercuric iodide. The modeling of the cathode and pixel anode signals is discussed in the second part of the chapter. The incorporation of severe hole trapping will demonstrate that the use of conventional planar electrodes will lead to poor spectral performance with thick HgI_2 detectors, even if very large applied voltages are used. The pixelated anodes, on the other hand, will perform very well and provide very sharp energy resolutions, even at relatively low detector biases. The effects of electron trapping and weighting potentials are discussed, along with the results for a large array of HgI_2 pixels.

Chapter 4 presents the design and setup of the prototype HgI_2 detectors. Each detector has 4 anode pixels surrounded by a large non-collecting anode. There

are actually two different designs: one where the pixels are well separated and one where the pixels are in the middle of the detector next to each other. The electronics and data acquisition system setup is described at the end of this chapter.

Chapter 5 shows the spectroscopic capabilities of HgI_2. First, the signals that come from the different electrodes is presented. Next, the results from collecting spectra from the planar cathode are presented. These results show that planar electrodes cannot yield well-resolved spectra from thick HgI_2 detectors. The majority of the chapter is dedicated to presenting results from 5 mm and 10 mm thick HgI_2 detectors using anode pixels. Both show significant improvements over the planar cathode electrode results. Also, the improvement that can be achieved with depth correction is presented.

Chapter 6 presents results of other experiments performed on pixelated HgI_2 detectors. First, multiple sources were used to collect a complex spectrum to show that these pixelated detectors and the depth correction technique are not limited to collection from single energy gamma-ray sources and can handle many gamma-ray lines effectively. Next, an estimation of the mobility and lifetime products for both electrons and holes is presented. These results show that material non-uniformity may be an important issue in HgI_2 detectors, but the pixelated anode design is able to overcome this effect. Finally, a study on the long term stability and polarization of pixelated HgI_2 is presented and shows that while polarization may still be present in current HgI_2 detectors, the effect is small and not nearly as limiting as previous studies indicated.

Finally, Chapter 7 summarizes the major findings of this work and provides a discussion on some recommended future research using pixelated HgI_2 detectors for room temperature gamma-ray spectroscopy.

Chapter 2

THEORY

In order to understand the induced charge on an electrode, the Shockley-Ramo theorem [78] [79] is introduced and applied to both planar and pixelated electrodes. Depth determination and correction using the cathode to anode signal ratio is then discussed. Finally, a method to estimate the mobility and lifetimes for electrons and holes using data that can be obtained from pixelated anodes is presented.

2.1 Signal Generation on Electrodes in HgI_2

In order to determine the signals on different electrodes, the transport of charge carriers in a semiconductor material needs to be understood. The transportation of electrons and holes can be easily determined if the mobilities are known for each carrier. The velocity ($\vec{v}$) of charge carriers can be described by the mobility (μ) and the electric field ($\vec{E}$) applied to the detector:

$$\vec{v} = \mu\vec{E} \tag{2.1}$$

From the Shockley-Ramo theorem, the current (i) generated by the movement of charge (q) can be calculated by determining the dot product between the velocity and the weighting field ($\vec{E_w}$).

$$i = q\vec{v} \cdot \vec{E_w} \tag{2.2}$$

The total charge (Q) that is induced on an electrode by the moving charge is described by

$$Q = q\Delta\phi_w, \tag{2.3}$$

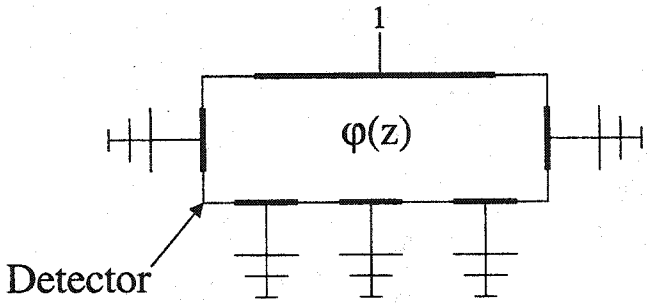

Figure 2.1: Application of the Shockley-Ramo theorem. The electrode of interest is set with a potential of 1 and all other electrodes are grounded.

where ϕ_w is the weighting potential.

In the previous two equations, the terms weighting field and weighting potential have been introduced. These terms do not represent the actual electric and potential fields that are applied to the detector. Rather, they represent how the charge is induced on the electrode. The electric field and the operating potential are set by the detector bias, but the weighting field and potential are determined only by the geometry of the detector and electrodes.

The Shockley-Ramo theorem provides a method to determine the weighting potential on an electrode [80]. The electrode is set with a weight of 1 (for normalization), and all other electrodes on the detector are set to 0. Figure 2.1 provides a description of the setup for determining weighting potential. Using these boundary conditions, the weighting potential as a function of position ($\vec{r}$ can be calculated by solving the Laplace equation:

$$\Delta^2 \phi_w(\vec{r}) = 0. \tag{2.4}$$

Before the solution is obtained, an additional assumption must be included. It is assumed that there is no space charge in the detector. Without this assumption, the calculation would have to be performed with the more difficult Poisson equation. When the electrodes are biased at a constant potential the weighting potential

determines the induced charge ($q(\vec{r})$) on an electrode due to a point charge (Q):

$$q(\vec{r}) = -Q\phi_w(\vec{r}) \tag{2.5}$$

Equation (2.5) shows that the induced charge on an electrode can be determined by only the geometry of electrode and is independent of the actual bias on electrodes. Once the path of a charge carrier is determined by the actual operating potentials and the electric field in the detector, the induced charge on the electrode can be calculated by determining the change of the weighting potential along the path that the charge will take.

2.1.1 Induced Signals on Planar Electrodes

First, consider a conventional detector with some thickness D with parallel plate electrodes (Figure 2.2). Assuming that a negative bias is applied to the cathode and that the signal is read out by the anode, the weighting potential increases linearly (Figure 2.3). Thus, the induced charge on the anode is linearly proportional to the total drift distance of the space charge. If there is a gamma-ray interaction event that produces n number of electrons and holes (each with charge e) at a depth z, the electrons will move towards the anode and the holes will move towards the cathode. The signal on the anode is then determined by

$$q = n_e e(1 - z) + n_h ez = ne \tag{2.6}$$

This equation assumes that there is no charge loss in the detector. The overall signal in this case only depends on the number of electron-hole pairs produced in the detector from the gamma-ray interaction. This would be the case with a perfect detector, however HgI_2 detectors suffer from severe hole trapping. In the case that the holes do not move, the second term in Eqn. (2.6) is zero and the induced charge on the anode is determined only by the first term:

$$q = ne(1 - z) \tag{2.7}$$

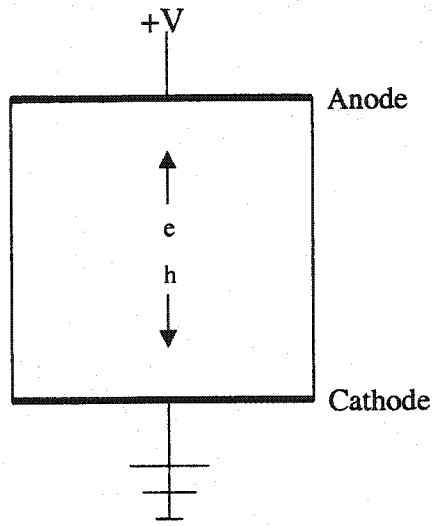

Figure 2.2: Electrode configuration of a conventional planar electrode detector. When a negative bias is placed on the cathode, the holes will move towards the cathode and electrons will move toward the anode. For calculating the weighting potential on the anode, a weighting potential of 1 is placed on the anode, and a value of 0 is placed on the cathode.

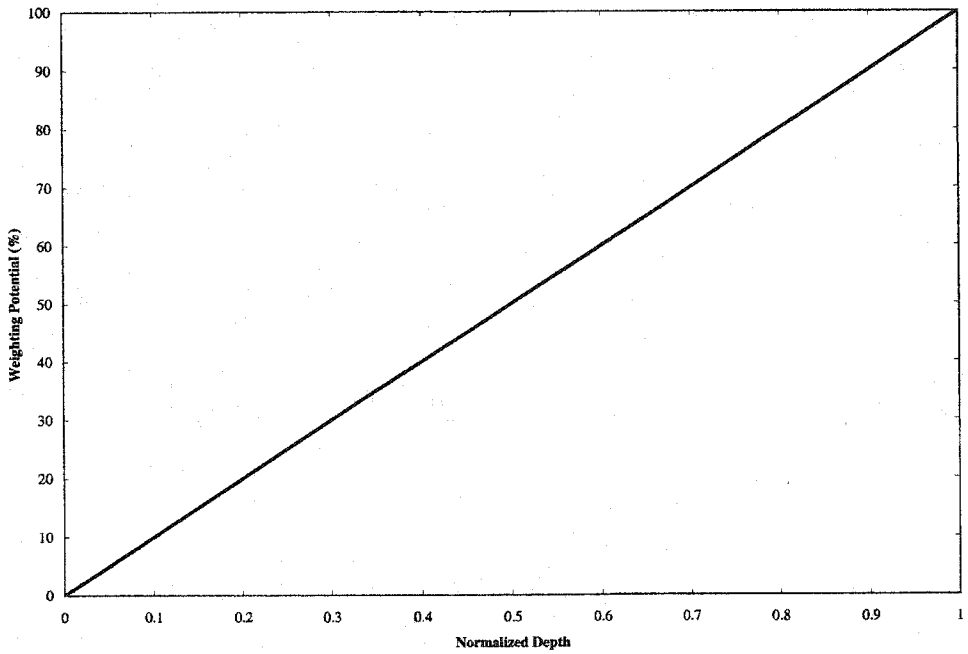

Figure 2.3: Weighting potential of the planar anode. Note the linearity with depth.

Thus, the signal is highly dependent on the interaction position and the detector will not be able to perform as a spectrometer, particularly for high energy gamma-rays where the interaction positions will be distributed throughout the detector.

In reality, the holes will slightly move and contribute a small amount to the signal. The lifetime (τ) of electrons and holes can be used to determine the amount of trapping each carrier will suffer. Since the electric field is constant throughout the entire detector, the number of charge carriers (N) that arrive at the electrode is determined by the distance (Δz) and the number of charge carriers produced by the gamma-ray interaction (N_o):

$$N(z) = N_o e^{\frac{-\Delta z}{\mu \tau E}} \tag{2.8}$$

Using the above equation, assuming that the allowable charge collection time is long, the total induced charge on the planar electrode can be determined by the

Hecht equation [81]:

$$q_t = Q_o \frac{(\mu\tau)_e E}{D}[1 - e^{\frac{-(D-z)}{(\mu\tau)_e E}}] + Q_o \frac{(\mu\tau)_h E}{D}[1 - e^{\frac{-z}{(\mu\tau)_h E}}] \tag{2.9}$$

where z is the interaction position in the detector, D is the thickness of the detector, E is the electric field strength, and $(\mu\tau)_e$ and $(\mu\tau)_h$ are the mobility-lifetime products for electrons and holes, respectively. In the case of severe trapping of one of the charge carriers, the Hecht equation will show a strong dependence on the depth of interaction. This equation will be explored further later this chapter in determining the mobility-lifetime products for the charge carriers.

2.1.2 Induced Signal on Pixelated Anodes

In order to obtain a uniform detector response from HgI_2 detectors, the signal must be obtained from only electron movement. Thus, single-polarity charge sensing must be incorporated. The first use of single-polarity charge sensing was the Frisch grid in gas detectors [14]. In this case, a grid is placed between the anode and cathode of the detector (Figure 2.4). The cathode is negatively biased compared with the grid, while the anode is positively biased. Thus, the electron cloud created by a radiation interaction drifts from the cathode towards the anode. However, the grid effectively shields the anode from charges between the cathode and grid. Thus, no signal is induced on the anode when the electrons are in this region. Only when the electrons move in the region between the grid and anode is a signal on the anode produced. If the Frisch grid is sufficiently close to the anode such that most of the detector volume is between the cathode and the grid, nearly all of the radiation interaction events will occur in this volume. Thus, the induced charge on the anode (q_a) will depend only on the number of electrons created (n_e) and is independent of the interaction location.

$$q_a = n_e e(\phi(1) - \phi(z)) = n_e e \tag{2.10}$$

In the absence of electron trapping or recombination, the induced charge on the anode will be independent of the interaction depth, and collection of the slower

moving ions is not necessary. However, should an interaction occur between the Frisch Grid and anode, the collection of both holes and ions will be necessary in order to determine the total energy deposited in the detector.

In order to take advantage of single-polarity charge sensing with room-temperature semiconductor gamma-ray spectrometers, special electrode geometries must be applied. The coplanar anode design consists of two groups of parallel strips. While the cathode maintains a strong negative bias on the detector, the coplanar anodes will have a small potential difference between each other [82]. As the electrons move from the cathode towards the anode side of the detector, the induced charge on each anode will behave similarly to a conventional electrode. However, once the electrons get sufficiently close to the coplanar anodes (commonly assumed to be one pitch depth), the potential difference between the coplanar anodes will produce an electric field such that all of the electrons are collected on one anode (called the collecting anode). The induced charge on the collecting anode will increase rapidly, while the other electrode (the non-collecting anode) will experience a decreasing induced charge since the electrons will be moving away from this electrode. By reading out the difference signal of the collecting and non-collecting anodes, a signal is generated that is similar to the anode signal from a detector employing a Frisch grid [83]. The signal will be dependent only on the number of electrons and the slower moving and significantly trapped holes in compound semiconductors will not contribute to the signal. Only events near the anode will suffer from a depth dependent signal. Thus, detectors with a coplanar anode design can be used as a single-polarity charge sensing device.

Another electrode design that will produced a signal that is relatively independent of the depth of the radiation interaction is the pixelated anode design [17]. This design consists of an array of small anode pixels on a detector (Figure 2.5). To solve for the weighting potential, one pixel has a bias of 1 while all other pixels and the cathode have bias of zero. The results for the weighting potential have been determined for both 5 mm thick and 10 mm thick detectors (Figure 2.6). The weighting potential for a pixel is near zero for most of the detector thickness, in-

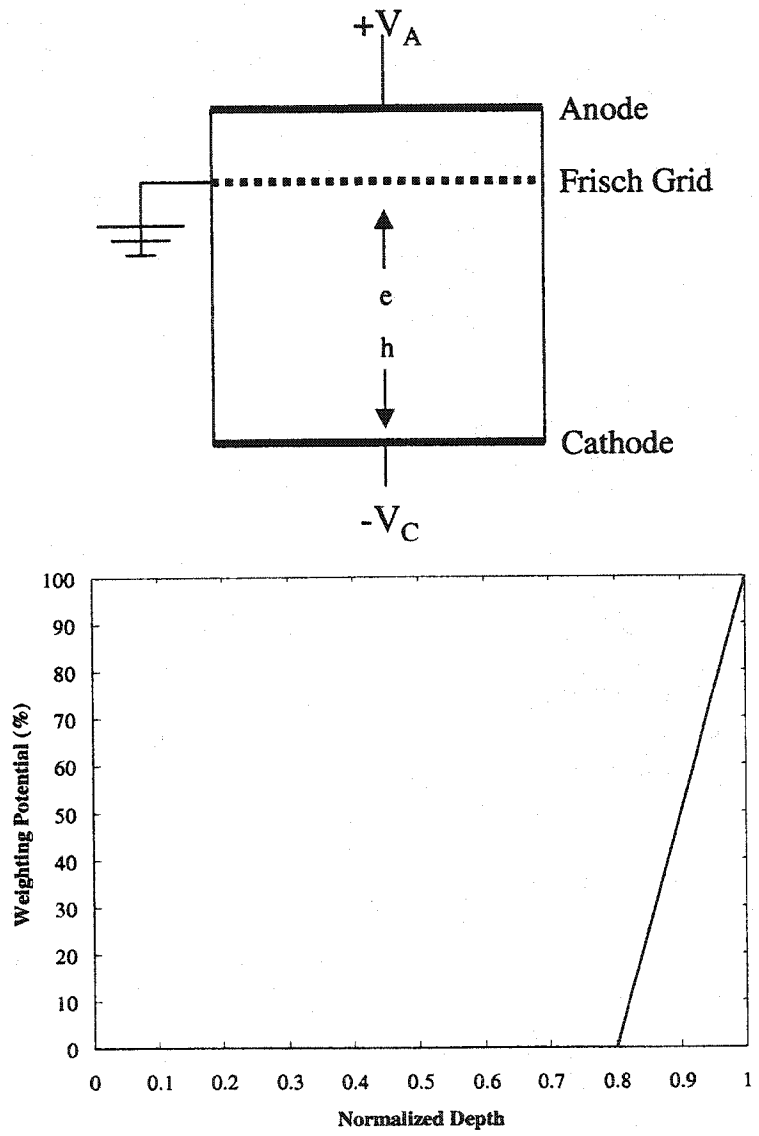

Figure 2.4: (a) The Frisch Grid design consists of a grid electrode placed between the anode and cathode. A negative high bias is applied to the cathode, the Frisch Grid is grounded, and a small positive bias is applied to the anode. (b) Weighting potential for the anode is linear and nonzero only between the Frisch grid and anode.

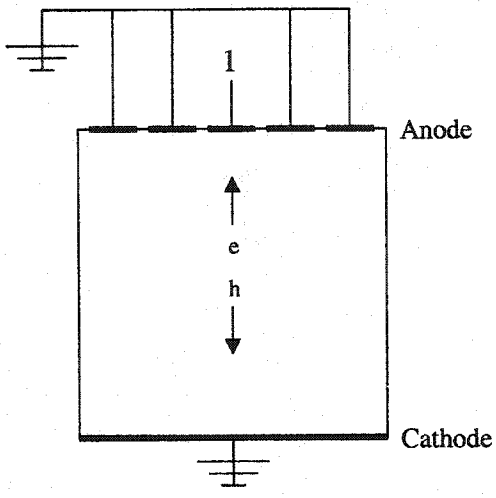

Figure 2.5: The pixelated anode design consists of an array of small area pixels on a relatively thick detector.

creasing rapidly to 1 near the pixel beginning approximately one pitch depth from the anode.

While most of the induced charge is produced near the pixel, the signal has a small amount of dependence on the depth of interaction. This dependence is due to the pitch to thickness ratio [84]. Thus, the weighting potential of the 5 mm thick detector will have a stronger dependence on depth than the 10 mm thick detector, assuming the pitch depth (pixel size) are the same in both cases. However, a 10 mm thick detector with a 2 mm pitch will have a comparable weighting potential with the 5 mm thick detector with 1 mm pitch.

Single-polarity charge sensing with room temperature semiconductor detectors eliminates the need to collect the severely trapped holes. However, electron trapping can exist and affect the signal, thereby introducing a term that can slightly depend on the depth of interaction. In a pixelated anode detector, the induced charge essentially depends on the number of electrons collected on the pixel. If trapping is present, the induced charge on the anode can be described by:

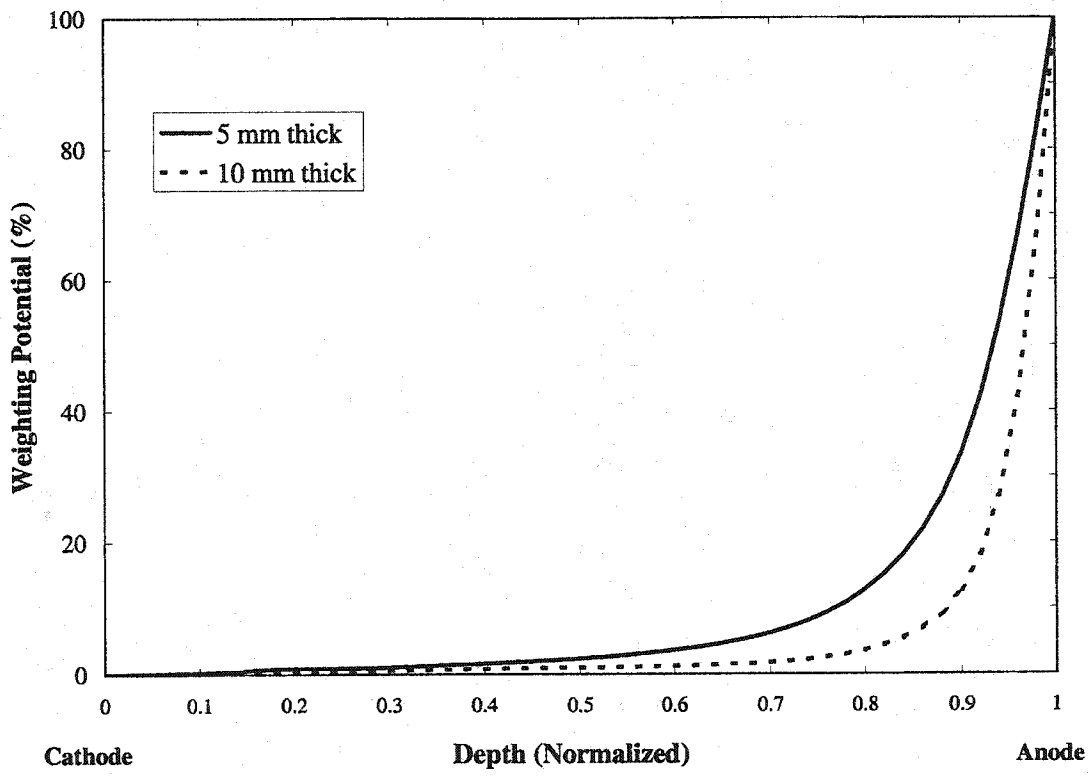

Figure 2.6: Weighting potential for a 1 mm^2 pixel on a 5 mm and 10 mm thick detector. Note the slightly stronger depth dependence of the weighting potential for the 5 mm thick detector.

$$q_a = q_o e^{\frac{-(D-z)}{(\mu\tau)_e E}} \tag{2.11}$$

In this equation, q_o is the original charge created by the gamma-ray interaction, namely $n_e e$. The above equation states that the trapped electrons will not contribute to the signal on the anode pixel. This is not entirely true since the weighting potential has a small dependence on depth, and electrons that are trapped within the pitch region near the anode may contribute a large signal on anode. However, if the amount of electron trapping is small, this effect should be minimal. In fact, electron trapping may counter the small amount of depth dependence with the weighting potential and this phenomenon will be explored in Chapter 3.

2.2 Depth Sensing and Depth Correction

While single polarity charge sensing with pixelated anode detectors removes most of the depth dependence of the induced signal, some depth dependence will still remain due to the weighting potential and electron trapping. Fortunately, it may be possible to partially remove these effects if we can determine the depth of the interaction and correct the signal for the interaction depth. Depth sensing and correction requires that signals be measured from both the anode pixel and the conventional planar cathode.

2.2.1 Depth Sensing by Measuring the C/A Ratio

Depth sensing with pixelated HgI_2 detectors can be performed by measuring the signals on both the anode pixel and the planar cathode for each event. An example of depth sensing by measuring ratio of the cathode to anode signals is shown in Figure 2.7, where a near one-to-one correspondence can be observed between the actual depth of interaction and the measured depth of interaction. The anode signal is determined by single-polarity charge sensing and can be determined by the following equation (assuming no electron trapping):

$$V_a = K_a n \tag{2.12}$$

This voltage signal on the anode pixel (V_a) is proportional to the number of electrons generated by the gamma-ray interaction. K_a is a constant that depends on the charge on an electron and the gain of the signal due to the associated electronics in the detector system. Since the cathode is a conventional planar electrode, the voltage signal on the cathode (V_c) is proportional to the position of the interaction (z):

$$V_c = K_c n z \tag{2.13}$$

Here, K_c represents the charge of electrons and the gain of the signal due to electronics connected to the cathode. If the electronics are the same for both the anode pixel and planar cathode, K_a and K_c are the same. Dividing the cathode signal by the anode signal, we get:

$$\frac{C}{A} = \frac{V_c}{V_a} = \frac{K_c n z}{K_a n} = z \tag{2.14}$$

Thus, the depth of the interaction can be estimated by measuring the C/A ratio. However, material non-uniformity and electron trapping can cause this technique to be inaccurate. As long as the C/A ratio has a monotonic relationship with interaction depth, though, this technique can still be used for depth sensing and allow for depth correction of the anode pixel spectrum. In reality, K_c and K_a may not be equal. However, the C/A ratio can still be normalized and depth sensing can still be achieved.

2.2.2 Depth Correction

When depth sensing is applied to pixelated anode HgI_2 detectors, the detector is virtually divided into many small detectors. The volume under each anode pixel is divided into k voxels, where k represents the number of depths. The measured signal from each voxel will vary due to the weighting potential of pixelated anodes, electron trapping, and material variations of the crystal. The measured deposited energy measured by the i-th pixel can be described by [18]:

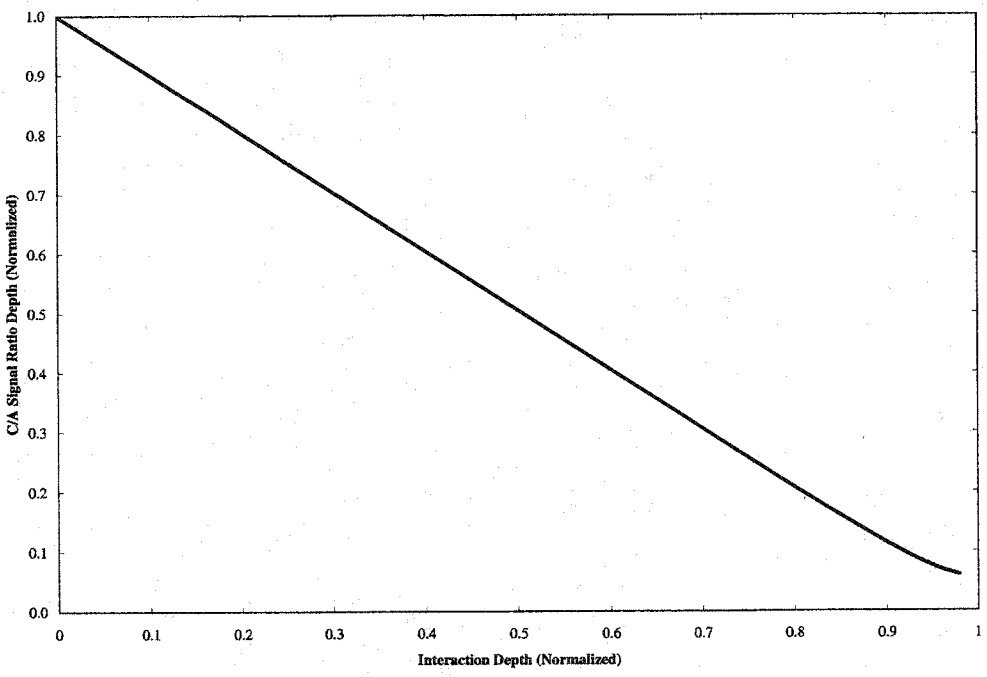

Figure 2.7: By measuring both the cathode and anode signals from a pixelated detector, the depth of interaction can be inferred.

$$V_i(k) = f_{ik}E_{ik} \tag{2.15}$$

Here, $V_i(k)$ represents the signal from the pixel, f_{ik} is the variation in the gain, electron generation, and electron trapping at a particular depth, and E_{ik} represents the energy deposited at that depth. By measuring the photopeak centroid of a monoenergetic gamma-ray source for position ik, the f_{ik} can be determined from

$$f_{ik} = \frac{V_{centroid,i}}{E_{ik}} \tag{2.16}$$

In order to correct for the depth of interaction, a gain adjustment $1/f_{ik}$ must be performed. This gain correction is applied prior to combining all of the spectra from the voxels of the pixels. This correction is performed after the spectra from individual depths have been recorded since it is difficult to apply the correction before the analog to digital (A/D) conversion.

Each channel j of a spectrum has a width of ΔV with boundaries

$$V_{i-1} = (i-1)\Delta V \tag{2.17}$$

and

$$V_i = i\Delta V \tag{2.18}$$

When the gain correction $G = \frac{1}{f_{ik}}$ is applied to the spectrum, the channel width of the new spectrum (ΔV_j)changes by $1/G$.

$$\Delta V_j = \frac{\Delta V}{G} \tag{2.19}$$

Thus, the boundaries for the new spectrum can be described by

$$V_j = j\Delta V_j. \tag{2.20}$$

Thus, the boundaries of the new spectrum and the old spectrum are related ($V_{i-1} < V_j < V_i$). The number of counts in each channel of the new spectrum (N_j)

is then calculated using the number of counts from the old spectrum (N_i) by the following equation:

$$N_j = N_{i-1}\frac{V_{i-1}-V_{j-1}}{\delta V} + N_i\frac{V_j - V_{i-1}}{\delta V} = N_{i-1}(i-1-\frac{j-1}{G}) + N_i(\frac{j}{G}-(i-1)). \quad (2.21)$$

The first term of the equation represents the number of counts from the channel with a slightly lower voltage boundary that contributes to the current (j-th) channel of the new spectrum, while the second term represents the number of counts from the channel with a slightly higher voltage boundary that will contribute to the same channel. Thus, the new spectrum is determined by the related channel numbers and the gain coefficient G (Figure 2.8). After applying the correction, the spectra from all voxels are combined to form a depth corrected spectrum. In order to ensure that no distortion appears due to this depth correction technique, 20 channels are sampled around the peak to avoid any potential undersampling.

2.3 Estimating Mobilities and Lifetimes for Charge Carriers

The mobility and lifetime of holes and electrons determine the charge transport characteristics in the detector. A detector with high and uniform charge carrier properties throughout the material will generally perform better as a spectrometer. A method to estimate the electron and hole $\mu\tau$ products is presented.

2.3.1 Determining the Mobility of Electrons and Holes

In pixelated HgI_2 detectors, the electric field is uniform except near the pixels where the electric field lines will bend slightly toward the pixel electrodes. However, the mobility of the electrons (μ_e) can be estimated by measuring the drift time (t_{drift}) for electrons from an interaction near the cathode (the electrons will drift the entire thickness of the detector):

$$\mu_e = \frac{v_e}{E} = \frac{D}{Et_{drift,e}} \quad (2.22)$$

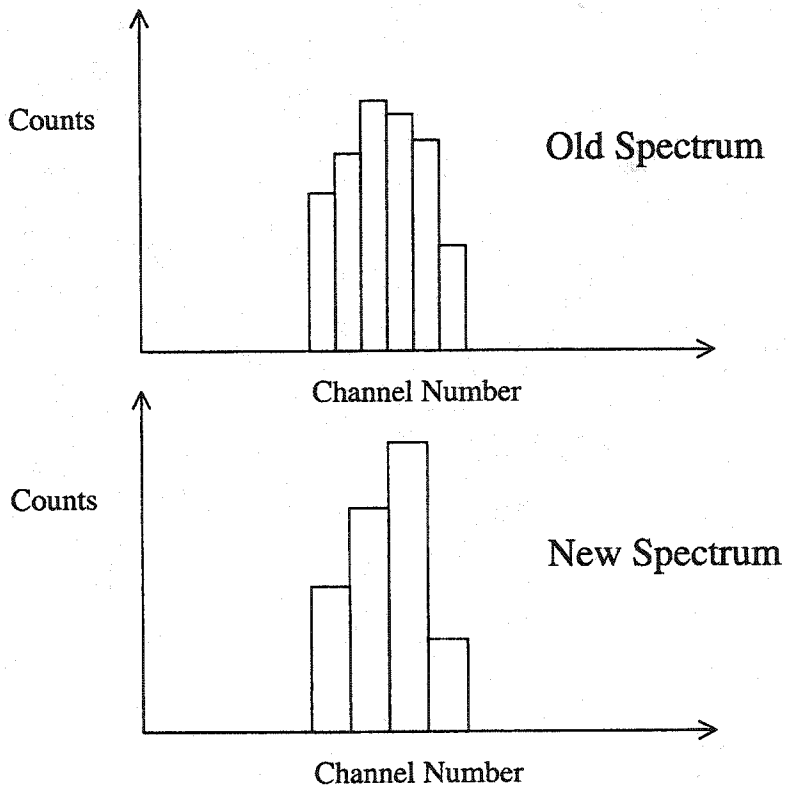

Figure 2.8: By applying a gain correction factor, the new count number in corrected spectrum is determined by the related channels in the original spectra.

In this equation, the drift time is measured by the rise time of the signal from the cathode. The mobility of holes is more difficult to measure due to the severe trapping present in HgI_2 detectors. However, it may be possible to estimate μ_h by measuring the signal from a pixel for an event near the anode. This event will show a signal on the pixel since the slope of the weighting potential in the pitch depth is steep. Thus, as long as the holes can move some distance (denoted as d_h), an estimate for μ_h can be made:

$$\mu_h = \frac{d_h}{E t_{drift,h}} \tag{2.23}$$

In order to determine the distance the holes will travel in HgI_2, an assumption must included. If it is assumed that the holes will travel at least as far as the pitch depth, the distance that can be incorporated in the above equation is the pitch depth (d_{pitch}), which can be determined by calculating the ratio of the rise times between the anode pixel (t_{pixel}) and cathode ($t_{cathode}$) signals for an event near the cathode:

$$d_{pitch} = \frac{t_{pixel}}{t_{cathode}} \times D \tag{2.24}$$

In addition, the holes will most likely be severely trapped within the pitch depth and the signal will be significantly smaller than the signal generated by the electrons. The average distance the holes moved can be determined by the ratio of the pixel signal amplitudes for an anode (V_{anode}) and a cathode ($V_{cathode}$) irradiation:

$$d_h = \frac{V_{anode}}{V_{cathode}} \times d_{pitch} \tag{2.25}$$

Using this estimation for the distance holes will travel in HgI_2, Eqn. (2.23) can provide a rough estimate of the hole mobility, which should be roughly one order of magnitude lower than μ_e for HgI_2 detectors.

2.3.2 Estimating Mobility-Lifetime Product for Electrons $(\mu\tau)_e$

The traditional method of determining the mobility-lifetime product ($\mu\tau$) for electrons and holes involves irradiating the detector with low energy gamma-rays.

Most of the gamma-rays are stopped near the side which was irradiated. Thus, irradiating the cathode side of the detector causes the signal produced by the detector to be generated by the movement and collection of electrons. Conversely, an anode irradiation causes the signal to be derived from hole movement. The $\mu\tau$ product for each charge carrier can then be determined by fitting the photopeak centroid produced by the irradiation to the Hecht relation.

The $(\mu\tau)_e$ can be measured in another method with pixelated HgI_2 [85]. For pixelated detectors, the pixel signal depends on the number of electrons collected by the pixel. Trapped electrons will contribute little or no induced charge to the signal. Thus, if the photopeak centroid (H) is measured at two different applied biases (V_1 and V_2) (see Figure 2.9) we get:

$$H_1 = H_o e^{-\frac{D^2}{\mu_e \tau_e V_1}}, \tag{2.26}$$

and

$$H_2 = H_o e^{-\frac{D^2}{\mu_e \tau_e V_2}}. \tag{2.27}$$

Since H_o (the number of electrons) is the same in both equations, this can be eliminated by taking the ratio of the two photopeak measurements:

$$\frac{H_1}{H_2} = e^{\frac{D^2}{\mu_e \tau_e}(1/V_2 - 1/V_1)} \tag{2.28}$$

Solving for $(\mu\tau)_e$, we get

$$(\mu\tau)_e = \frac{D^2}{ln(\frac{H_1}{H_2})}(1/V_2 - 1/V_1). \tag{2.29}$$

Thus, $(\mu\tau)_e$ can be estimated by varying the bias to the detector and observing the shift in the photopeak from a pixel. By incorporating depth sensing with pixellation, higher energy gamma-rays can also be used in this measurement since it is possible to select an interaction from near the cathode surface. By measuring the $(\mu\tau)_e$ from different pixels on the same detector crystal, the material non-uniformity can also be studied.

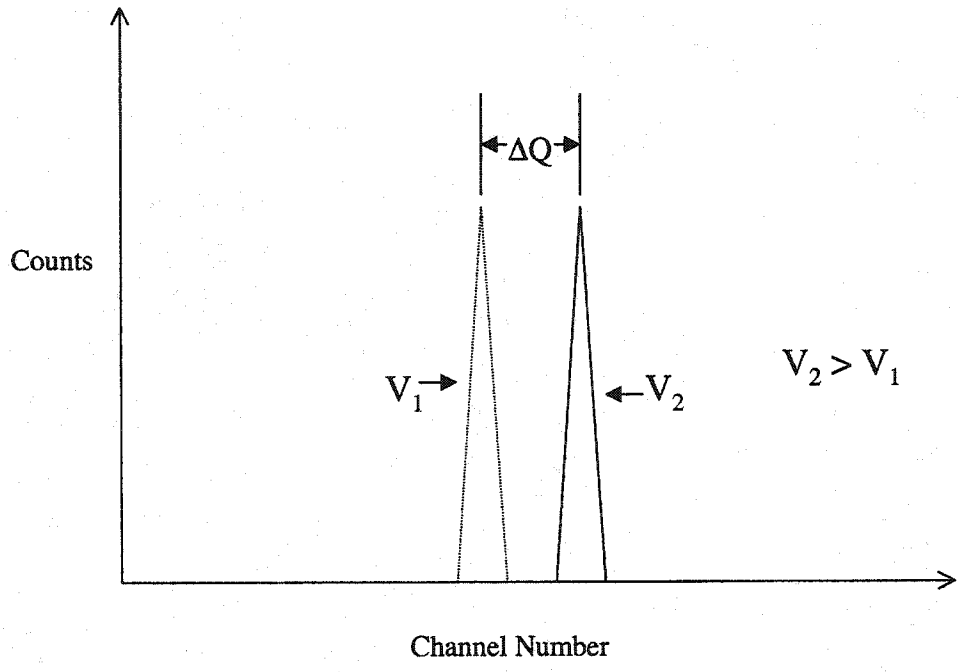

Figure 2.9: Electron loss is less significant at higher detector biases. By measuring the shift in the photopeak centroid, the $\mu\tau$ can be determined.

2.3.3 Estimating Mobility-Lifetime Product for Holes $(\mu\tau)_h$

Due to the significant hole trapping, an accurate measurement of $(\mu\tau)_h$ is difficult to perform. However, an estimate can be obtained by measuring the photopeak peak shift for irradiations from the opposite sides of the detector for the planar cathode [86]. Using the estimate for $(\mu\tau)_e$, the hole mobility-lifetime product can be estimated by using the Hecht relation. With low energy gamma-rays and irradiating from the anode side ($x = 0$), the Hecht equation for the signal generated on the planar cathode reduces to:

$$Q_a = Q_o\left(\frac{(\mu\tau)_h}{D^2}\left(1 - e^{\frac{-D^2}{(\mu\tau)_h V}}\right)\right). \tag{2.30}$$

A similar equation exists for the irradiation from the cathode side, where electron movement dominates the signal.

$$Q_c = Q_o\left(\frac{(\mu\tau)_e}{D^2}\left(1 - e^{\frac{-D^2}{(\mu\tau)_e V}}\right)\right). \tag{2.31}$$

Taking the ratio of these two equation, we obtain

$$\frac{Q_a}{Q_c} = \frac{(\mu\tau)_h\left(1 - e^{\frac{-D^2}{(\mu\tau)_h V}}\right)}{(\mu\tau)_e\left(1 - e^{\frac{-D^2}{(\mu\tau)_e V}}\right)}. \tag{2.32}$$

By obtaining this ratio, the $(\mu\tau)_h$ can be estimated. Thus, by measuring the mobilities of electrons and holes, along with their respective $(\mu\tau)$, estimations of the lifetimes for each charge carrier can be performed.

Chapter 3

Detector Modeling

In order to verify that the HgI_2 detectors work properly, simulations of the detectors need to be performed. In this chapter, we present the modeling of the detector using the GEANT4 Monte Carlo simulation package. First, the modeling of the energy deposition in the detector is discussed. Then, the incorporation of the different signals is included to show the vast improvement in energy spectra using pixelated anodes over a conventional planar electrode. The effects of hole trapping, electron trapping, and the weighting potential for the different electrodes are discussed. In addition, the potential efficiency advantage of a large array of pixels with a HgI_2 detector over a CdZnTe detector of similar size is discussed.

3.1 Modeling Energy Deposition in HgI_2

It is necessary to gain an understanding of the performance of HgI_2 gamma-ray spectrometers. Thus, the energy deposition from gamma-rays needs to be modeled. To model of detectors, the Monte Carlo simulation package GEANT4 [87] was used. This package takes into account all of the physics processes involved with radiation, from low energies in the eV range up to many TeV. The package also allows for easy manipulation of geometry and composition of the detector material.

3.1.1 Simple Model of a 1 cm^3 HgI_2 Detector

The first simulation performed was the simple 1-cm^3 HgI_2 case, shown in Figure 3.1. In this simulation, the spectra generated only considered the energy deposition within the entire detector volume. The results of this simulation would correspond

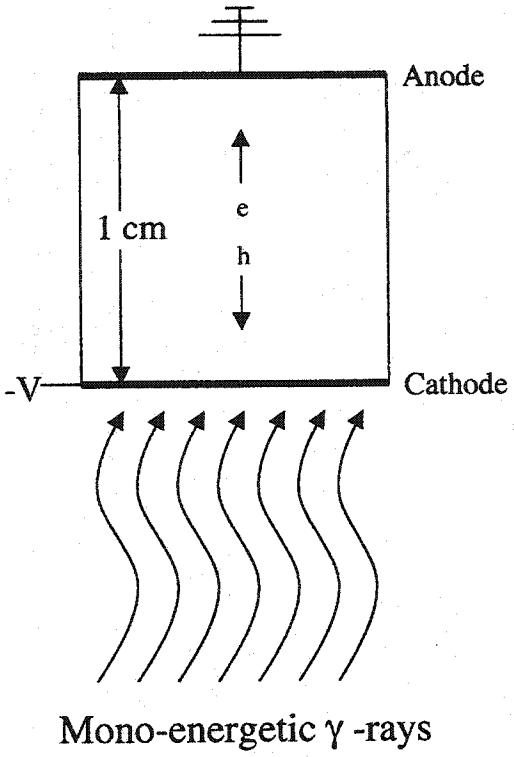

Figure 3.1: Setup for simple HgI_2 detector simulations.

to the ideal case that the HgI_2 detector could work with a planar electrode and that all electrons and holes could be collected without becoming trapped within the detector.

The simulations were performed using 662 keV gamma-rays (to simulate a ^{137}Cs source) uniformly incident on the cathode side of the detector. The results from this are shown in Figure 3.2. A Gaussian spreading term has been included to simulate the spreading of the photopeak due to electronic and statistical noise. The detection efficiency of 662 keV gamma-rays was approximately 42 percent and the intrinsic photopeak efficiency was about 19 percent (see Table 3.1). Thus, nearly half of the gamma-rays that interacted with the 1 cm^3 HgI_2 detector resulted in a photopeak event (from either single photoelectric events or multiple Compton interaction events.

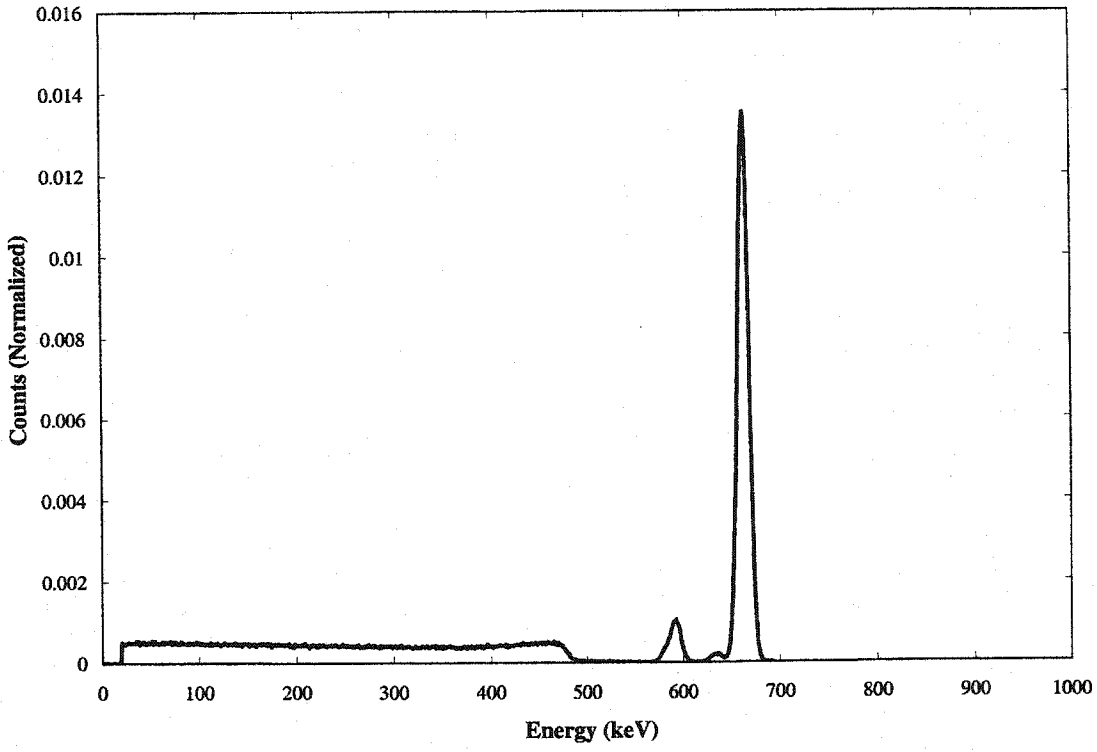

Figure 3.2: Spectrum from a 1 cm^3 HgI_2 detector based on energy deposition. Spreading is included to simulate electronic and statistical noise.

Table 3.1: 662 keV Gamma-Ray Detection Efficiency for a 1 cm^3 HgI_2 Detector Based on 10^6 Incident Photons

Parameter	Total Number	Percent
Number of Interacted Gamma-Rays	422361	42.2%
Number of Photopeak Events	193095	19.3%
Number of Escape Peak Events	19110	1.9%

In addition to the photopeak centered at 662 keV, there are two additional small photopeaks in the spectrum, one near 630 keV, and the other near 585 keV. These two peaks represent the escape peaks of the material. When a gamma-ray has a photoelectric interaction with a bound electron, this electron can gain enough energy such that it will be knocked out of its orbital shell. Some energy will be required to allow the electron to escape. Another electron from an outer shell will replace the photoelectron in the inner shell. In this process, an x-ray is released representing the energy difference of the two orbital shells. Should this low energy x-ray escape the detector without interacting, there will be a lower deposited energy recorded in the spectrum. Since escape x-ray energies increase with increasing atomic number, the small peak at 630 keV represents the x-ray escape peak of gamma-ray interactions with iodine, and the escape peak at 585 keV represents gamma-ray photoelectric interactions with mercury. If the escape peak events are considered true photopeak events, the intrinsic photopeak efficiency of a 1 cm^3 HgI_2 gamma-ray spectrometer would be over 20%.

3.1.2 Modeling Energy Deposition in One HgI_2 Pixel

For a pixelated detector, the induced charge on an individual pixel is primarily determined by the energy deposited in the volume directly under the pixel. Thus, it is important to model the energy deposition in a pixel region. The setup for this simulation is shown in Figure 3.3. The simulated pixel region has a 1×1 mm^2 cross-sectional area and is slightly offset from the center of the detector to simulate the actual detector design (see Chapter 4). Only radiation interactions that result in energy depositions within the pixel region are considered in the spectrum generation.

The results of the pixel energy deposition simulation is shown in Figure 3.4. Due to the much smaller effective volume of the pixel region (10 mm^3), the efficiency of one pixel is about 1% that of a full detector. In addition, the Hg and I escape peaks appear to be a much larger compared to the full energy photopeaks events. In the pixelated detector case, it is possible for x-rays to escape out of the

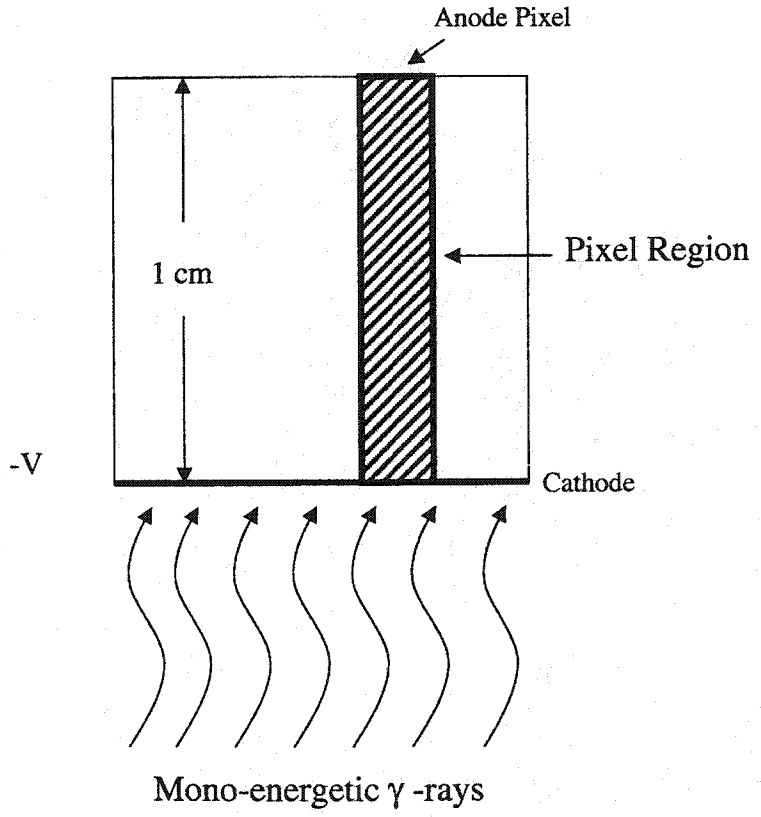

Figure 3.3: Simulation setup for a 1 cm^3 HgI_2 detector with a pixel anode. The pixel region has a 1×1 mm^2 cross-sectional area. Only energy depositions within the pixel volume are considered in the simulation.

side of the pixel region into other parts of the bulk HgI_2 volume. Events such as these would appear as a full energy event in the planar electrode (1 cm^3) case. The broadening of the escape peaks was not only due to the simulated electronic noise, but also due to the different x-ray energies generated in each electron shell. For example, the two Hg K-shell x-ray energies have a difference of approximately 13 kev (83 keV and 70 keV for the k_α and k_β x-rays, respectively). In addition, it is possible that escape x-rays from the surrounding HgI_2 materials will interact within the pixel region. These event peaks appear in Figure 3.4 at the escape x-ray energies around 32 and 80 keV, however only the Hg x-ray barely visible in the spectrum due to the low probability of the I x-ray traveling far enough in HgI_2 to penetrate the pixel region.

3.1.3 Energy Deposition in a Fully Pixelated Detector

In a room-temperature semiconductor detector, full energy depositions can occur from a single gamma ray undergoing several interactions (multiple Compton scatters plus a photoelectric interaction) within the detector. In a detector with an array of anode pixels, the energy deposited in the detector will show up on multiple pixels in a multiple interaction photopeak event (escaped x-rays can also cause multi-pixel events). In addition to multiple interaction events, the electron cloud size and the diffusion of electrons as the cloud moves toward the pixel can also cause some of the single pixel photopeak events appear as multiple pixel events. Thus, it is important to determine the number of pixels that will receive a signal for each photopeak event.

The results for a 11 $\times$ 11 pixel array with a pitch of 1.3 mm (pixel size is 1.3 $\times$ 1.3 mm^2) is shown in Figure 3.5. For a 662 keV incident energy (Cs-137), nearly half of the photopeak events occurred under one pixel. In addition, over 85% of all the gamma-rays that would contribute to a photopeak from the entire detector volume had interactions under only 1 or 2 pixels.

However, energy deposition is not confined to one point. The photoelectron created in the interaction will eventually create an electron cloud of many charges.

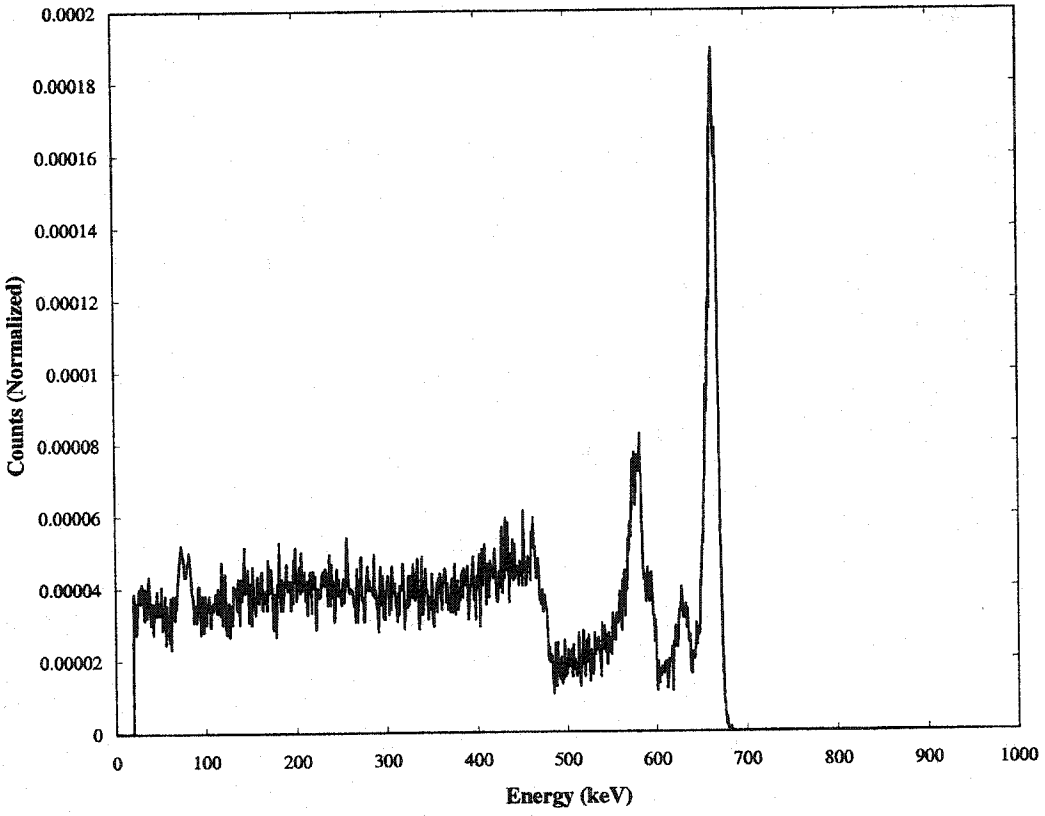

Figure 3.4: Simulated spectrum from a 1 cm^3 HgI_2 detector pixel anode. The cross-section of the pixel was 1 $\times$ 1 mm^2. Note the increase in the relative size of the escape peaks due to mercury and iodine x-rays escaping the sides of the pixel region into the bulk HgI_2 material.

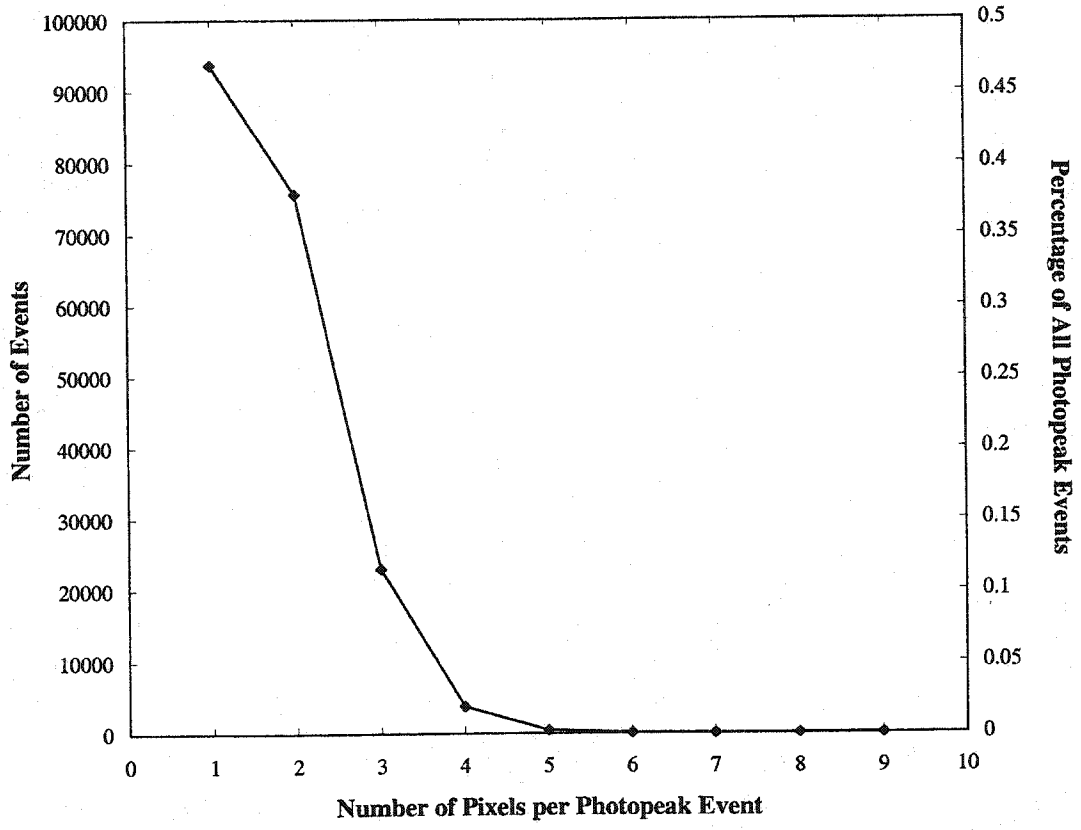

Figure 3.5: The number of pixels that recorded a signal for each 662 keV photopeak event for a 1 cm thick HgI_2 detector with a pixel pitch of 1.25 mm. Only energy deposition is considered in this simulation.

Some of these electrons can be created in an adjacent pixel if the original event occurred near a pixel boundary. For a 662 keV photoelectric event, the average electron cloud size was estimated to be 150 μm. Thus, when the finite electron cloud size is considered for the gamma-ray interactions, the number of single pixel events will decrease by about 7%, indicating an increase in charge sharing between pixels (see Figure 3.6).

The number of pixels for each photopeak event can be significantly impacted by the energy of the gamma-ray of interest. Figure 3.7 shows the number of pixels that record a signal for each photopeak event at three different energies (122, 662, and 1332 keV). At low energies where the photoelectric effect dominates the interaction

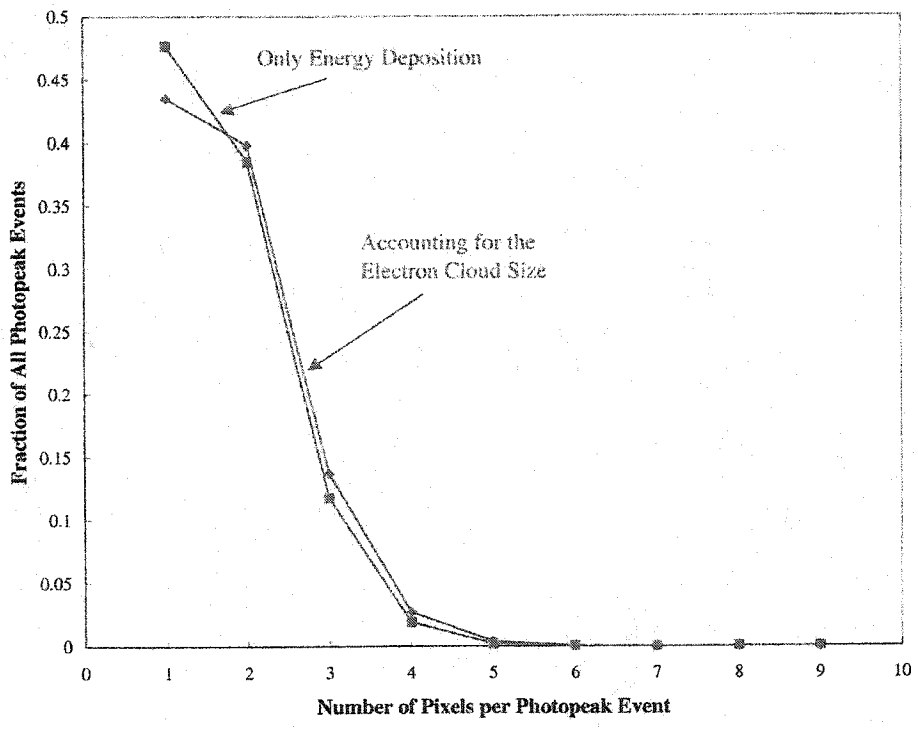

Figure 3.6: Incorporating the size of the electron cloud produced in the detector decreases the number of single pixel events while increasing the fraction of multiple pixel events. The simulated detector thickness was 1 cm with a pixel pitch of 1.25 mm.

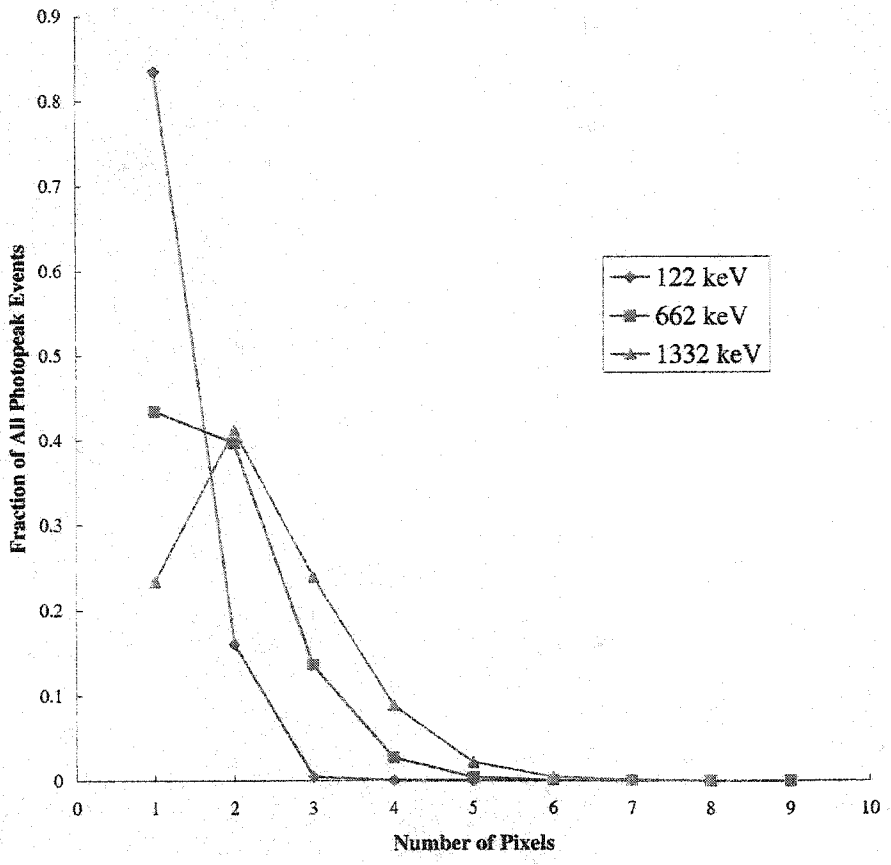

Figure 3.7: The number of pixels that record a signal for each photopeak event can vary widely for different gamma-ray energies. At low energies where the photoelectric effect dominates, most photopeak events are single-pixel events. At higher energies where gamma-rays go through Compton scattering, multiple pixel events dominate.

process, most of the photopeak events are single pixel events. However, at higher energies (such as 1332 keV) where Compton scattering is the dominant effect, the majority of the photopeak events are multiple pixel events (2 pixels or more).

As the electron cloud moves toward the anode pixel, it will expand due to diffusion. This diffusion can be described by [88]

$$D = \frac{KT}{e}\mu_e \tag{3.1}$$

where D is the diffusion coefficient, T is the absolute temperature, e is the elec-

tron charge, and μ_e is the electron mobility. The severity of electron diffusion will also depend on the distance and time the electrons must travel. Thus, electron clouds that must travel a greater distance and in a smaller electric field will suffer from increased diffusion. The amount of spreading (σ) can be calculated by the value for diffusion and the time (t) the electron cloud must travel [1]:

$$\sigma = \sqrt{2Dt} \tag{3.2}$$

For a 1 cm thick HgI_2 detector operated at 2500 V, the electron cloud will spread by approximately 75 μm. Figure 3.8 shows the results for a 1 cm thick HgI_2 detector with a 1.3 mm pixel pitch with electron diffusion incorporated into the simulation. The number of single-pixel photopeak events in the detector decreased further due to the the diffusion of charge. The result also shows the number of single-pixel events improves with increases detector bias, showing a decrease in the influence of electron diffusion.

The size of the anode pixels can also effect the number of pixels for each photopeak event. Figure 3.9 shows the results from varying the pixel size. In this case, the size of the pixel array (11 $\times$ 11 pixels) remained constant. Thus, the detector size also varied in the simulation. The results indicate that the fraction of single pixel events increases with larger pixel size. However, there is a tradeoff with pixel size. While the amount of charge sharing due to electron diffusion will decrease, there can be an increase in the number of events that would have multiple interactions under one pixel, causing errors in determining the interaction depth of the gamma-ray. In addition, larger pixel size would also increase the depth dependence of the signal, assuming the thickness of the detector remains the same. This dependence could degrade the resolution of the detector.

3.2 Incorporation of Signal Generation

Energy deposition from a gamma-ray interaction is only the first step in creating a gamma-ray spectrum from HgI_2 detectors. A critical step is the signal generation

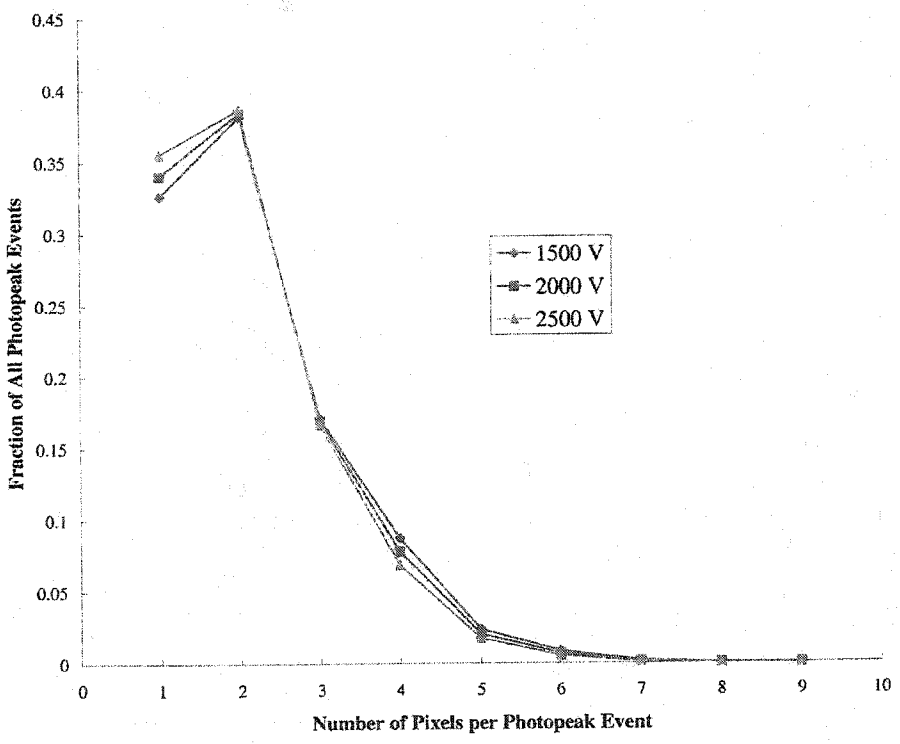

Figure 3.8: Number of pixels for each 662 keV photopeak event in simulations that include the effects of electron cloud size and diffusion. The increase in single pixel events by increasing the detector bias is due to a reduction in the amount of electron diffusion.

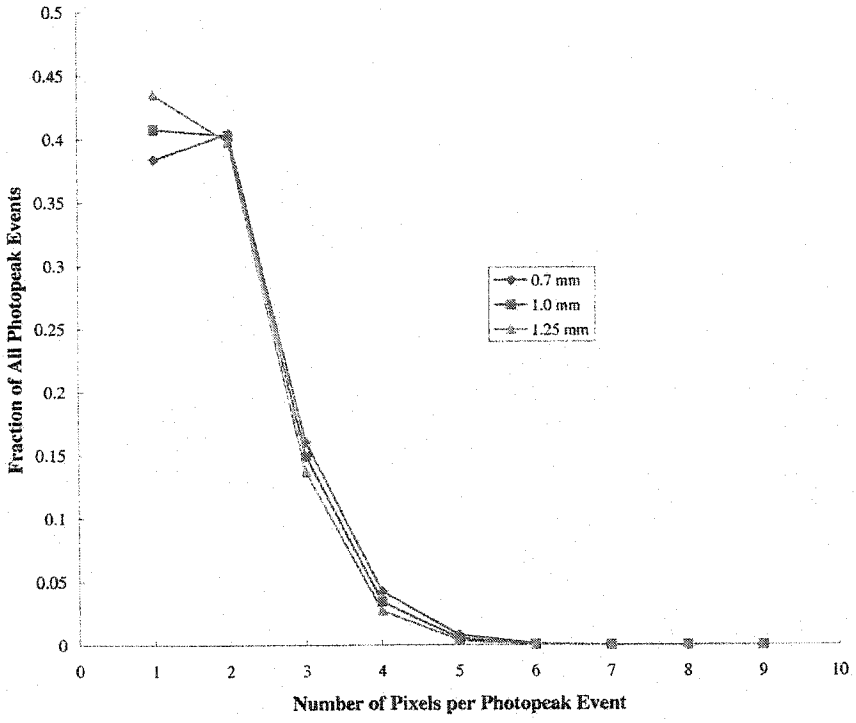

Figure 3.9: Comparison of the number of involved pixels for varying pixel sizes of 11×11 anode pixel array for a 1 cm thick HgI_2 detector. There is a tradeoff between a reduction in charge sharing between pixels and increasing the depth dependence of the weighting potential with increasing pixel size.

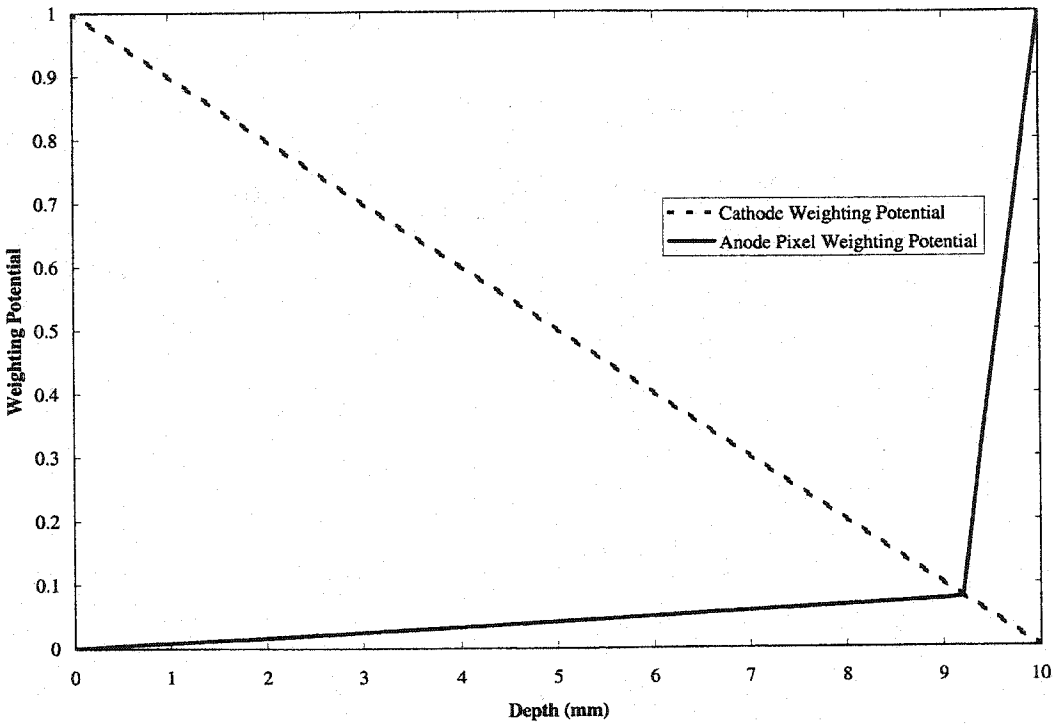

Figure 3.10: Weighting potentials modeled for the simulations. The cathode weighting potential was linear throughout the detector volume, while the pixel weighting potential had a fast rising slope near the anode pixel.

from the separation and movement of the electrons and holes in HgI_2 from the influence of an electric field. Thus, in order to understand how the signal generation will affect spectra from a pixelated anode HgI_2 detector, the weighting potential for the planar cathode and pixelated anode must be incorporated in the simulations. For this study, a linear weighting potential was used for the planar cathode, and a weighting potential with a slight depth dependence that rises quickly near the anode side was used for the pixel (see Figure 3.10).

3.2.1 Cathode Spectra

Since the holes are severely trapped in the detector, only electron movement was initially considered in the simulations. The result is shown in Figure 3.11. Due to the linear interaction depth dependence of the signal, the 662 keV photopeak has

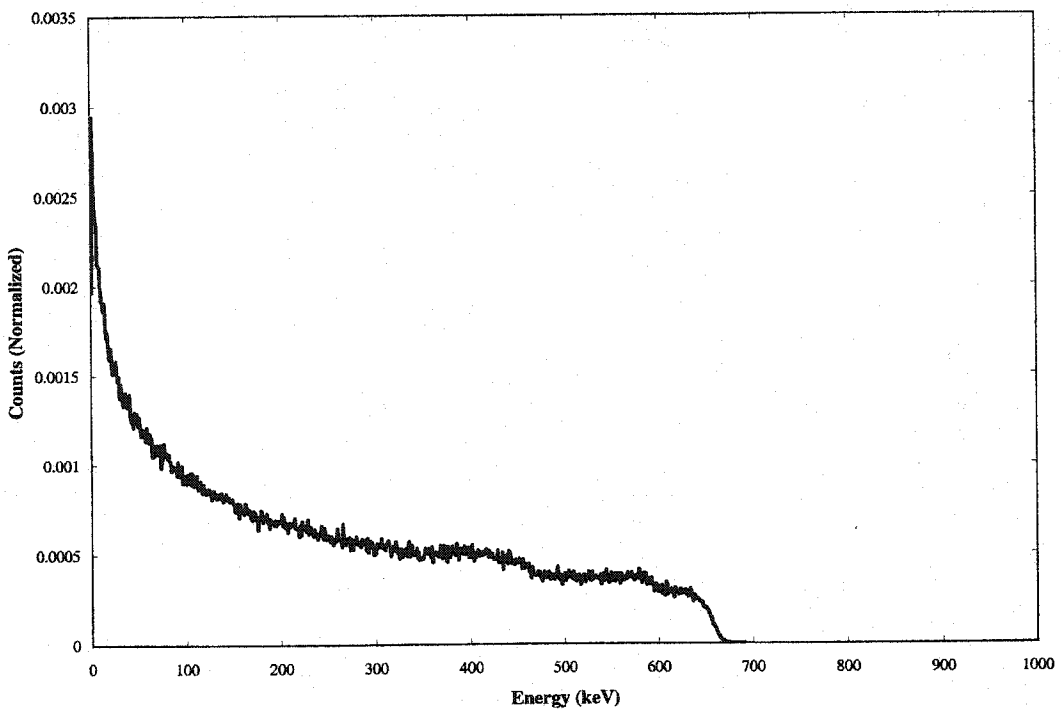

Figure 3.11: Simulated cathode spectrum with no signal contribution from holes. The linear dependence of the weighting potential on the interaction depth causes the loss of the photopeak.

disappeared. The edge of the spectrum still appears near 662 keV due to gamma-ray photopeak interactions taking place near the cathode. However, photopeak events that occur near the anode will induce very little charge since the electrons will only travel a short distance to the anode side of the HgI_2 detector. Small steps can be seen near 580 keV and 480 keV, representing the Hg X-ray escape events and the Compton edge, respectively.

In reality, there will be some hole movement, albeit slight, that will contribute to the signal. Electron trapping can also degrade the signal. Thus, the Hecht equation was incorporated into the simulation to study the effect that changing the bias on a 1 cm thick detector will have on the detector. Assuming $(\mu\tau)_e = 5 \times 10^{-3}$ and $(\mu\tau)_h = 3 \times 10^{-5}$, the generated spectra for 2500, 5000, and 10000 V applied bias are shown in Figure 3.12. In these spectra, while the photopeak is still quite poor, there

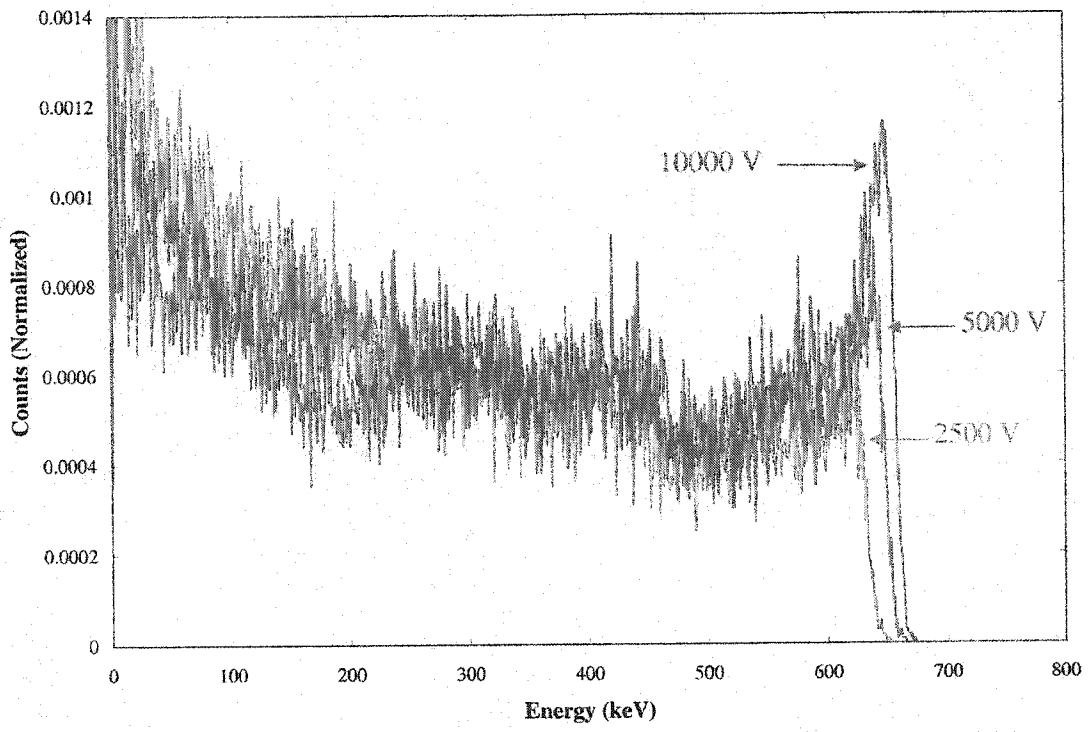

Figure 3.12: Simulated cathode spectrum incorporating the Hecht equation and accounting for both hole movement and electron trapping. The spectrum improved with increasing detector bias due to reduced electron trapping and improved hole movement.

is an improvement with increasing bias due to both reduced electron trapping and slightly improved hole movement. By comparing the photopeak efficiencies with the energy deposition case earlier, with a bias of 10 kV, only approximately 20% of the detector thickness (2 mm in this case) contributed to the 662 keV photopeak. Less than 10% of the detector thickness will contribute to the photopeak when the detector was biased to 2500 V. Thus, it is best to use as large an electric field as possible with planar electrodes.

3.2.2 Anode Pixel Spectra

The weighting potential for the pixel was incorporated into the anode pixel simulation and the resulting energy spectrum is shown in Figure 3.13. There is a significant improvement in the pixel anode spectrum compared with the planar electrode

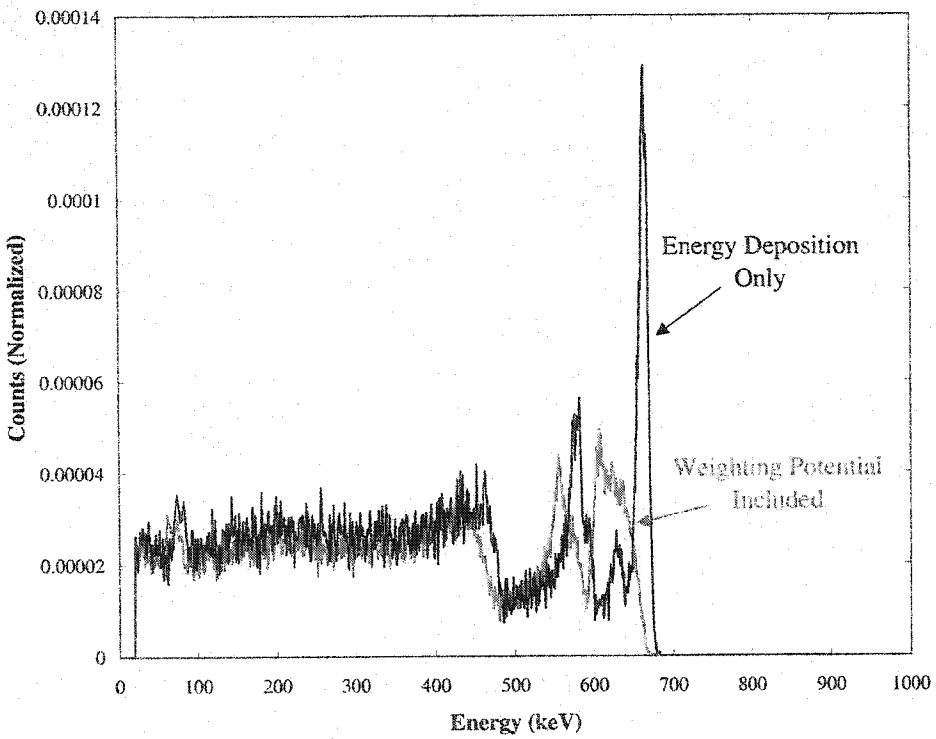

Figure 3.13: Simulated anode pixel spectrum incorporating the weighting potential. Although broad, a photopeak can be observed.

spectrum. Although broad (approximately 10% FWHM), a clear photopeak can be observed. In addition, the Hg escape peak and a Compton edge can also be seen. The broadening of the photopeak was primarily from the slight depth dependence of the weighting potential used in this simulation. The increase in counts on the low-energy side of the photopeak was due the I-escape peak events also contributing to the photopeak. Since the energy of these events is approximately 35 keV less than a true photopeak event, I-escape events contributed to the low energy side of the photopeak when the weighting potential was included. In this simulation, there is only a slight loss in the total number of photopeak events when compared with the case involving energy deposition only. This loss was due to events near the anode where the weighting potential rises sharply and the simulated signal was highly dependent on location of the interaction.

In addition to weighting potential, electron trapping and the effect of applied

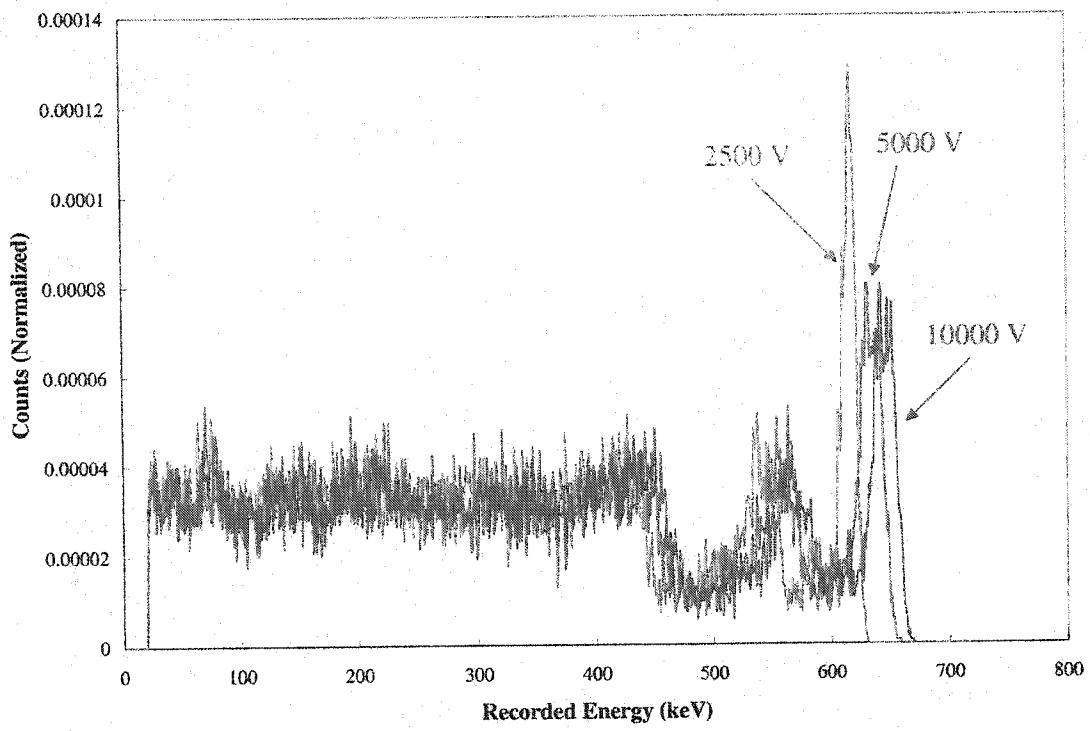

Figure 3.14: Anode pixel spectra at three different cathode biases, accounting for weighting potential and electron trapping. The $(\mu\tau)_e$ used in these simulations was 5×10^{-3} cm^2/V.

bias must also be simulated (hole movement was ignored due to the small effect it would have on the detector performance, given the severe trapping and weighting potential). The results incorporating both the weighting potential and electron trapping into the simulation are shown in Figure 3.14. In this case we see the photopeak shift to the right in the spectra as the detector bias increases, indicating a greater number of electrons are collected by the pixel. In the pixelated anode case, the signal is highly dependent on the number of electrons that are collected by the pixel. Trapped electrons will contribute very little charge to the induced signal on the pixel. Only the electrons that will be trapped within one pitch depth of the pixel will contribute any appreciable charge to the induced signal. However, at 2500 V, the number of electrons trapped within one pitch is much less than 1%, and thus the contribution to the induced signal from trapped electrons is negligible.

While electron trapping is small in HgI_2 detectors, it can play an important role in pixelated anode detectors. In Figure 3.14, the resolution at 2500 V appears to be better than for the 5000 or 10000 V cases. This is counterintuitive since more electrons will be trapped at 2500 V (approximately 7% when the electrons must travel the full 1 cm thickness of the detector) than at 10000 V (less than 2% for the same situation). The weighting potential is slightly larger for interaction events near the cathode, thus inducing a larger signal on the pixel. At the same time, electron trapping will decrease the induced charge on the pixel, and is larger for interactions near the cathode. In the case where the detector is biased at 2500 V, the electron trapping compensated for the slight depth dependence of the pixel anode weighting potential. While this may suggest that it would be advantageous to operate HgI_2 at a lower bias, incorporating depth sensing and correction into the gamma-ray spectra would further improve the energy resolution.

3.2.3 Best Possible Resolution for Planar and Pixelated Electrodes

While the pixelated simulations demonstrate that HgI_2 detectors can performed with energy resolution when pixelated anodes are incorporated, it is possible that the cathode spectra can be improved by having some knowledge of the interaction position (such as from the rise time of the signal [12]). However, pulse compensation techniques such as these cannot overcome the poor signal to noise ratio for interactions close to the anode (small pulse due to the short distance electrons travel and the severe trapping of holes). Figure 3.15 shows the simulated resolution as a function photopeak interaction position for both a planar cathode and an anode pixel based upon 13 keV noise. As can be seen, the resolution of the cathode signal begins to degrade immediately, gradually getting worse as the interaction location gets closer to the anode side of the detector. Thus, the overall depth corrected spectra for the planar cathode will show severe tailing on both sides of the photopeak, as the energy resolution for 662 keV gamma-rays will not be better than about 5-6% (similar to scintillators) even if perfect knowledge of the interaction position is incorporated (Figure 3.16). Meanwhile, the anode pixel signal resolution remains

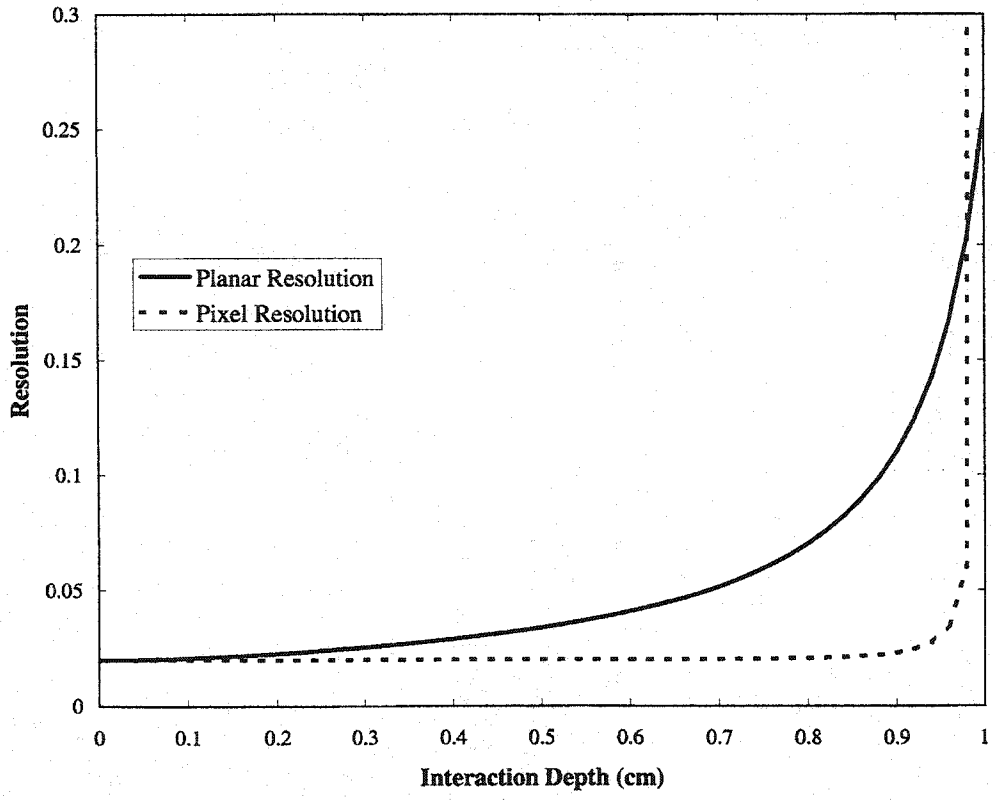

Figure 3.15: 662 keV photopeak resolution as a function of position for both a planar cathode and an anode pixel. Due to the cathode weighting potential and severe hole trapping, the resolution of the cathode signal severely degrades as the event takes place closer to the anode side of the detector. The anode pixel resolution, on the other hand, remains relatively constant since the signal is mostly independent of the depth of interaction.

relatively constant because its signal is mostly independent of interaction depth. Only very near the anode does the resolution degrade. Pixelated spectra can have a depth corrected resolution far better than any resolution from a thick planar detector.

3.3 HgI_2 Detectors Compared With CZT Detectors of Same Geometry

Most of the development of pixelated anode gamma-ray spectrometers has focused on the use of CdZnTe as the room temperature semiconductor material.

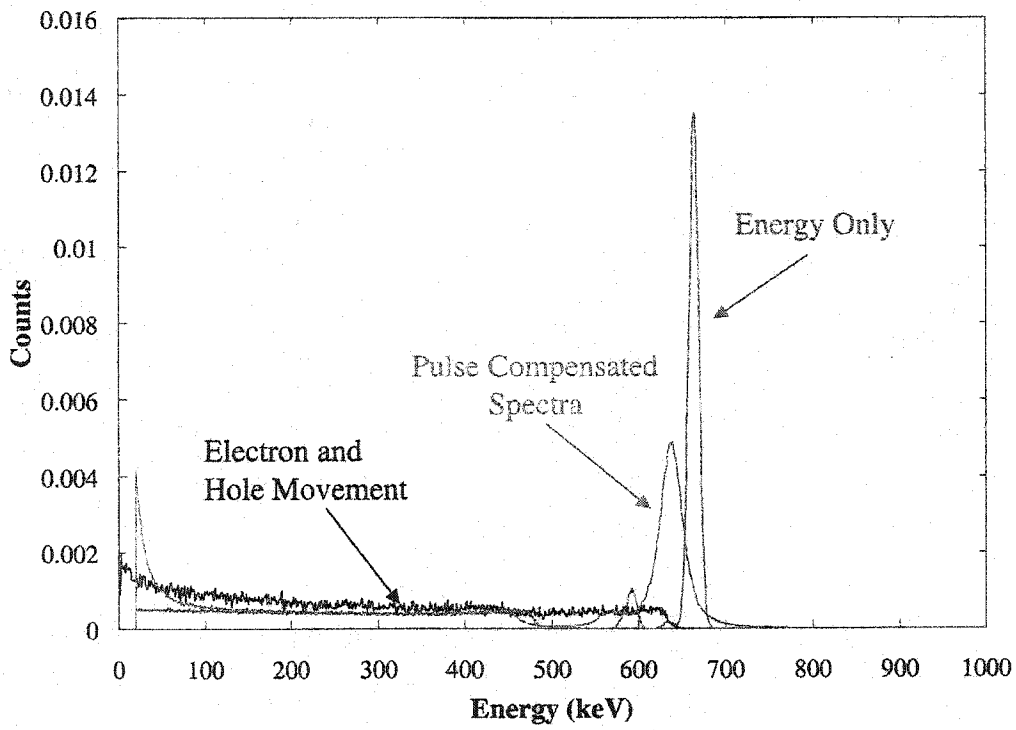

Figure 3.16: While depth correcting the cathode spectrum can improve the photo-peak resolution, the technique cannot overcome the poor signal-to-noise ratio for events near the anode, and the overall resolution will never be much better than 5-6%, even if perfect knowledge about the interaction position can be incorporated into the correction technique.

Table 3.2: 662 keV Gamma-Ray Detection Efficiency Comparison of 1 cm^3 HgI_2 and CdZnTe Detectors

Parameter	HgI_2	CdZnTe	Ge
Gamma-Ray Detection Efficiency	42.2%	35.5%	12.5%
Photopeak Efficiency	19.3%	8.1%	0.93%

CdZnTe suffers from the same basic material problems as HgI_2, namely poor charge transportation and severe hole trapping. Thus it is important to investigate the advantages of HgI_2 over CdZnTe. The higher effective atomic number and slightly higher density of HgI_2 will cause an improved detection efficiency. This is summarized in Table 3.2 (Ge is also included in the table for comparison. The increase in atomic numbers with HgI_2 detectors benefits the intrinsic photopeak efficiency, as the efficiency more than doubles (19.3% versus 8.1%). The gamma-ray detection efficiency also increased slightly, due to both the high atomic number and the increased density of HgI_2. A 1 cm thick HgI_2 detector is equivalent to a 2-3 cm thick CZT detector.

Pixelated HgI_2 detectors hold a significant photopeak efficiency advantage over pixelated CdZnTe detectors of the same geometry. Figure 3.17 shows the percentage of photopeak events that are single-pixel events, two-pixel events, and so on, for both the two detector materials. The high atomic number will increase the 662 keV photoelectric cross section, and the HgI_2 will have a larger fraction of single pixel events. The advantage becomes clear when the absolute number of photopeak events is compared (see Figure 3.18). The number of single pixel events in HgI_2 is nearly equal to the number of all photopeak events in CdZnTe (approximately 85000 to 86000 for HgI_2 and CdZnTe, respectively). This efficiency advantage of HgI_2 is significant. If multiple pixel readout and photopeak reconstruction techniques were used with pixelated HgI_2 detectors, significant efficiency improvements could be achieved over CdZnTe gamma-ray spectrometers.

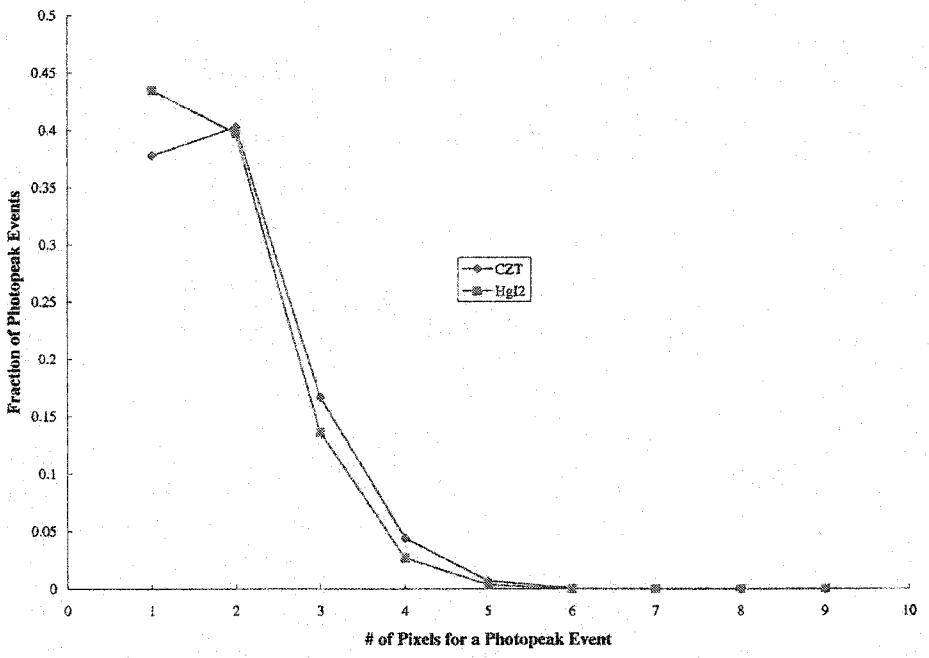

Figure 3.17: Comparison of pixelated HgI_2 and CZT detectors. Here the number of pixels per photopeak event is compared between the two materials for a 11 $\times$ 11 pixel array with a pitch of 1.25 mm^2. The higher value of HgI_2 for single pixel events suggests that a high percentage of photopeak events occur under one pixel than with CdZnTe.

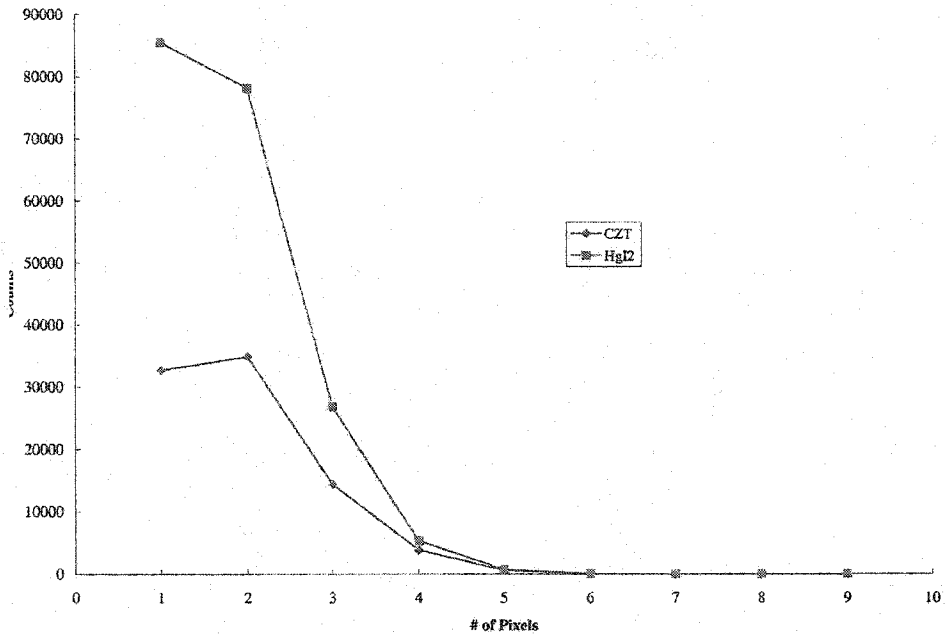

Figure 3.18: Comparison of the number of pixels affected per photopeak event for HgI_2 and CdZnTe. Absolute numbers from the simulation are plotted to show the significant efficiency advantage pixelated HgI_2 detectors have over pixelated CdZnTe detectors of similar dimensions.

Chapter 4

Design And Setup

In this chapter, the detector design and data acquisition setup are described. More specifically, the first part of the chapter presents the two different anode designs used in this work. The first design had 4 well separated pixels each with an area of 1 mm^2 and surrounded on all sides by a large non-collecting anode. The second design had the 4 pixels of the same size next to each other in the middle of the anode surface. The second part of the chapter discusses the electronics and data acquisition setup for the experiments.

4.1 Detector Designs

The first HgI_2 detector design used 5 and 10 mm thick detectors grown by Constellation Technologies, Inc [89]. Each detector was designed with a planar cathode, 4 anode pixels, and a surrounding large anode (see Figure 4.1). Each electrode was created by sputtering palladium onto the detector surface through a mask. Each pixel was approximately 1×1 mm^2 in area. There was a small gap approximately 100-150 μm wide on each side of the pixel to prevent the pixel from being in electrical contact with the large anode. The large anode is called non-collecting not because the large anode doesn't collect charge, but because signals from this electrode are not considered in the generation of gamma-ray spectra. Each pixel is also separated from its neighbors by approximately 3 mm to eliminate any potential charge sharing between pixels. This design was created primarily to study single pixel events in the detector and to investigate the feasibility of using HgI_2 detectors as a pixelated, single polarity charge sensing device for room temperature gamma-ray spectroscopy.

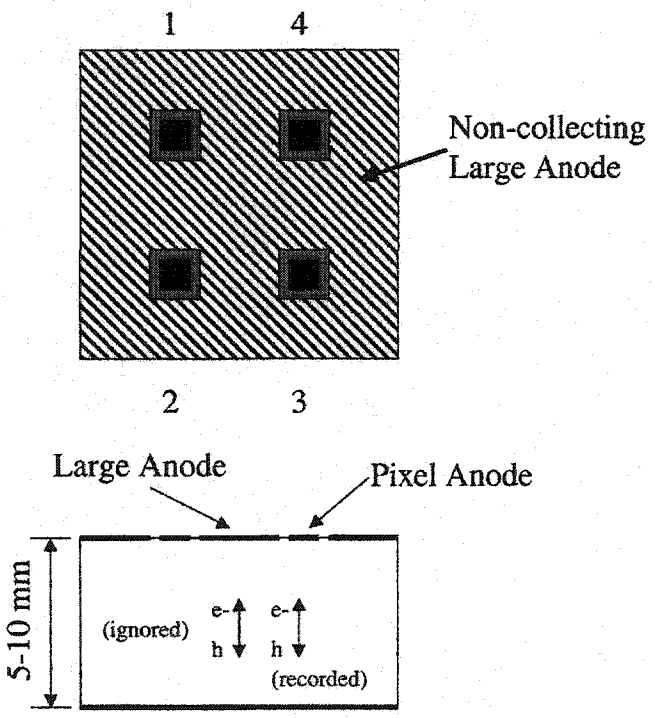

Figure 4.1: First design for the pixelated HgI_2 detectors.

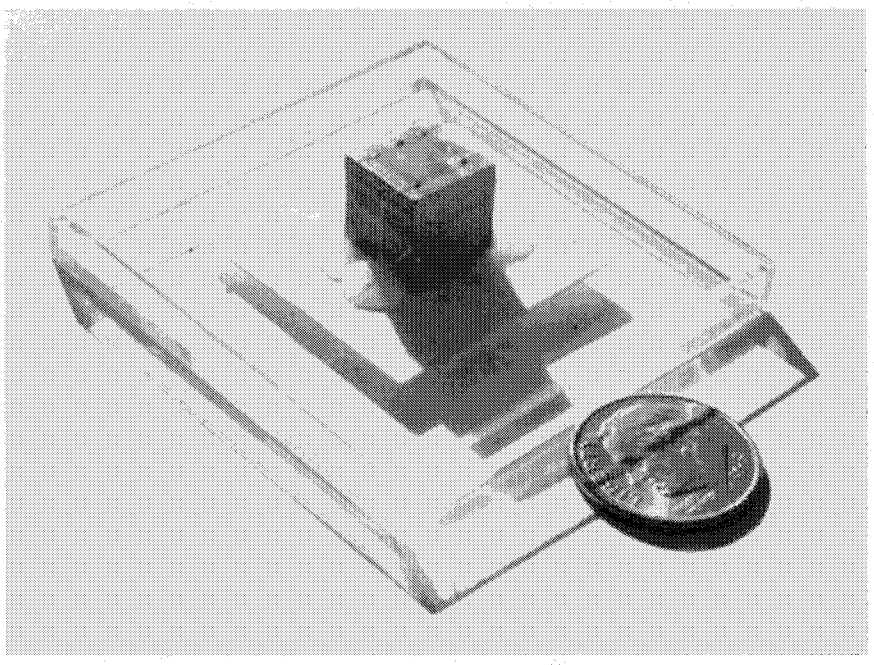

Figure 4.2: Photograph of a pixelated HgI_2 detector.

A photograph of the detector crystal is shown in Figure 4.2. The detector is encapsulated to prevent sublimation of the HgI_2 material. The crystal is glued to a ceramic substrate using the Dow Corning 3140 MIL-A-46146 RTV coating to ease the handling of the detector. Lead wires from each electrode are also glued on the ceramic substrate next to the base of the detector crystal. The detector is then placed in a removable clear plastic box for storage and shipping purposes.

A second anode design was created recently in which the anodes were placed next to each other (see Figure 4.3). This design will allow for the investigation of charge sharing between pixels. The original specification for this design called for the pixel and gap size to be the same as in the first configuration. The large anode now surrounds the outside of the pixel region. A picture of this detector design is shown in Figure 4.4. The packaging of the detector was identical to detectors with the first anode design.

Difficulties with the design occurred with the second anode configuration. The layout of the pixels suffered from two problems. First, the gap between the pix-

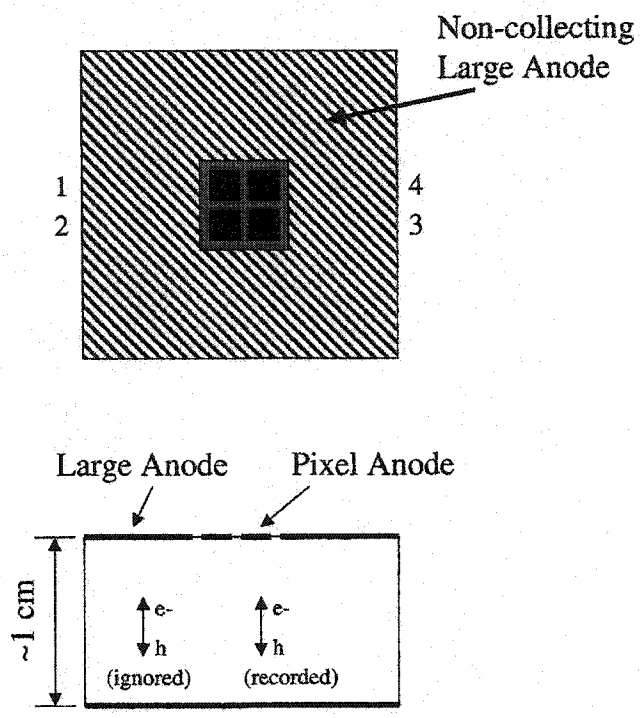

Figure 4.3: Second design for the pixelated HgI_2 detectors.

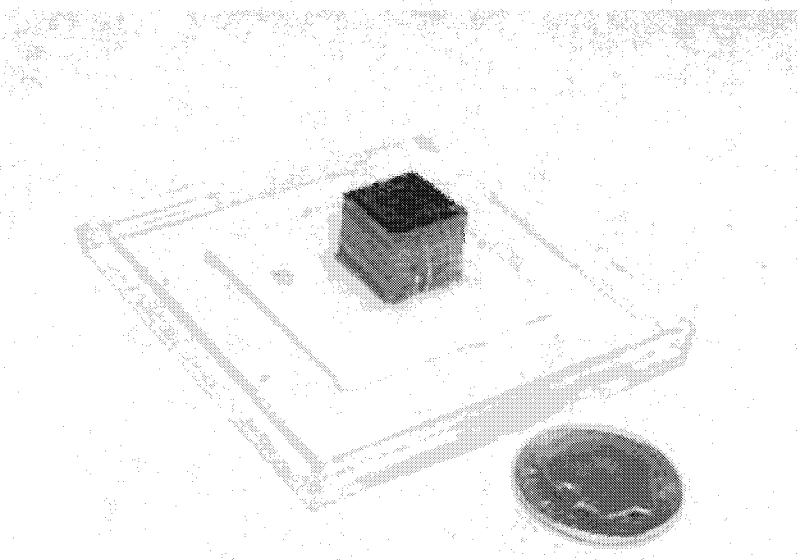

Figure 4.4: Photograph of HgI_2 detectors with the second anode pixel configuration.

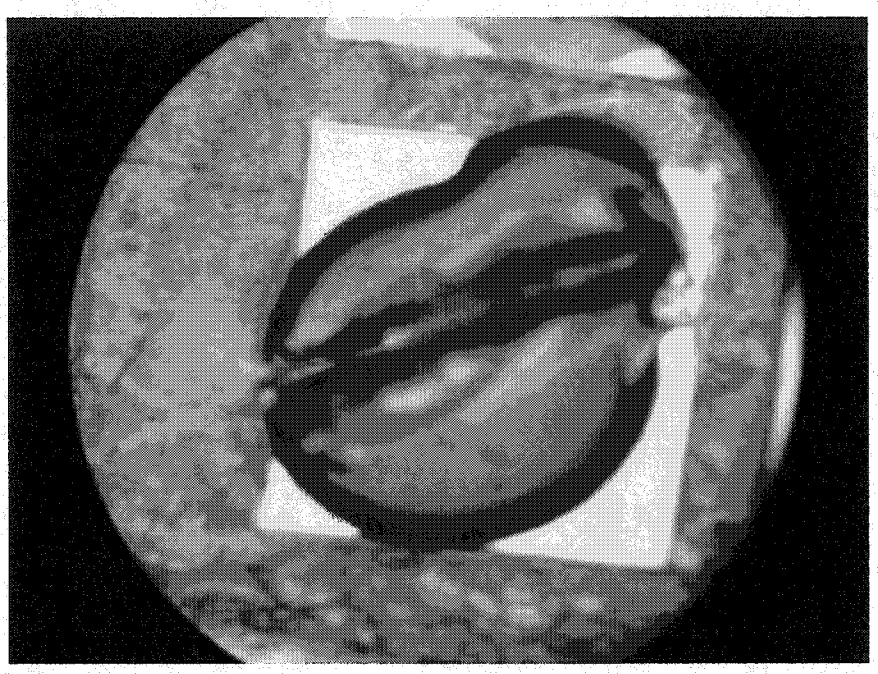

Figure 4.5: Photograph from a microscope of HgI_2 anode pixel structure on the second design. There was an unexpected large gap between the pixel region and the large non-collecting anode.

els and the large surrounding anode was too large (Figure 4.5). Instead of a 150 μm gap, the gap was close to 500 μm in size. The increased gap size causes two problems. First, there will be a larger pitch size leading to an increased depth dependence with the induced charge on the pixel, and an increase in charge sharing between the pixel and large anode due to gamma-ray interactions that occur in the gap region. Second, some of the pixels suffered from poor sputtering of the electrodes. Figure 4.6 shows a magnified photograph of a good pixel. The gap can clearly been seen on all four sides of the pixel. This clearly differs from a poorly sputtered pixel (Figure 4.7). In this figure, the pixel is in direct physical contact with the large anode. Without the gap, this pixel will function as part of the non-collecting anode. Several pixels on different detectors with the new anode layout showed this defect. In the future, improvements should be made to the manufacturing process for the electrodes to eliminate this problem.

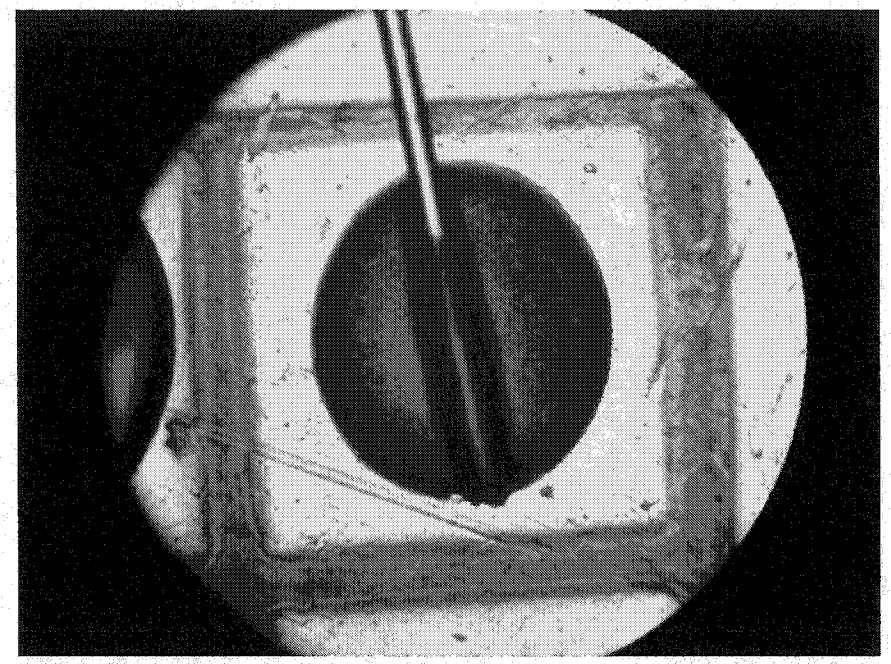

Figure 4.6: Photograph of a well manufactured anode pixel. The thin gap region can be seen on all four sides of the pixel.

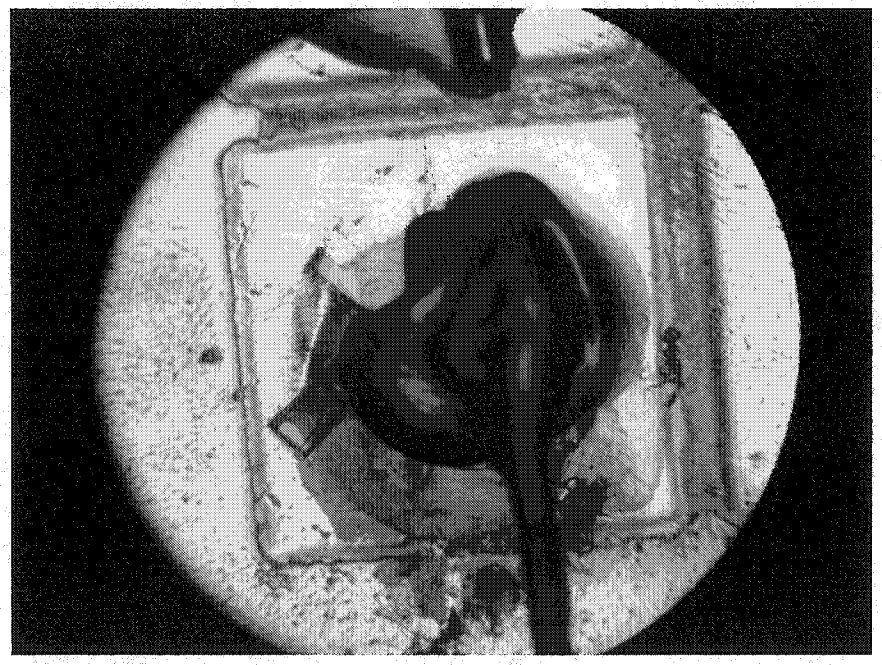

Figure 4.7: Photograph of a pixel in direct contact with the large non-collecting anode. Reading out the signal from the pixel lead wire showed the pixel behaved just like the large anode.

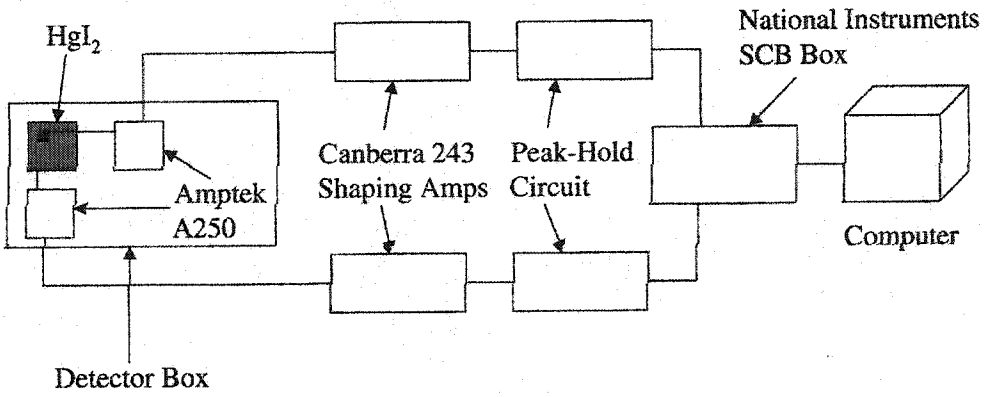

Figure 4.8: Simple block diagram of the data readout system.

4.2 Electronics and Data Acquisition Setup

Figure 4.8 shows a block diagram of the basic electronics setup for the acquisition of data and spectra from the pixelated HgI_2 detectors. Five AmpTek [90] A250 charge sensitive preamplifiers and the detector crystal are placed in an aluminum box (see Figure 4.9) to shield the HgI_2 crystal from light leakage. One preamplifier was connected to the cathode electrode, while the other four preamps were connected to the anode electrodes (either to the 4 pixels or to 3 pixels and the large anode). An additional wire was provided for the other connection on the anode side of the detector. A negative bias was supplied to the cathode, while all anodes were electrically grounded to the aluminum box. In order to study the shapes of the pulse waveforms from the A250 preamps, a Tektronix digital oscilloscope was used.

When performing spectroscopy measurements, only the cathode and one anode pixel signal are used since the focus of this research was single pixel events in the detector (a fully pixelated device would allow for the investigation of gamma-rays that undergo multiple interactions in a single HgI_2 device). The two signals were each connected to Canberra Model 243 shaping amplifiers. This shaping amplifier has a variable gain from 2.5-1500X and a variable shaping time from 1-16

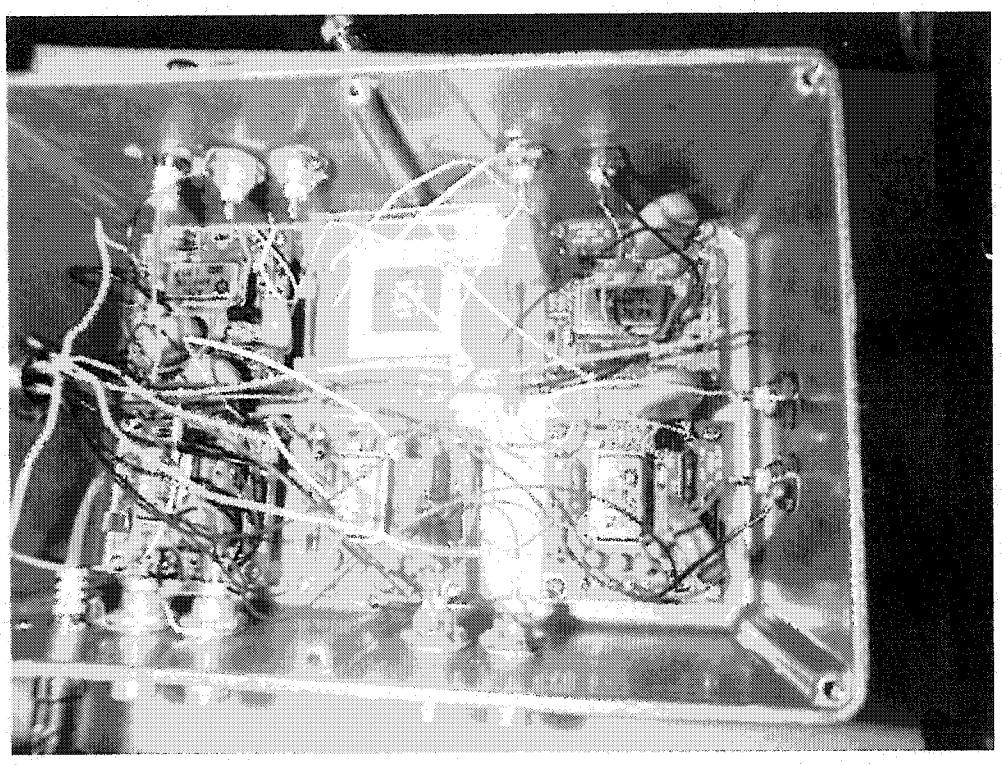

Figure 4.9: Photograph of the aluminum detector box containing the five preamplifiers and the HgI_2 crystal.

μs.

The output pulse of the shaping amplifier is then fed into the peak-hold circuit. The peak-hold circuit functions to hold the peak amplitude of the shaped pulse for a prescribed amount of time before the signal is sampled by the data acquisition board (see Figure 4.10). The peak-hold circuit serves two important functions. First, the circuit holds the peaks long enough such that the peak amplitude of the signal will be sampled by the data aquisition board (DAQ). Second, by holding the peak amplitudes of both the anode and cathode shaped pulses sufficiently long, timing differences between the signals that may arise due to the different weighting potentials of the two electrodes will not cause any error while reading both input pulses to the DAQ (as shown in Figure 4.11). The signals are then input into the DAQ. The peak-hold circuit is then discharged. The data aquisition board used in this work was a National Instruments PCI-MIO-16E Series DAQ board [91]. The DAQ board contains an analog-to-digital converter (ADC) and allows for the use of a digital trigger from an external source, in this case the anode pixel signal.

The data aquisition software used in these experiments was LabView^{TM}. This software package was developed by National Instruments and easily communicates with the DAQ board. A block diagram of the program developed to collect gamma-ray spectra is shown in Figure 4.12. First, the pulses from the planar cathode and anode pixel are read by the program. The cathode to anode signal ratio is calculated. This ratio value is then used to determine the interaction depth. A ratio of 1.0 corresponds to an interaction next to the cathode, while a ratio near 0.5 is from an interaction near the middle of the detector, and a value near 0 corresponds to an interaction near the anode. The program is designed such that the detector is divided into 20 depths. Five extra depths corresponding to a cathode to anode ratio greater than 1 are also recorded. Trapped electrons induce very little signal on the anode pixel, but will induce an appreciable charge on the planar cathode. Thus, it is possible that some events that occur near the cathode will have a ratio slightly greater than 1. These events may be recorded in a depth index of 21 or 22 even though they are true single pixel gamma-ray interactions. Therefore, the total

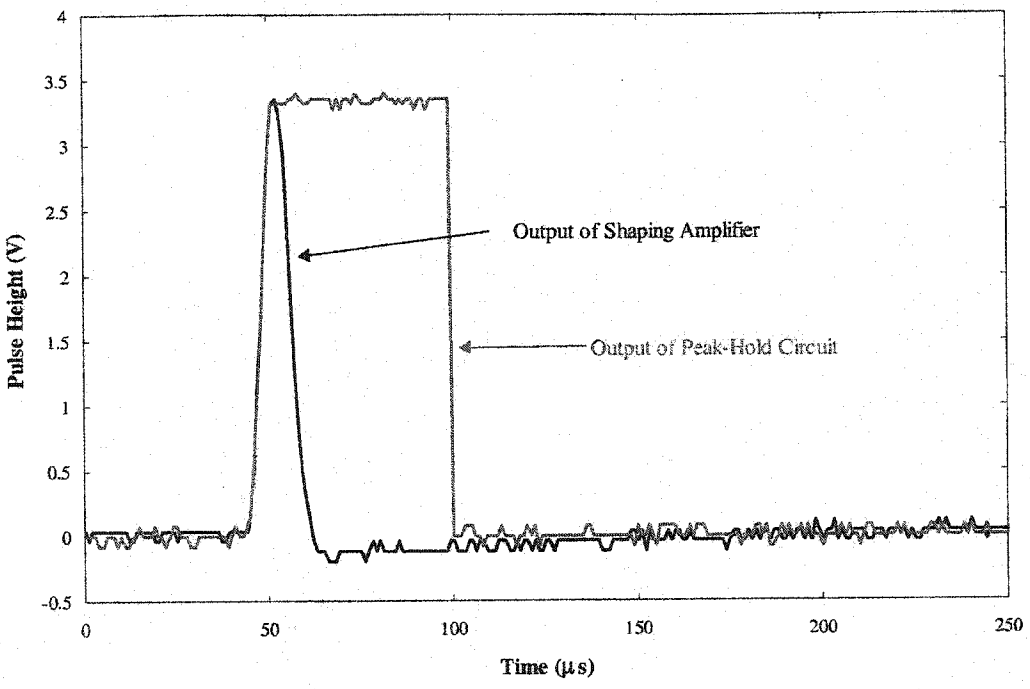

Figure 4.10: The output of the peak-hold circuit maintains the peak amplitude of the input pulse for a significant amount of time before discharging.

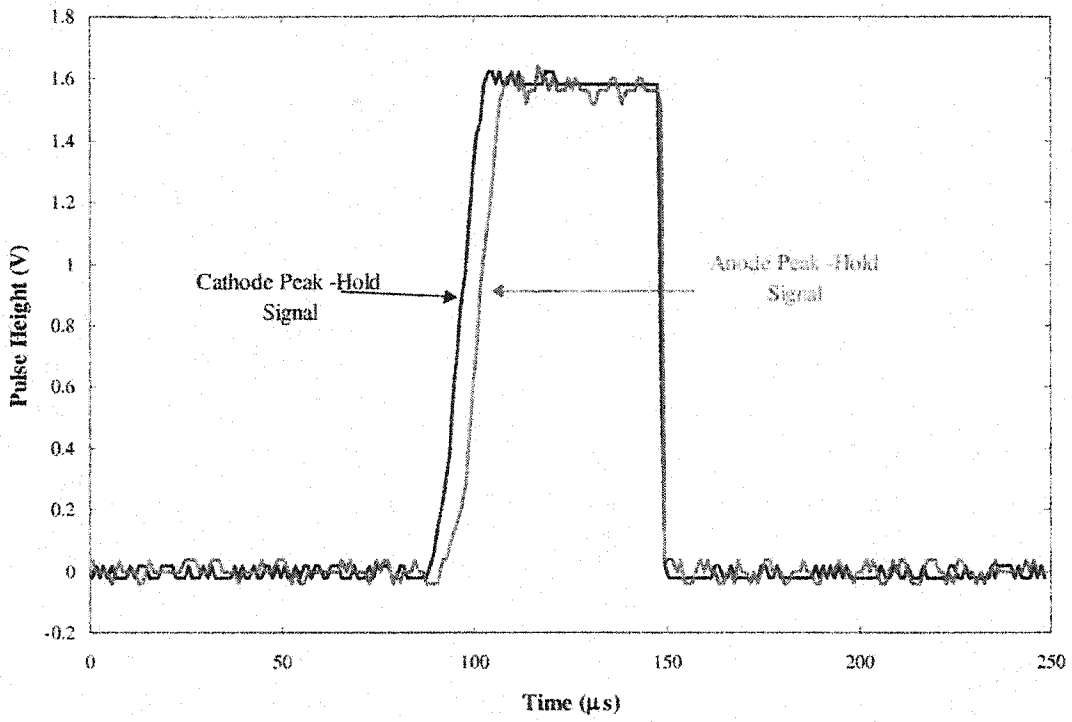

Figure 4.11: The weighting potentials of the planar cathode and pixel anode may cause a slight time difference between the peaks of the two signals. By holding the peak, sampling of the peak amplitude by the DAQ board is ensured for both signals

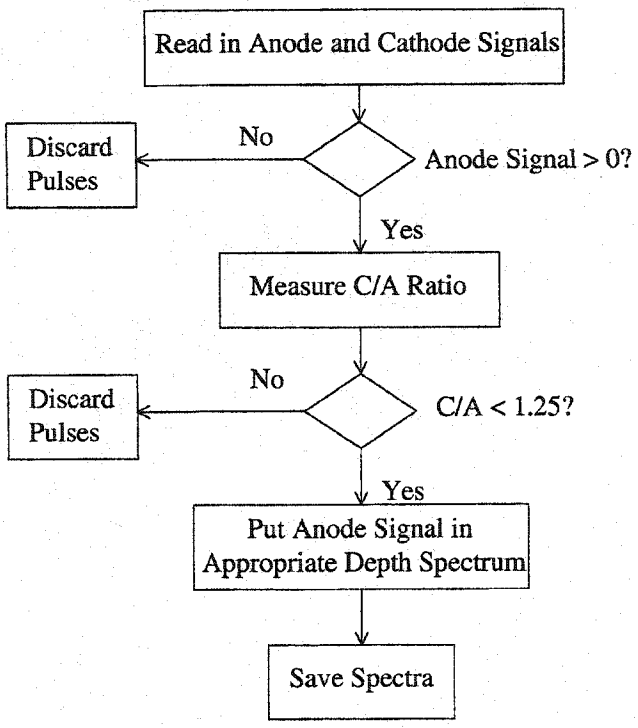

Figure 4.12: Block Diagram of the spectrum collection and depth analysis program.

number of virtual depths recorded is actually 25. If the C/A ratio is greater than 1.25, the event is discarded from the pixel spectrum. Both the depth sensing anode pixel spectrum and the planar cathode spectrum are recorded. For post collection analysis, the spectra files are read into Matlab^{TM}, and several small programs were written to measure the photopeak resolution and perform depth correction. Table 4.1 describes all of the programs written for spectra collection and analysis.

Table 4.1: Programs created for spectrum collection and analysis

Program Name	Software Package	Description
Spectrum depth sense.vi	LabView	Collects anode and cathode spectra, performs depth sensing
read.m	Matlab	Reads in spectra into Matlab, separates anode spectra array into depth spectra
fwhm.m	Matlab	Measures the FWHM of the specified spectrum and photopeak range
depcorr.m	Matlab	Provides depth correction for the anode pixel spectra

Chapter 5

Spectroscopic Results Of Pixelated HgI_2

The most important characteristic for room temperature semiconductor radiation detectors is the ability to produce well resolved energy spectra. The spectroscopic capabilities of pixelated HgI_2 is presented in this chapter. First, the actual pulse waveforms from the charge sensitive preamplifiers for gamma-ray events are described. Next, spectra for the conventional planar cathode are presented. Then, spectra from the anode pixels are discussed for both 5 mm and 10 mm thick HgI_2 detectors. These results show the significant improvement of pixelated anodes over the conventional planar cathode. The incorporation of depth sensing and correction is presented and shows an even further improvement in energy resolution with pixelated detectors.

5.1 Signals From HgI_2 Detectors

In order to verify that the electrode configuration results in an induced charge from the anode pixel rising quickly when the electrons are near each pixel, the signals from the charge sensitive preamplifiers were analyzed. Figure 5.1 shows the induced charge from an event for three electrodes (the planar cathode, and two anode pixels). The pulse height of the cathode and pixel signals were nearly identical, indicating that the gamma-ray interaction occurred near the cathode side of the detector. Thus, only electrons generated by the gamma-ray interaction will induce a charge on the electrodes. The rise of the cathode signal begins at the location of the interaction. However, the anode pixel signal does not begin to significantly rise until the electrons are essentially directly under the pixel electrode. The second pixel signal has a shape similar to the other pixel. However, when

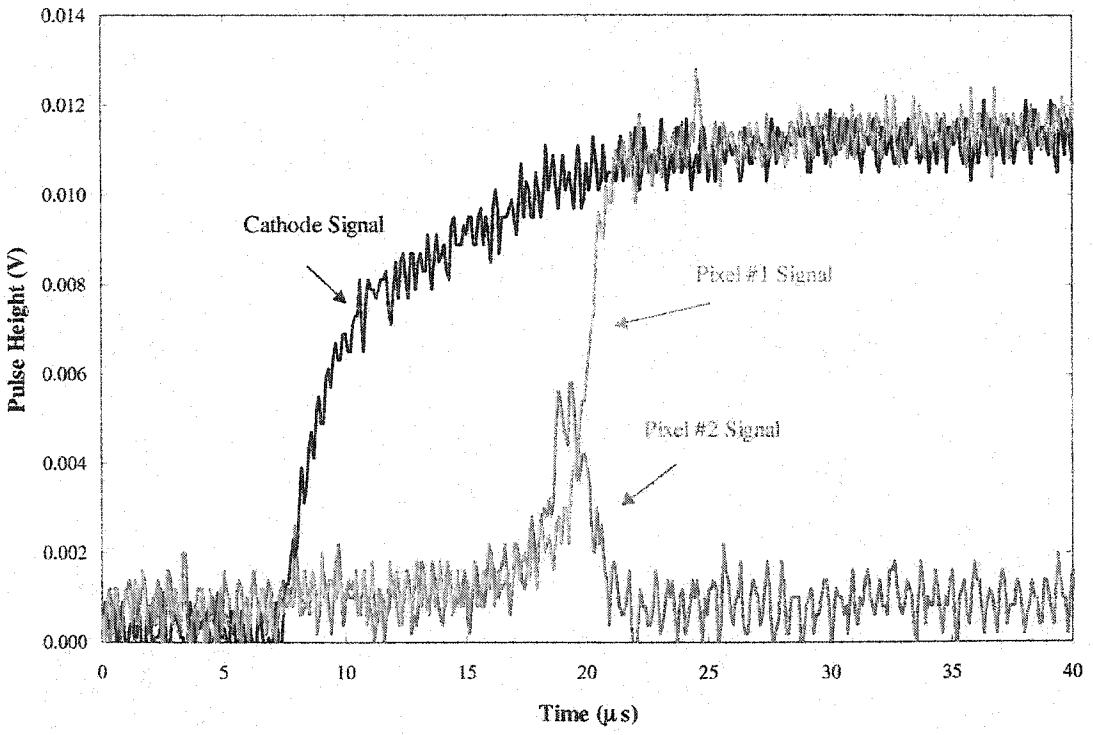

Figure 5.1: Pulse waveforms from the cathode and two anode pixels for a radiation interaction that occurred near the cathode side of a 1 cm thick detector (93203N98 with a cathode bias of -2000V).

the electrons approach the first pixel electrode, the signal on the second pixel will fall quickly. At this point, the electrons are moving away from the second anode pixel and towards the first pixel. Thus, a current of opposite polarity is induced on the second and the pulse produced by the preamp will rapidly return to its original baseline. These pulse waveforms showed that the pixelated anode design will operate properly with detectors made from HgI_2.

Interactions from further within the detector material were observed. Figure 5.2 indicates an example of an event that took place within the bulk of the detector. In this case, the cathode signal is significantly lower than the anode pixel signal due to the lack of any signal produced by the movement of holes with HgI_2 (poor mobility and severe trapping). Thus, the cathode signal can be used to indicate the depth of the gamma-ray interaction while using the pixel signal to determine the

energy deposited by the event. The surrounding large anode signal initially rose in similar fashion to that of the cathode electrode (the surrounding large anode has a shape similar to the cathode, so it should have a nearly identical weighting potential). As the electrons approach the pixel, the weighting potential of the large surrounding anode quickly returns to zero. Thus, similarly to the second pixel in Figure 5.1, the current on the large aonde became negative, and the induced charge on this electrode quickly decreased. Due to the fact that the event in Figure 5.2 took place in the middle of the detector, the baseline of the large surrounding anode became negative with respect to the original baseline prior to the gamma-ray event within the detector. Due to the weighting potential of the large anode, the charge induced on the large anode from the electrons moving towards the anode side of the detector (with the electrons within the bulk of the detector) is significantly less than the opposite charge induced on the large anode when the electrons are collected by the anode pixel (moving away from the large anode) for this interaction. The baseline of the large anode eventually returned to 0, in accordance with the 300 μs time constant of the preamplifier.

While the above event showed that (nearly) all of the electrons are collected by the anode pixel, other gamma-ray interactions showed positive signals on more than one anode electrode. Figure 5.3 depicts an event in which some of the electrons produced from the gamma-ray interaction are collected by the large anode. In this case, the new baseline of the large anode was higher than expected due to the collection of electrons on the large anode. Charge sharing between pixels was also observed, and an example is shown in Figure 5.4. In this case, two pixels show a similar rise of their respective signals. The example shown indicates that about 60% of the charge was collected by the pixel that produced the trigger, while 40% of the electrons were collected by an adjacent electrode. The significant charge sharing between the pixels may indicate that the radiation interaction took place within the gap region between the two pixels.

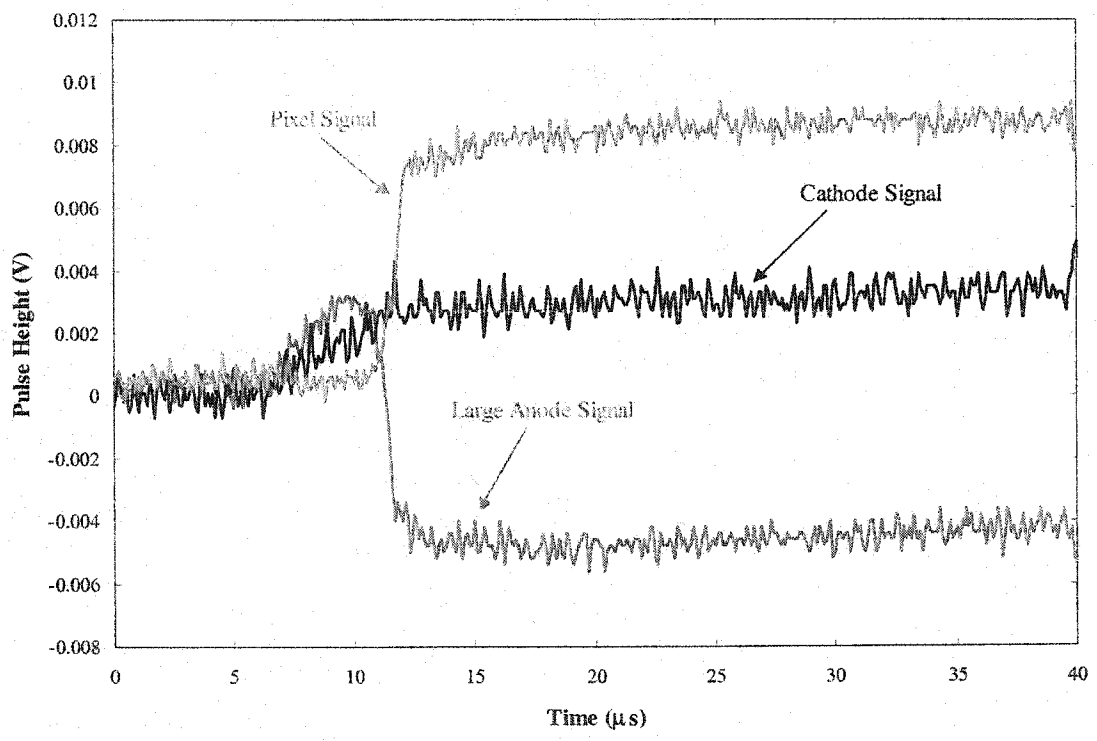

Figure 5.2: Pulse waveforms for an event in the middle of the detector. While the pixel signal was independent of the depth of interaction since the signal is induced only when the electrons are near the pixel, the cathode signal showed a near linear dependence with the interaction depth.

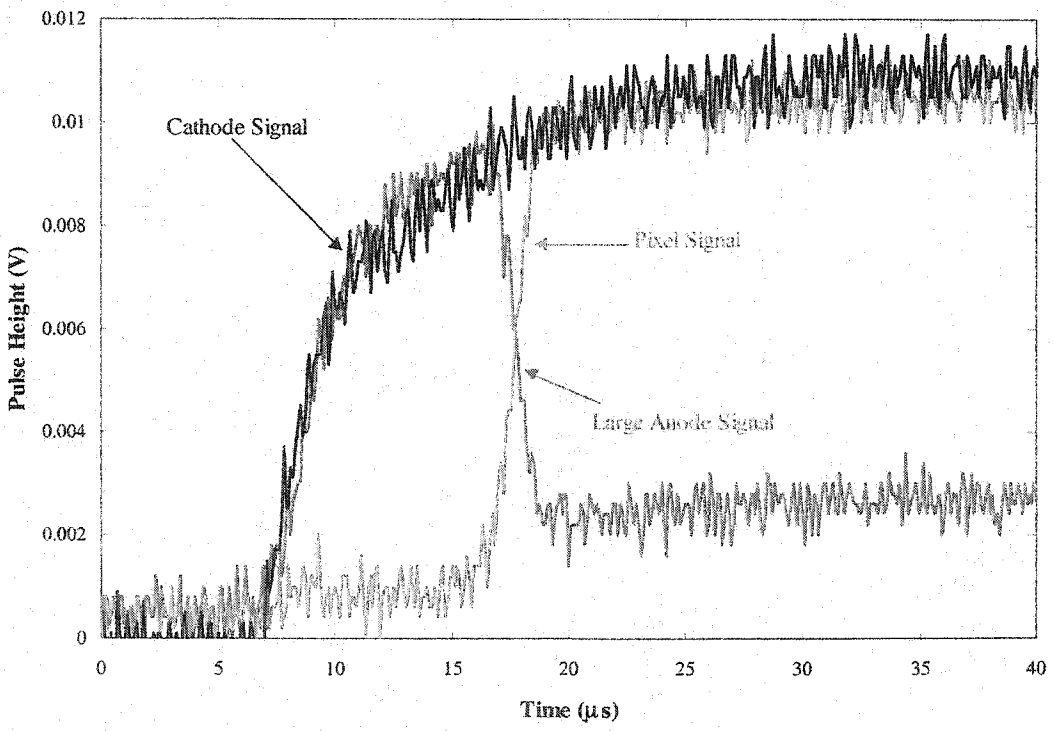

Figure 5.3: Pulse waveforms from an event where some of the electrons were collected by the large anode. This is indicated by the slightly positive baseline of the large anode after the electrons were collected by the anodes. Note that the interaction took place near the cathode side of the detector, as indicated by the prominent cathode signal.

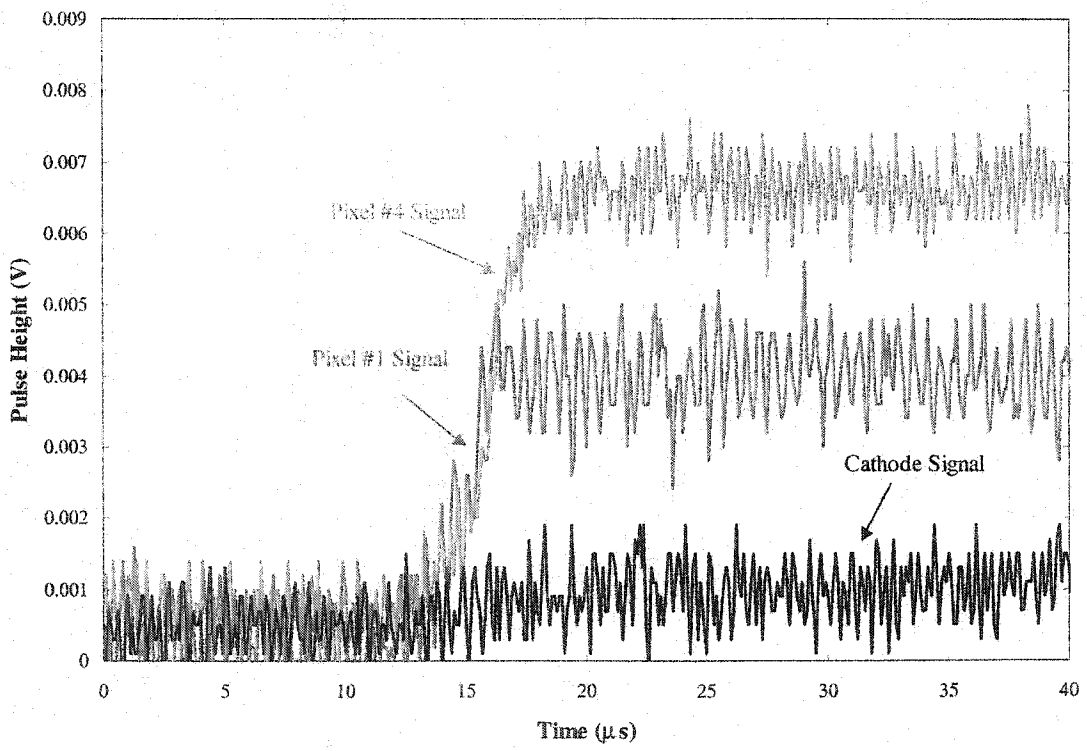

Figure 5.4: Charge sharing between pixels was also observed. Two adjacent pixels show a signal for an event that occurred near the anode side of the detector (as indicated by the lack of a cathode signal).

5.2 Spectra Obtained From the Cathode

The cathode spectra were obtained in order to observe and collect spectra using a conventional planar electrode. A Cs-137 spectrum from a 10 mm thick HgI_2 is shown in Figure 5.5. The spectra collection software was triggered by the cathode signal, thus the entire volume of the detector (not just the pixel volume) was used to obtain the spectra. The 662-keV photopeak inherent to Cs-137 cannot be seen in the spectra. Despite the long shaping time used in this measurement (16 μs), the severe hole trapping and low hole mobility associated with HgI_2 will prevent the holes from producing any significant signal on the cathode (as explained earlier in Chapter 2). In order for the holes to move a larger fraction of the detector volume, a spectrum from a 5.79 mm thick detector was obtained (see Figure 5.6). Despite using the same shaping time and applied bias of -2500 (to increase the electric field), no appreciable 662 keV photopeak was observed in the thinner detectors, either. Thus, good energy resolution of moderate gamma-ray energies cannot be obtained with thick HgI_2 detectors using planar electrodes.

In order to obtain a photopeak with sufficient energy resolution using HgI_2 detectors with conventional planar electrodes, the detector must be very thin (less than 1 mm) with a large detector bias and long shaping times must be used. The large electric field and short distance holes would have to travel will allow for relatively efficient charge collection. However, there will be a significant loss of detection efficency with thin detectors. It is possible to use pulse processing techniques with thicker HgI_2 detectors [12]. However, these techniques will also suffer from a poor S/N ratio for many of the events that occur closer to the anode side of the detector. Thus, only a small fraction of the HgI_2 detector volume will contribute a good signal to the photopeak [86], and the efficiency of these detectors will suffer. In general, HgI_2 incorporating conventional electrodes are limited to less than 3 mm in thickness using large shaping times and high electric fields. If good detection efficiency and good energy resolution is required, only pixelated anodes can be used with thick HgI_2 detectors.

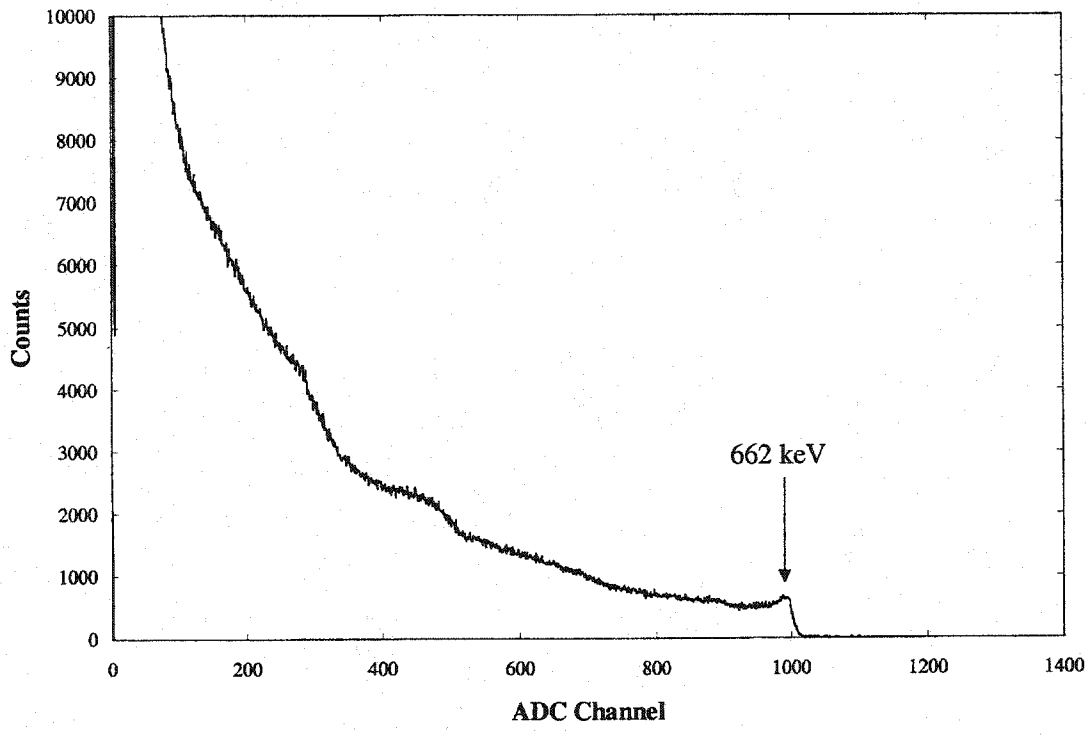

Figure 5.5: Cs-137 spectrum obtained from the planar cathode electrode of a 10.05 mm thick HgI_2 detector. The applied bias on the cathode was -2500 V and the shaping time used was 16μs. Note the lack of photopeak for the 662 keV gamma-ray associated with the decay of Cs-137 due to low hole mobility and severe hole trapping. Even if hole trapping was not present, the holes would only travel about 1 mm in 16 μs.

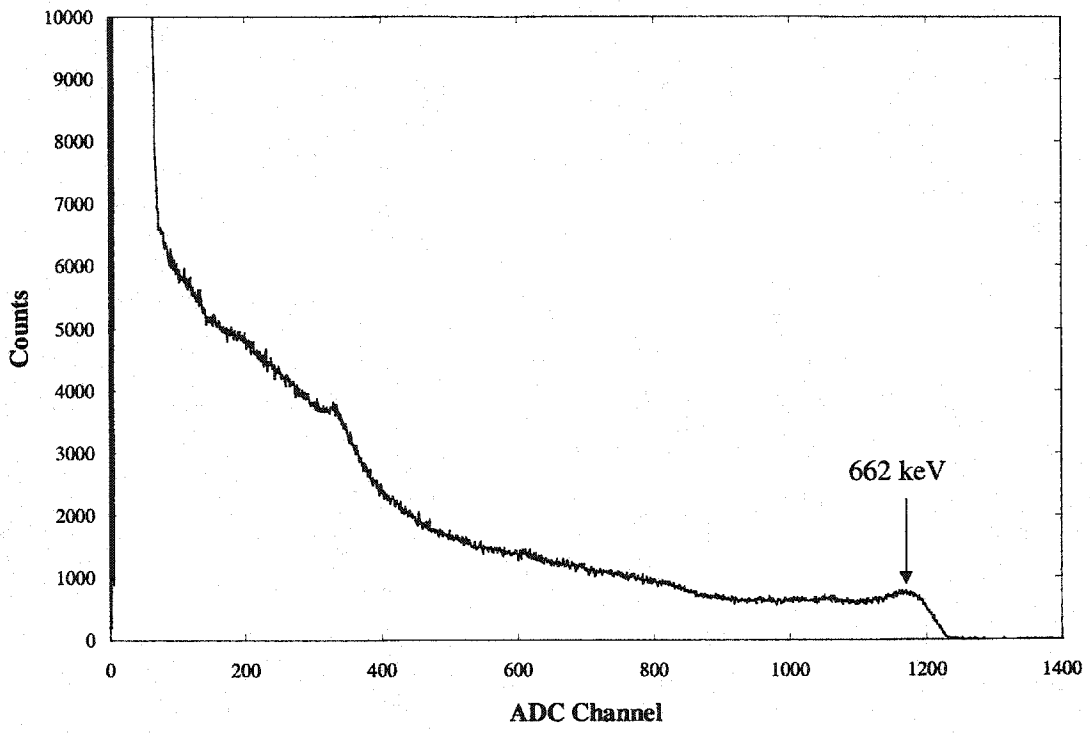

Figure 5.6: Cs-137 spectrum from a planar cathode of a 5.79 mm thick HgI_2. Despite using the same detector bias and shaping times as the 10 mm thick detector, the spectrum still lacked the 662 keV photopeak.

5.3 Spectra Obtained From 5-6 mm Thick Pixelated Detectors

Two detectors were used for these measurements. Detector 92512Q92 had a thickness of 5.79 mm, while Detector 93203N95 had a thickness of 6.29 mm. Each detector had pixels approximately 1 cm^2 in area with a suurounding gap of 150 μm wide. Each Cs-137 spectra was obtained over a 22 hour collection time. Only single pixel events were recorded. If the C/A ratio exceeded about 1.25, which could happen if there were multiple interactions outside of the pixel region or a significant amount of charge sharing, the event was ignored. The shaping time was varied for both the cathode and anode signals in order to obtain the best resolution. In most cases, the best results were obtained with a shaping times of 4 μs (peaking time of 8 μs, which corresponds to the approximate electron drift time from the cathode to anode side of the detector.

Figure 5.7 shows a Cs-137 spectrum obtained from pixel *No.*2 of Det. 92512Q92 accounting for only the weighting potential of the pixel. The spectrum shows a very broad energy resolution at 662 keV of approximately 13.5%. The energy resolution of each pixel on the detector widely varied from about 5.9% (pixel *No.*4) to about 14% (pixel *No.*1). By measuring the C/A ratio, the pixel region was divided into approximately 20 depths. The spectra as a function of depth index is shown in Figure 5.8.

As can be seen in Figure 5.8, a sharp photopeak for the 662 keV gamma-ray was observed for many depth indices. The peak area as a function of depth index is shown in Figure 5.9. The area remained relatively constant over the entire thickness of the detector, however Depth Index 20 (the depth adjacent to the cathode) had an area approximately twice that of any other depth. This large area can be attributed to the small amount of hole movement present in HgI_2. For events near the cathode, the holes can be collected, and the C/A signal ratio will be close to 1.0 for a larger fraction of the detector thickness. Thus, the depth index next to the cathode will have a larger effective volume than others and the photopeak area will be comparatively large. It should be noted that it was expected that a $e^{-\mu z}$

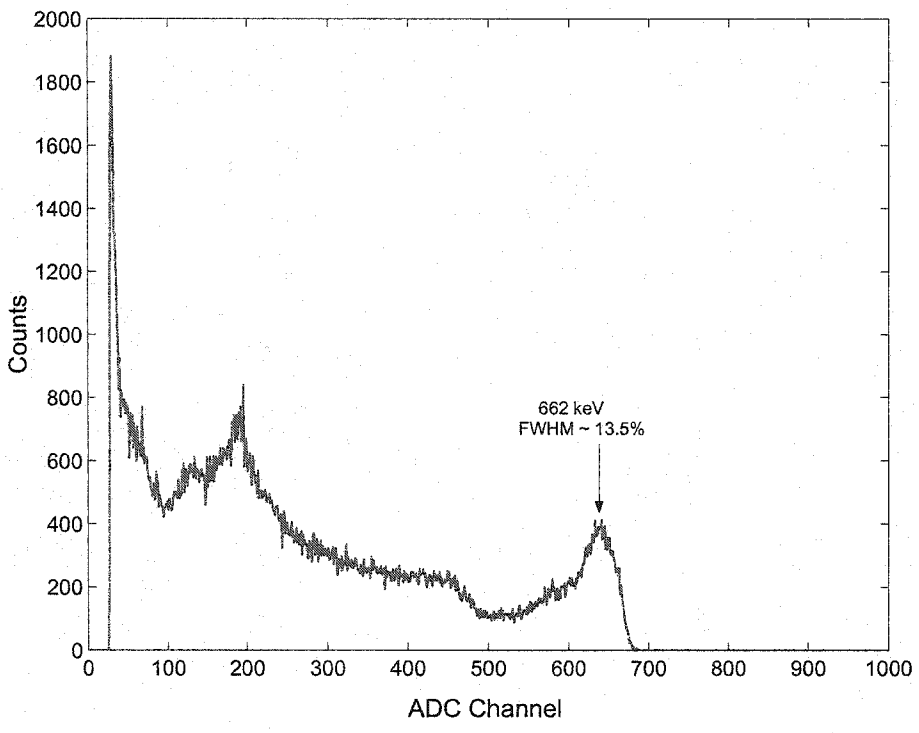

Figure 5.7: Cs-137 spectrum collected over 22 hours from pixel *No.*2 on Detector 92512Q92 (5.79 cm thick). The anode shaping time was 4 μs. While the photopeak was very broad, there was an improvement over the resolution using conventional electrodes.

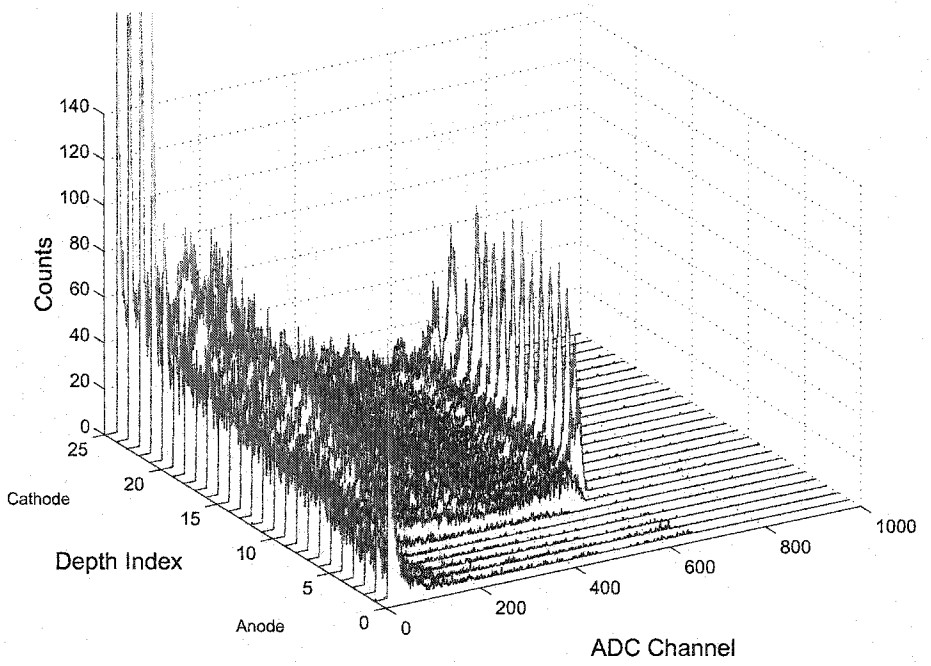

Figure 5.8: Cs-137 spectrum collected over 22 hours from pixel *No.*2 on Detector 92512Q92. The use of depth sensing by measuring the C/A ratio allows the spectra to be divided according to the depth of gamma-ray interaction.

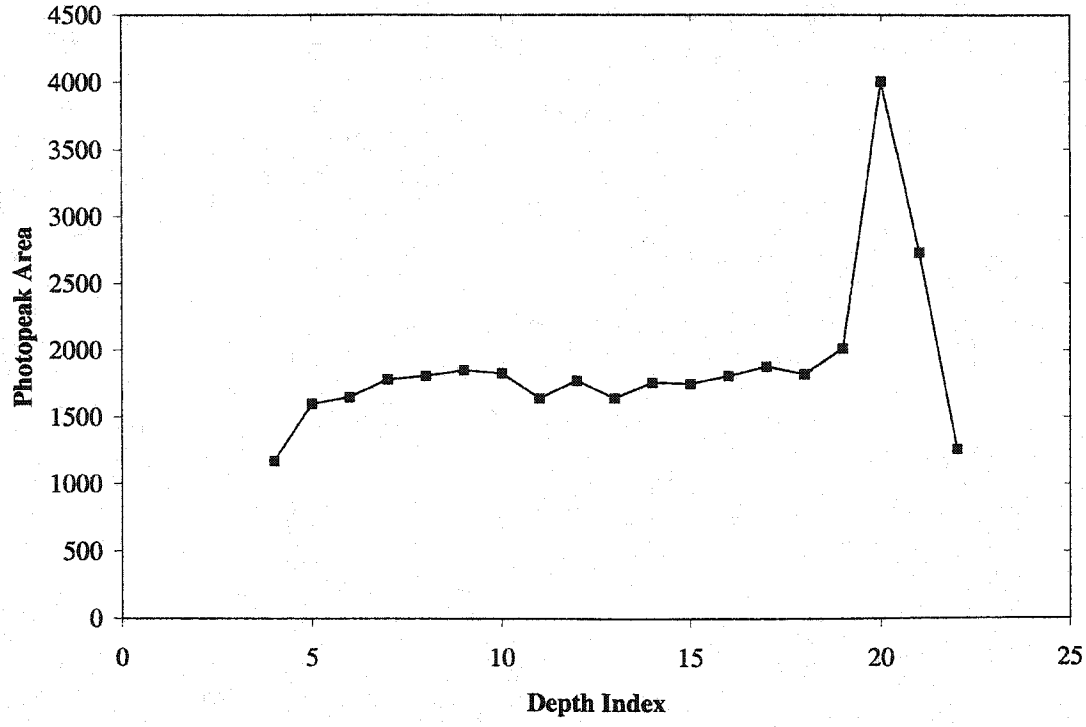

Figure 5.9: Cs-137 photpeak area as a function of depth. The large area at depth index 20 was due to the small amount of hole movement present in HgI_2. This hole movement caused the effective thickness of the depth index adjacent to the cathode to be much larger than the other depth indices. An expontential shape to the curve was expected, but the increased charge sharing for events closer to the cathode may have decreased the effective pixel volume for depths closer to the cathode.

shape was also expected with the photpeak area as a function of depth, due to the exponential attenuation of the source. This was not observed and may be due to the increased charge sharing that will occur from photopeak events near the cathode. The effective volume of a depth index near the cathode (e.g., 15) may actually be smaller than one closer to the anode (e.g., 8), and the attenuation of the source may not necessarily be completely observable.

The peak around channel 180 (seen in Figure 5.7) is much more prominent at depths closer to the cathode side of the detector. This peak is a backscatter peak that can be attributed to the surrounding materials, in particular the wood desk the detector box rests upon. The desk is below the detector cathode, and therefore the

backscatter count rate is much larger at the cathode side of the detector since the lower energy backscatter gamma-ray is absorbed in a shorter distance than higher energy gamma-rays.

The resolution of the photopeaks as a function of depth index was much better than the overall resolution of the pixel (see Figure 5.10). The resolutions of most of the small pixel voxels was near 2% (approximately 13 keV). Only near the anode side of the detector did the resolution significantly degrade due to the large depth dependence of the weighting potential near the anode. The poor resolution of the overall peak was due to the variation of the photopeak position as a function of the interaction depth. Figure 5.11 shows the photopeak position as a function of depth index. The increase in photopeak position as the interaction position got closer to the cathode was due to the weighting potential having a significant slope throughout the HgI_2 detector thickness.

Incorporation of the depth sensing and depth correction was performed by aligning the photopeak centroids from each individual depth index to a particular ADC channel. The photopeak resolution was dramatically improved to approximately 2.1% (Figure 5.12). While many of the individual depths showed a better resolution, the depths near the anode side of the detector slightly degraded the overall depth corrected resolution. In addition to the resolution improvement, the number of events in the Compton continuum was also slightly reduced. Depth indices where no counts are observed in the photopeak were automatically eliminated by the software since they would not contribute to the photopeak. Depth correction also allowed the Hg escape peak to be observed approximately 83 keV below the true photopeak. Analysis of all four pixels showed that depth correction improved the resolution for all four pixels (see Figure 5.13), although one pixel (pixel *No.*1) did not have significant improvement since the resolution was poor throughout the pixel volume (all depths had poor resolution).

A second (6 mm thick) detector was also tested using a Cs-137 source. The overall resolutions of all four pixels for this detector are shown in Figure 5.14. This detector had better resolutions for all working pixels (one pixel did not produce

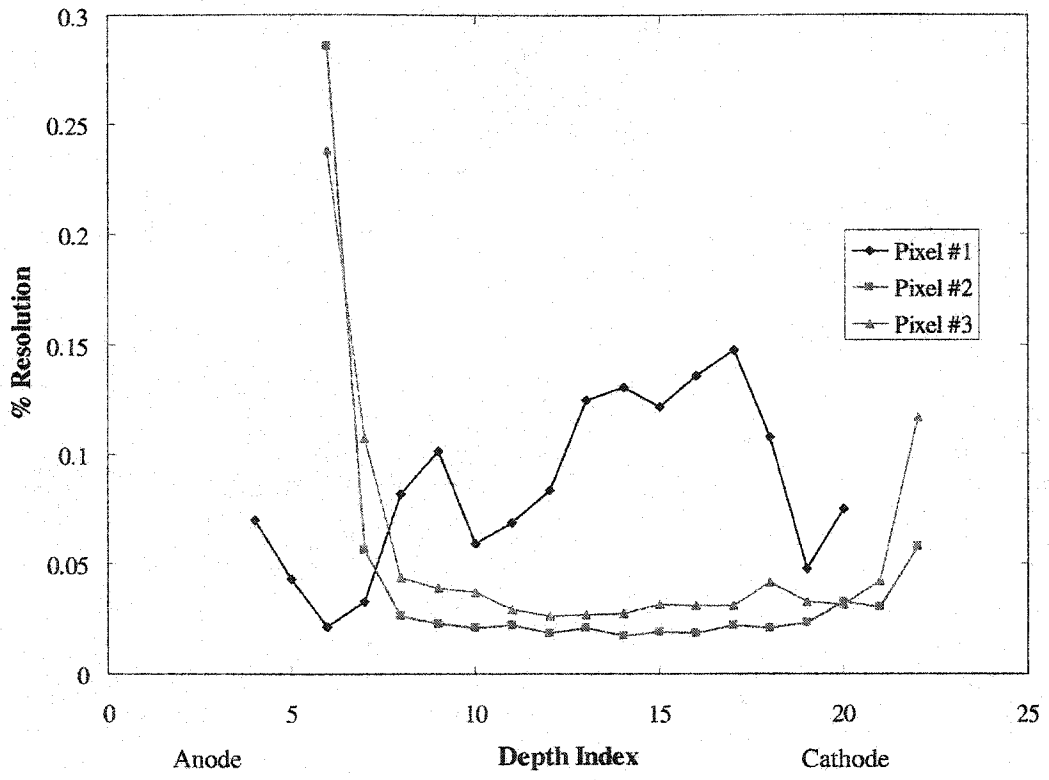

Figure 5.10: Cs-137 photopeak resolution as a function of depth index for several pixels on Detector 92512Q92. The resolution remains relatively constant over the majority of the thickness of the detector for two pixels. One pixel shows a severe variation (and much worse) resolution over each depth index, possibly due to poor HgI_2 material in this pixel region.

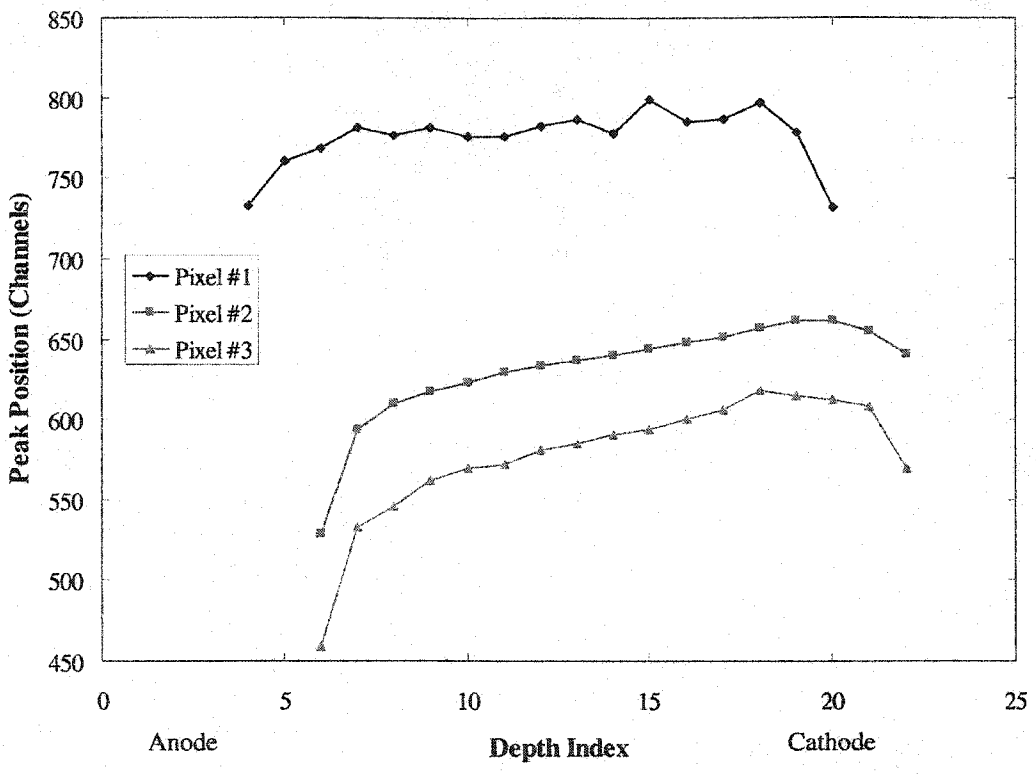

Figure 5.11: Cs-137 peak position as a function of depth index. The increase in peak position as the interaction takes place closer to the cathode was due to the slight depth dependence on the weighting potential outweighting any electron trapping effects.

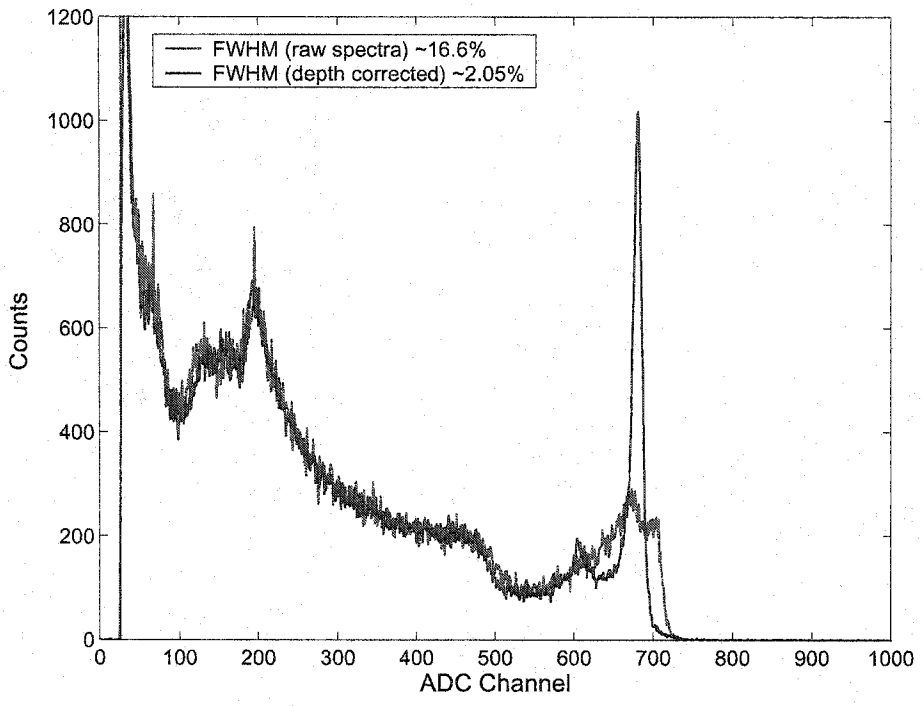

Figure 5.12: Cs-137 spectra from pixel *No.*2 of detector 92512Q92. The incorporation of depth correction dramatically improved the photopeak resolution. The peak near channel 190 can be attributed to backscatter events from outside materials.

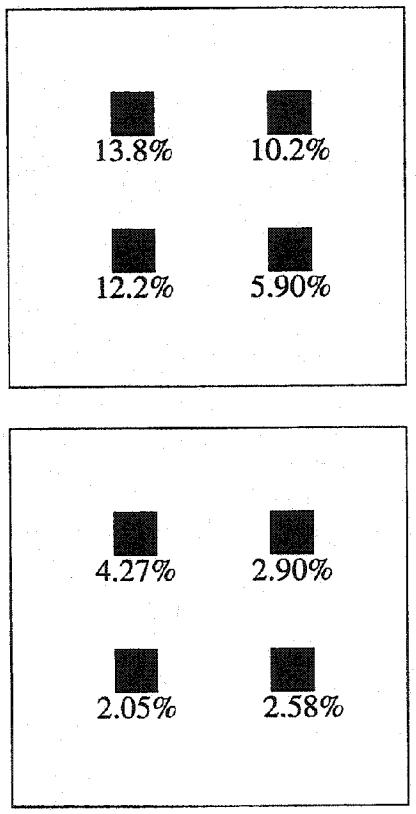

Figure 5.13: Top: The best measured Cs-137 photopeak resolution from all four pixels of detector 92512Q92 without depth correction. Bottom: With depth correction, the resolution improved for all four pixels.

a signal). The detector generally showed a more uniform induced charge on the pixels as a function of the interaction depth. This can be observed in Figure 5.15 where the photopeak position remained at a relatively consistent position (much more so than detector 92512Q92). The resolution at individual depths was shown to be better, and a resolution less than 1% was also observed for one depth index (Depth Index 6) of pixel *No.*2. This particular depth index corresponds to interactions that occurred near the anode side of the detector, where charge trapping and charge sharing will not affect the pixel signal, but far enough from the pixel whereby the sharp slope of the weighting potential will not force a depth dependence on the induced charge. A depth corrected resolution less than 2% was observed on one pixel of this detector. Figure 5.16 represents the best pixel on this detector, with a depth corrected resolution of approximately 1.6%, and represents the best observed resolution for any pixel on the thinner (less than 1 cm thick) HgI_2 detectors. Of the seven pixels tested on the two 5-6 mm thick detectors, five had depth corrected resolutions better than 3%.

5.4 Spectra Obtained From 10 mm Thick Pixelated Detectors

From calculations shown in Chapter 2, the induced charge of anode pixels for thinner detectors show a larger depth dependence. Thus, if thicker (approximately 10 mm) were used, the induced charge on the detector should be more uniform across the entire pixel volume assuming no trapping or material effects. In addition, thicker detectors will also be much more efficient in detecting gamma-ray several hundred keV or larger. Therefore, 1 cm thick HgI_2 detectors should have both better resolution and detection efficiency. Three detectors slightly better than 1 cm thick were used in these measurements. Two detectors (93203N91 and 93203N92) had their pixels separated from each other by 4 mm (see Figure 4.1), while the other detector (93203N98) had the four pixels adjacent to each other within the center of the detector.

Figure 5.17 shows the spectra for each depth index of detector 93203N91, pixel *No.*4. Similar to the previous detectors, the majority of the depths indices show

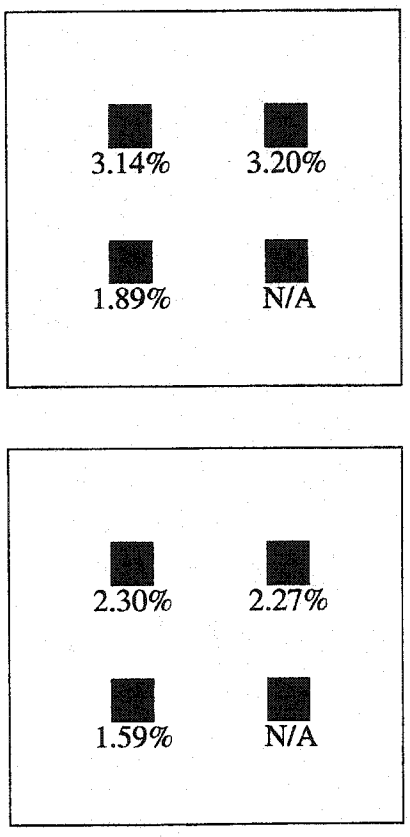

Figure 5.14: Top: The best measured Cs-137 photopeak resolution for the three working pixels of detector 93203N95 (6.29 cm thick) without depth correction. Bottom: With depth correction, the resolution improved for all three pixels, including one where the resolution improved to less than 2%.

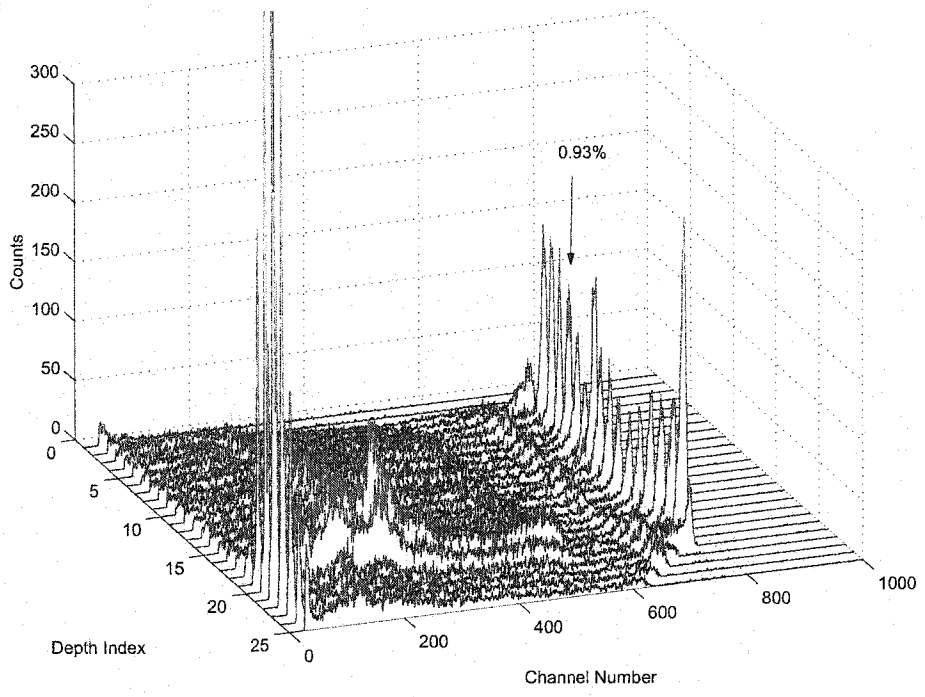

Figure 5.15: Depth resolved Cs-137 spectra of detector 93203N95, pixel *No.*2. The photopeak position did not have as a severe depth dependence compared with detector 92512Q92 (any pixel). The resolution was also slightly better at most depths, including a resolution of 0.93% at depth index 6 (near the anode side of the detector).

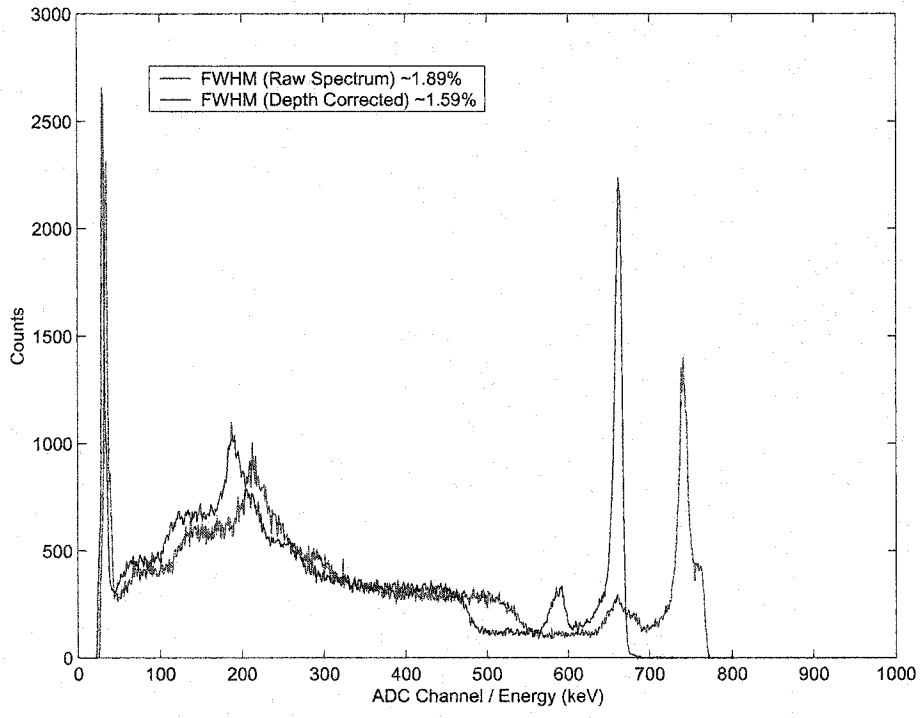

Figure 5.16: The best observed resolution for a 5-6 mm thick detector was from detector 93203N95, pixel *No.*2 with an anode and cathode shaping time of 4 μs. The depth corrected resolution was 1.59%.

a strong photopeak. As with the 5 mm thick detectors, a Hg escape peak can be observed for many depths. However, the 10 mm thick detector has a photopeak associated with more depth indices closer to the anode pixel. Due to the larger thickness, only about 10 percent of the detector thickness is within the pitch region of the pixel (approximately 1 mm) as opposed to the 5 mm thick detector where nearly 20% is within the pitch region. This is the region where the depth dependence of the induced charge on the pixel is severe. Therefore, a photopeak can be observed beginning with depth indices 2 and 3 for a 10 mm thick detector as opposed to depth index 5 or 6 for the thinner detectors. The photopeak position and resolution as a function of depth index are shown in Figure 5.18. The peak position initially increased as the interaction position occurred further from the anode side of the detector due to the increase in the induced charge on the pixel from the weighting potential. However, after around depth index 8-10 for each pixel on the thick detectors, the peak position would slightly decrease at the interaction location occurred closer to the cathode side. For the thicker (1 cm detectors), electron trapping and charge sharing can play a larger role in determining the induced charge on a pixel. As the interaction location occurs closer to the cathode, more electrons will be trapped in the detector material. Thus, the number of electrons collected by the anode pixel will be reduced. For a thick detector where the weighting potential is relatively flat throughout the majority of the detector, the signal reducing effect of electron trapping can counter signal increasing effect of the weighting potential. Therefore, the induced charge on the anode pixel can be smaller for interactions near the cathode than the middle of the detector, as shown in Figure 5.19.

Analysis of the Cs-137 spectra from the three detectors revealed that the photopeak resolution for many of the pixels on the 10 mm thick detectors was very good with values less than 4% for many of the pixels (Figure 5.20) even without correcting for the depth of interaction. Depth correction was also performed with the 1 cm thick HgI_2 detectors. Figure 5.21 shows the Cs-137 spectrum with the best measured resolution for a 1 cm thick HgI_2 detector. It should be noted that

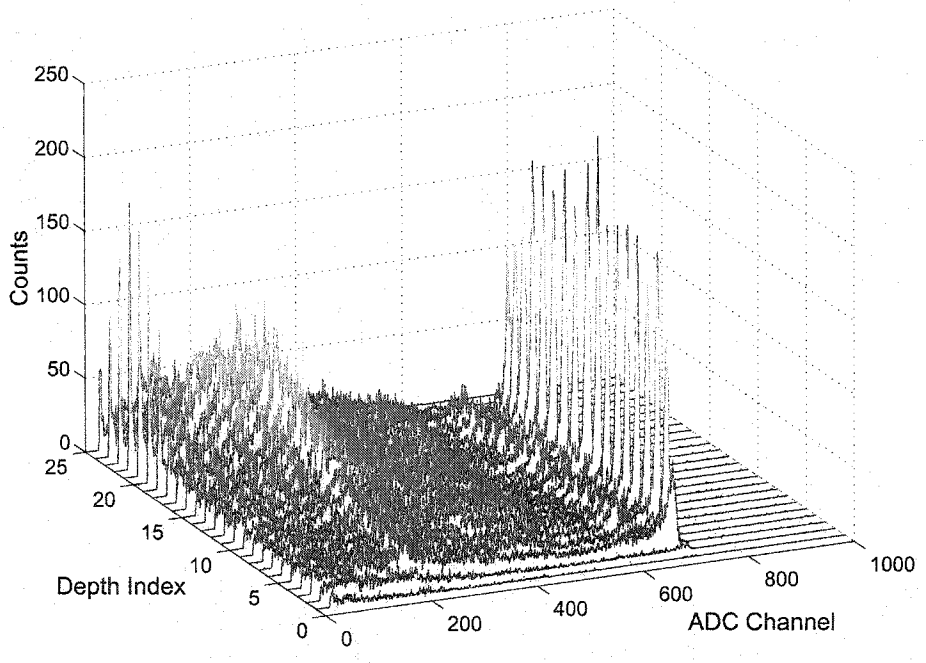

Figure 5.17: Depth separated Cs-137 spectra from detector 93203N91 (thickness of 1 cm), Pixel *No.*4.

this resolution would not be possible with this thickness of detector using only conventional planar electrodes, due to the lack of hole movement in the detector (as shown earlier). In the spectra shown here, the uncorrected spectrum has what appears to be a double peak around the 662 keV region. This is due to a material defect in the middle of the detector (a sudden drop in the photopeak centroid in the middle of the pixel volume was observed with this pixel). Fortunately, depth correction can eliminate this double peak feature by aligning the peak centroids at the same energy. Thus, the Cs-137 photopeak resolution was improved from 3.03% to 1.38%. Figure 5.22 shows the measured depth corrected resolution for all pixels tested on the 1 cm thick detectors. Eight of the eleven pixels had an observed photopeak resolution less than 2%.

5.4.1 Observation of the Iodine Escape Peak

When charge sharing between anode electrodes is not severe, the low energy tailing of the 662 keV photopeak will be small. Thus, the low energy Iodine escape

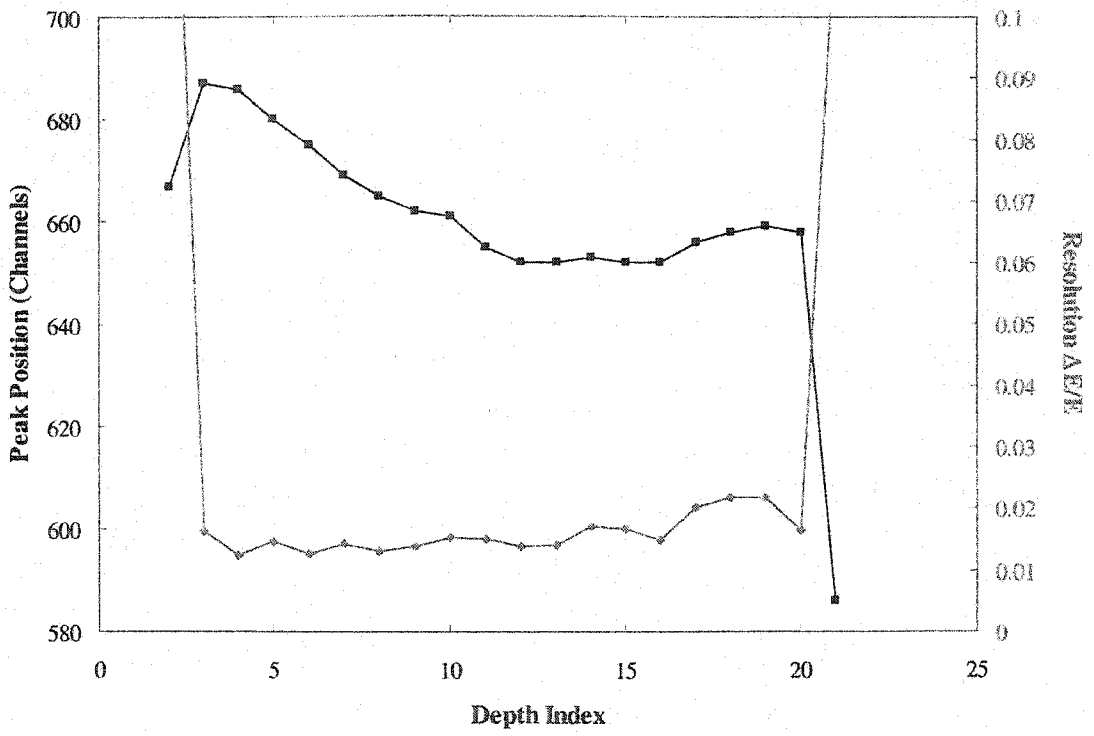

Figure 5.18: Peak position and resolution as a function of depth index for detector 93203N92 (1 cm thick), pixel *No.*4. The resolution at each depth index is nearly always below 2%. The peak position decreases as a function of depth index, suggesting electron trapping and charge sharing are dominant effects on the induced charge for a pixel on thick detectors.

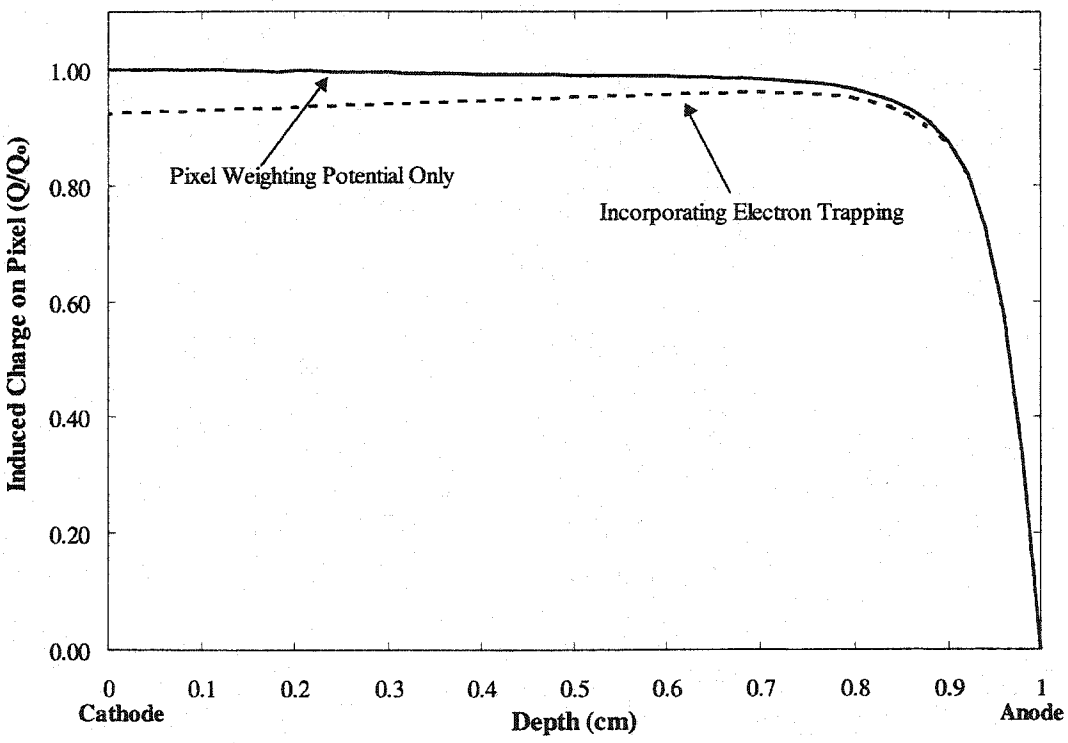

Figure 5.19: The induced charge on an anode pixel with and without electron trapping. For the case where approximately 10% of the electrons are trapped for an event from the cathode side of the detector, the induced charge for an event near the cathode is actually smaller than for an event in the middle of the pixel volume.

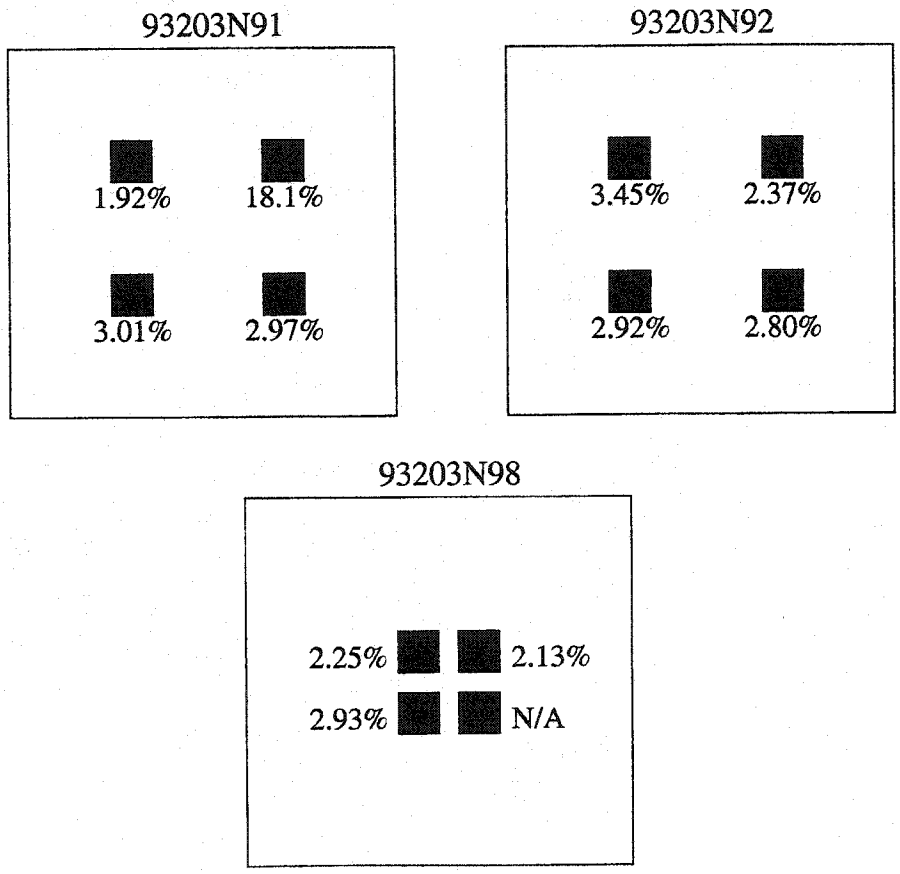

Figure 5.20: Non-depth corrected Cs-137 resolution for all three 10 mm thick detectors tested in this work. Pixels depicted N/A represent pixels that did not have a signal.

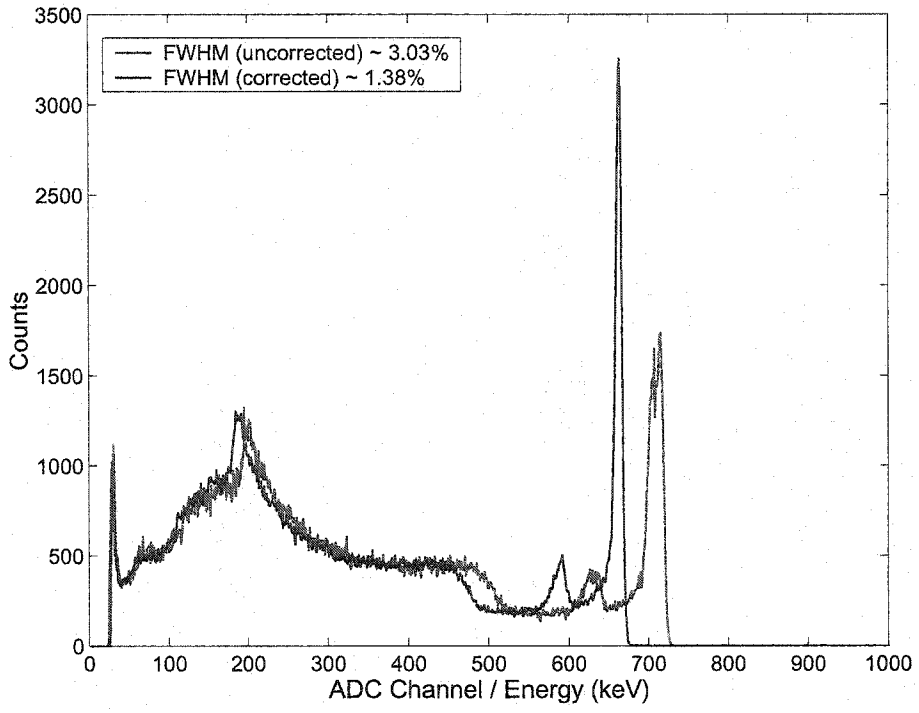

Figure 5.21: Cs-137 spectrum for pixel *No.*2 of detector 93203N91 using a shaping time of 8 μs on the anode and cathode. The depth corrected resolution was 1.38%.

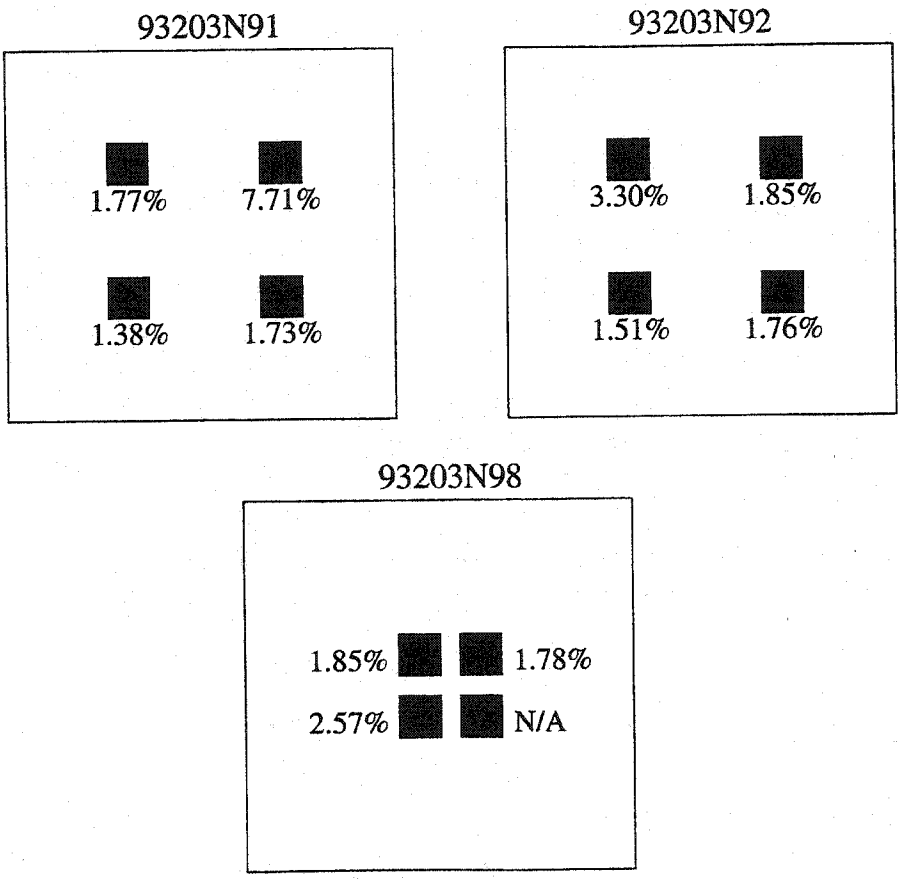

Figure 5.22: Depth corrected Cs-137 resolution for all three 10 mm thick detectors tested in this work. Eight of the eleven pixels with measurable signals had a resolution less than 2.0%.

peak (X-ray energy is approximately 35 keV) can be observed. In a few cases, it was possible to see the escape peak (Figure 5.23). The size of the photopeak is relatively small and can only be observed in depth index 20, corresponding to interactions adjacent to the cathode. Because of the low energy of the iodine X-ray, the X-ray will not travel far within the HgI_2 detector material. Therefore, the X-ray will be absorbed either within the pixel volume or within the gap region, where at least partial charge collection on the pixel can occur. Only if the X-ray escapes out the sides of the detector will an escape peak be observed. For an anode pixel, the escape peak can only be observed from the cathode side spectrum of the detector due to the low induced charge for events near the anode side of the detector (weighting potential and poor hole movement). Thus, only with depth sensing and observing only events that occurred next to the cathode will the iodine escape peak be observed. It should be noted that it would not be possible to observe the I escape peak if charge sharing between pixels and electron trapping is large in the detector, as these effects will lead to increased low-energy tailing of the photopeak. The I escape peak, whose itensity is very low, would then be combined with the low-energy tail of the photopeak.

5.4.2 Effect of Gap Size

Detector 93203N98 was unique in that the four anode pixels were placed adjacent to each other in the central region of the HgI_2 detector. This was considered an intermediary step while a fully pixelated HgI_2 detector was being developed. As was described earlier in Chapter 5, it was now possible to observe charge sharing events between pixels with some frequency. However, this detector suffered from a significantly larger gap between the pixel region and the surrounding large anode. The larger gap will lead to increased charge sharing between the anode electrodes and the effect on Cs-137 spectra can be seen in Figure 5.24. The figure shows a comparison between depth corrected spectra from two pixels, one with a normal narrow gap region (approximately 150 μm) and one with a large gap (500 μm) between the pixel and surrounding large anode. The energy resolution of the

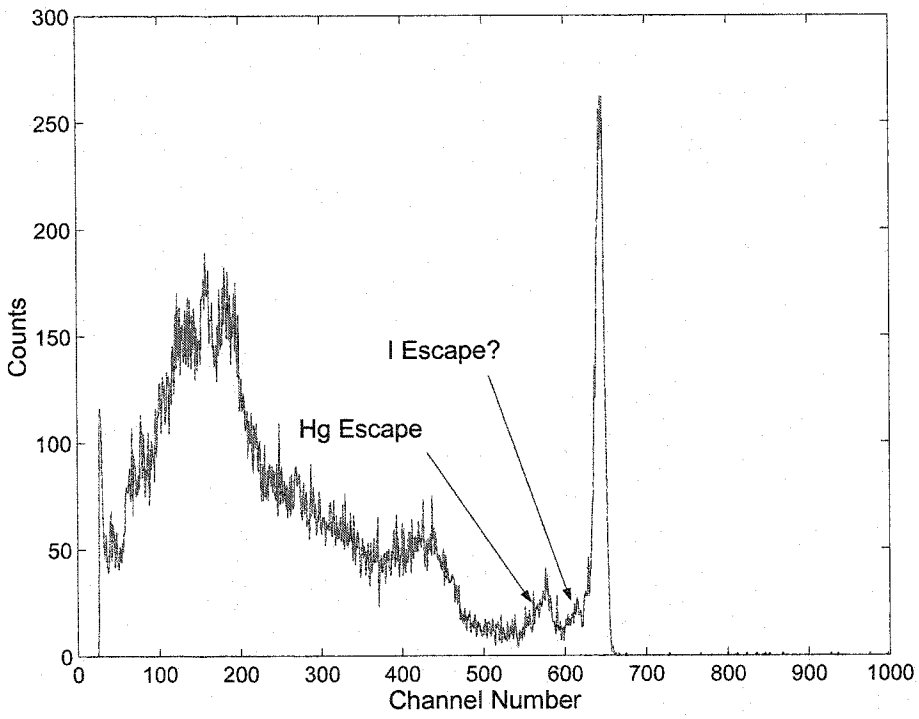

Figure 5.23: This Cs-137 spectrum is from detector 93203A98, pixel *No.*1, depth index 20 only, corresponding to events occurring near the cathode side of the detector. In this case, the iodine escape peak can be observed approximately 35 keV below the true photopeak.

pixel with the larger gap was slightly degraded due to larger charge sharing effects that increased the tailing on the lower energy side of the photopeak. There was also a significant increase in the total number of counts between the photopeak and Compton edge. This can be explained by increased charge sharing of a single photoelectric interaction due to the wide gap, and also from the possibility of increased multiple interaction events where an interaction takes place both in the pixel volume and the gap region. The increased gap region will weaken the ability to eliminate these multiple interaction events from the spectra. The increased events in the Compton region can be explained by the fact that the larger gap means a larger effective pixel volume, and therefore, a larger number of interactions (both photopeak and Compton) recorded by the pixel. These events will also suffer from significant charge sharing between the anode electrodes. Charge sharing will also significantly affect photopeak events that occur within the gap region. The small, yet very broad, peak at approximately 330 keV (a situation in which half the electrons are collected by the pixel and the remaining electrons are collected on the surrounding anodes) may have been caused by the increased charge sharing of true photopeak events within the larger gap region of detector 93203N98. Since it is vital to eliminate charge sharing events since they are not true multiple interaction events, the gap region needs to remain relatively small and consistent (same size on all sides of all pixels) in order to realize a fully pixelated HgI_2 detector.

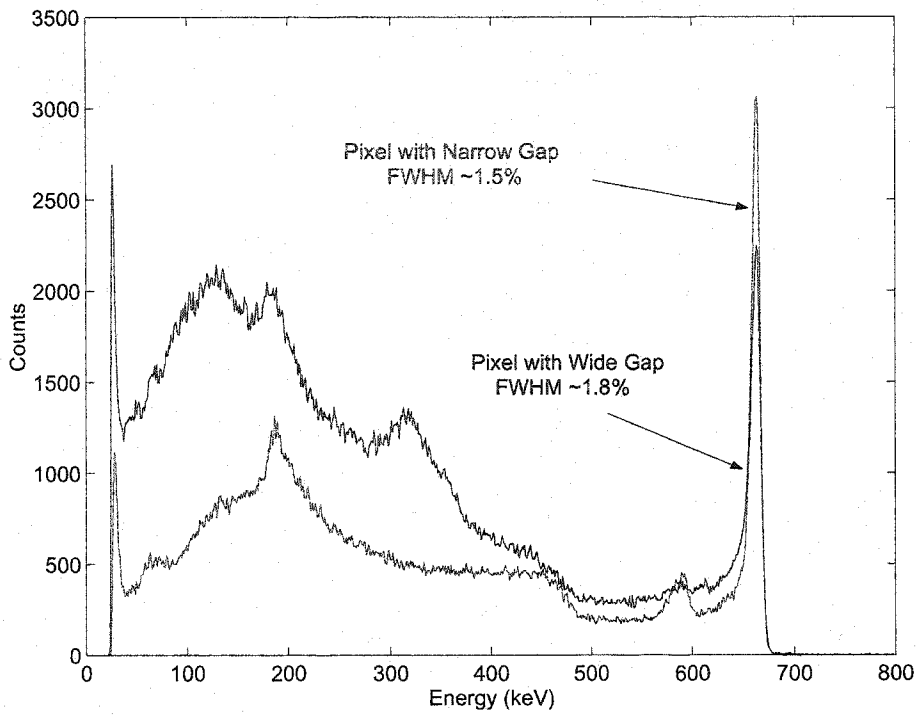

Figure 5.24: Comparison of two depth corrected Cs-137 spectra. The large gap shows a much larger Compton continuum, larger number of counts between the peak and Compton edge, and slightly more tailing on the low energy side of the 662 kev photopeak. These effects are due to the larger effective volume of the pixel and increased charge sharing between the pixel and the adjacent electrodes.

Chapter 6

Detector Crystal Performance

In addition to the spectroscopic experiments described in Chapter 5, other experiments to investigate detector performance were performed. In this chapter, these experiments are described and the results are discussed. The results from a multiple source spectra show that these HgI_2 detectors perform well for gamma-rays up to a few MeV in energy. The charge carrier properties are investigated and show that the mobilities and lifetimes of electrons and holes are on the same order as measured by others, but can vary from pixel to pixel in a single HgI_2 device. The polarization of HgI_2 is discussed and long term stability measurements show that current pixelated HgI_2 detectors do not seem to have the severe polarization problems that have plagued this material in the past.

6.1 Other Sources

6.1.1 Am-241

The 60-keV gamma-ray from Am-241 will interact only by the photoelectric effect and will not penetrate far into the detector (mean free path of approximately 0.29 mm). Thus, the Am-241 spectra consisted of mainly the single photopeak, as is shown in Figure 6.1. The resolution of the 60 keV photopeak was approximately 7.7% (approximately 4.6 keV). The spectrum as a function of depth index is shown in Figure 6.2. In this figure, the photopeak resolution for the depth indices of 18-20 were less than 6%. However, the resolutions of depths greater than 20 were worse, in some cases over 10%. These depths corresponded to a C/A ratio greater than 1, in which the effects of charge sharing and trapping would degrade the pixel signal. Thus, these depth spectra have worse resolution and the resolution of the

overall spectrum in Figure 6.1 was much worse than the associated 3.1 keV (5.2%) equilavent noise of the pixel. The Am-241 resolutions for the anode pixels generally ranged from 4-8 keV (7-12%) as some pixels showed more tailing on the low energy side of the photopeak, possibly due to charge sharing where some of the events had an interaction near the edge of the pixel region and subsequently lost some electrons to the gap region or the adjacent electrode. Another measurement was carried out by irradiating the anode side of the detector. Figure 6.3 shows a comparison of spectra between irradiation from opposite sides of the detector using the same electronics. Here, the spectra show that the induced charge from the anode irradiation was slightly lower than that for the cathode irradiation. The resolution of the photopeak from the anode irradiation was much worse than the cathode irradiation, with a value of 13.2%. Keeping in mind that the mean free path of the 60 keV gamma ray is about 0.3 mm, nearly all of the events will occur within the pitch region of the pixel when irradiation was performed from the anode side. Thus, the interactions occurred in the region where the weighting potential on the pixel has a severe slope. In order to induce the full charge on the pixel (a charge similar to the cathode irradaition case), some hole movement will be required. The fact that the photopeak centroid was only 8% lower for the anode irradiation suggests that there is some hole movement in the detector down the large slope of the weighting potential towards the cathode side. However, the poor hole movement and severe hole trapping, along with the severe depth dependence on the weighting potential, will degrade the energy resolution. However, this experiment with low energy gamma-rays proved that the entire thickness of the HgI_2 detector was active and contributed to gamma-ray spectra.

6.1.2 Multiple Line Gamma-Ray Spectra

While the single gamma-ray source spectra have shown remarkable energy resolutions using depth sensing and correction, it is far more important that the technique is applicable to spectra with multiple gamma-ray energies. A depth corrected spectrum from a collection of sources (Ba-133, Co-60, and Cs-137) is shown

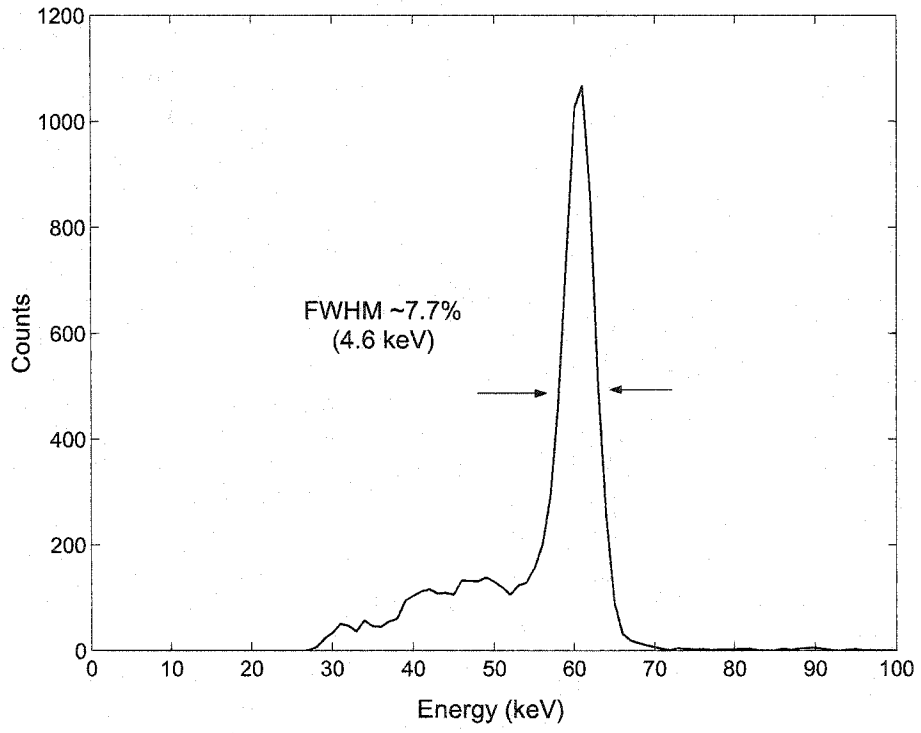

Figure 6.1: Am-241 spectrum for pixel *No.*3 of detector 93203N92 by irradiating the cathode side of the detector.

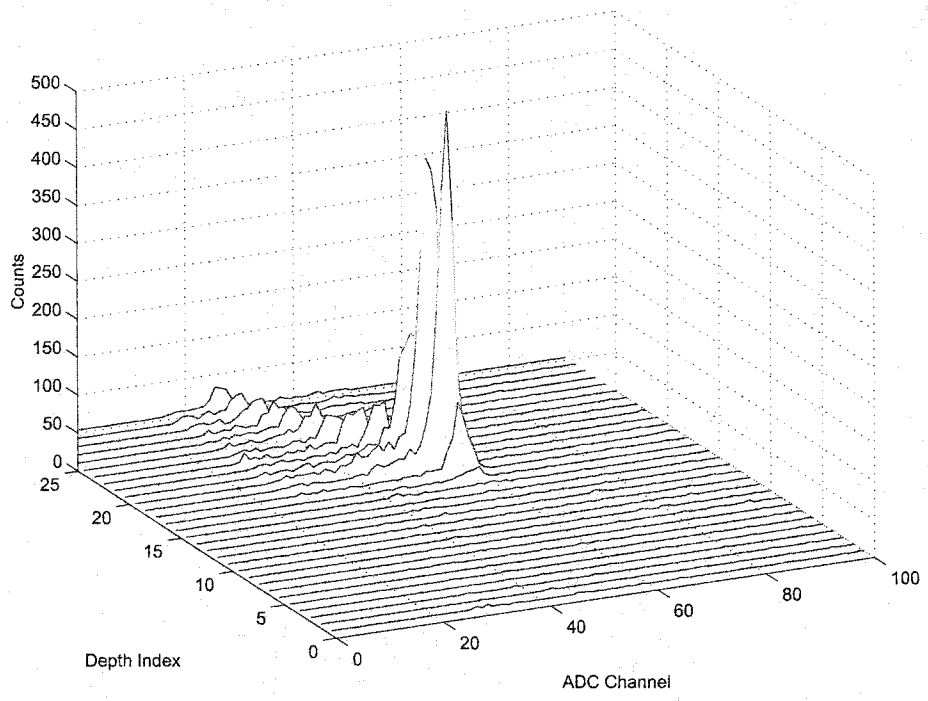

Figure 6.2: Depth spectra of the overall Am-241 spectrum shown in Figure 6.1. Most of the peak counts are contained within a a few depths. The resolution of the peaks in depths greater than 20 degraded due to charge sharing. This, in turn, degraded the resolution by increasing the low energy tailing of the spectra in Figure 6.1.

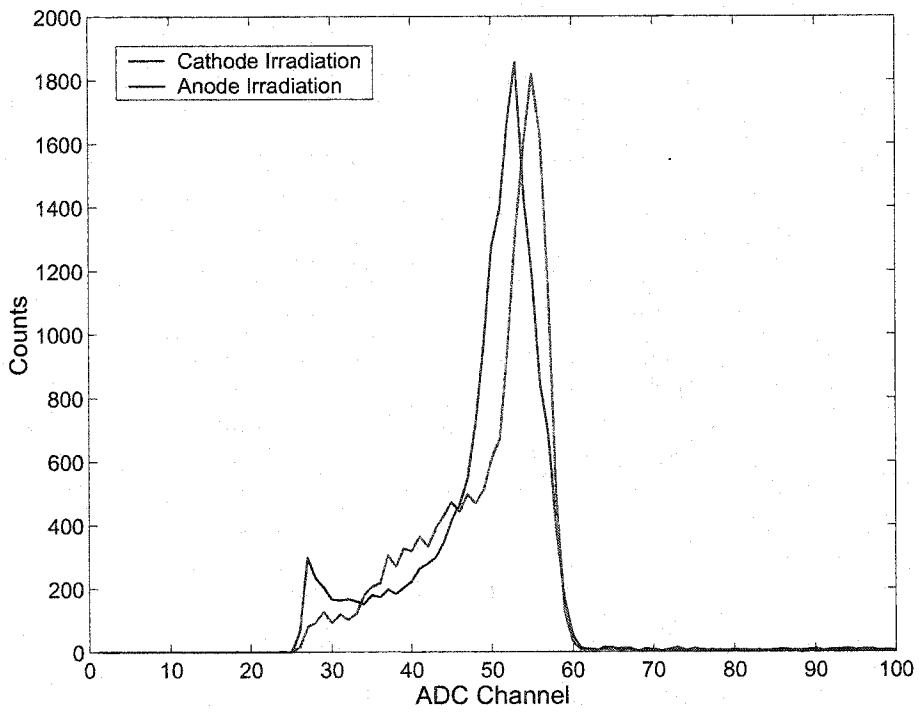

Figure 6.3: Am-241 spectra for pixel *No.*4 of detector 93203N92. In this figure, the comparison between the cathode side and anode side irradiations is shown.

in Figure 6.4. The five gamma-ray energies of Ba-133 and the Cs-137 peak can clearly be seen. However, the two photopeaks from Co-60 are difficult to observe due to the low activity of the source used in the experment (approximately 2 μCi) compared to the other sources (10 μCi). In addition, the reduced detection efficiency for high energy gamma-rays, and the fact that high energy gamma-rays will more likely interact via Compton scattering, also reduced the photopeak for the Co-60 source (the spectrum was generated for single pixel events). In this case, three sources (Ba-133, Cs-137, and Co-60) were placed under the cathode and a 1 day spectrum was collected for detector 93203N98, pixel *No.*4. The resolutions of the 1332 keV and 1173 keV gamma-rays from Co-60 were approximately 1.7% and 1.8%, respectively. The low energy gamma-ray (83 keV) of the Ba-133 source should have been larger, as shown by the measured spectrum of only the barium source (Figure 6.5). In order to more clearly observe the Co-60 photopeaks, the Ba-133 source was moved off axis from the detector. The low energy gamma-ray was absorbed by the surrounding HgI_2 material (these events would be detected by the large surrounding anode) prior to the volume of the detector corresponding to the pixel region. Figure 6.5 shows that the 83 keV photopeak was as strong as expected when the source was placed directly under the cathode.

One advantage of depth sensing with the pixelated detectors is that spectra can be separated by depth, and one can observe how gamma-rays with different energies interact with HgI_2. Figure 6.6 shows the spectra from Figure 6.4 separated according to depth index. The 83 keV gamma-ray from Ba-133 can only be observed in depths near the cathode side of the detector, while the higher energy gamma-rays can be observed throughout all depth spectra. It is possible to use the fact that low energy gamma-rays will only interact in a small volume of the detector to choose the location to collect and analyze spectra. This is possible because depth sensing with pixelated detectors can break a large volume detector into many hundreds (or thousands) virtual detectors.

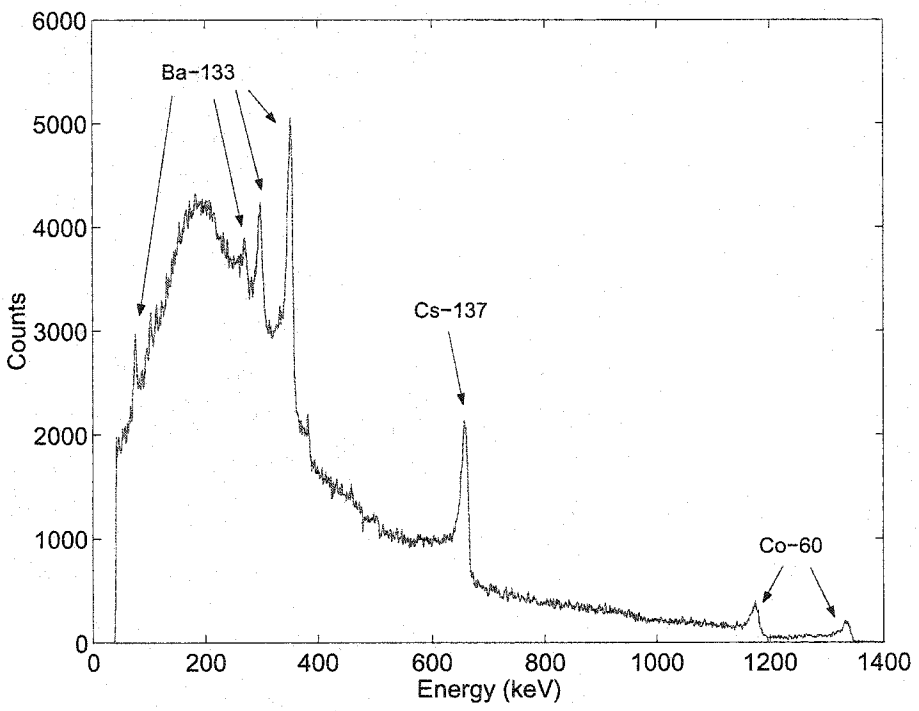

Figure 6.4: Depth corrected, multiple source spectrum for detector 93203N98, pixel *No.*2, using a bias of 2500 V and a shaping time of 8 μs.

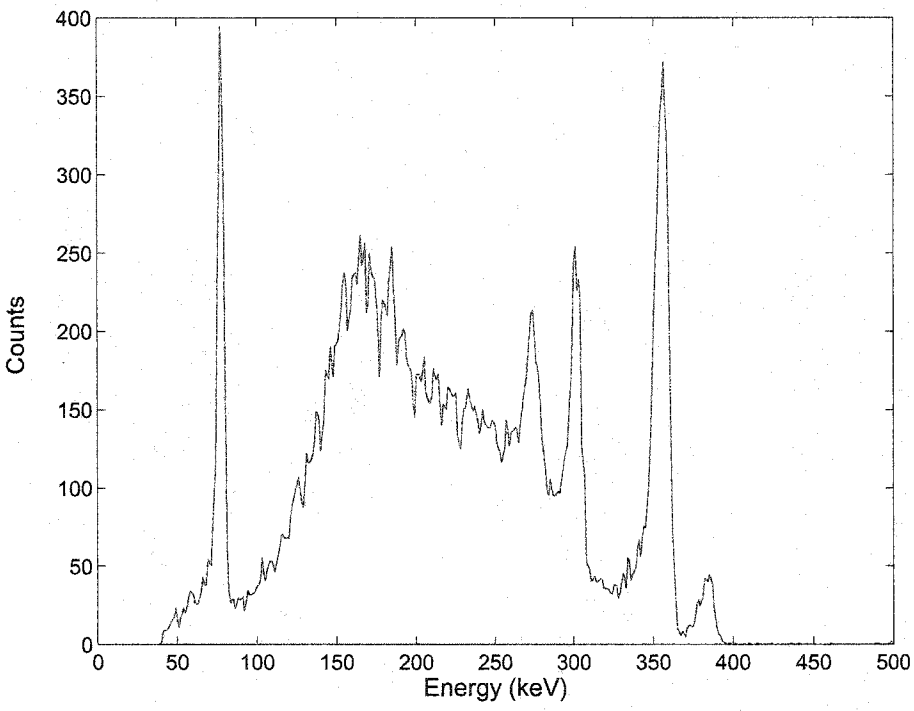

Figure 6.5: Ba-133 spectrum from detector 93203N98, pixel *No.*2. In this case the source was placed directly under the cathode.

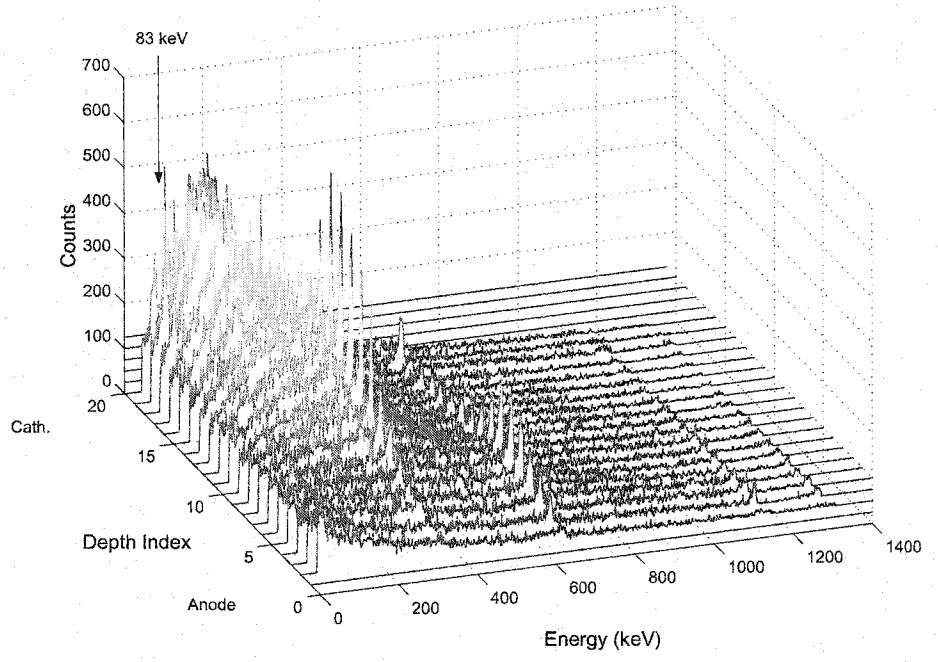

Figure 6.6: Multiple source spectrum from Figure 6.4, separated into many spectra as a function of depth index. Since the sources were placed under the cathode side of the detector, the low energy gamma-rays (such as the 83 keV gamma-ray from Ba-133) will only observed in depth spectra near the cathode.

6.2 Properties of Charge Carriers

6.2.1 Measuring Electron Mobility

The electron mobility (μ_e) was measured by determining the rise time for a near cathode event. Thus, the electron drift time ($t_{drift,e}$) was measured across the full thickness of the detector. Figure 6.7 shows a near cathode event from a 1 cm thick HgI_2 detector. Knowing the thickness of the detector (D) and the voltage applied to the cathode, the electron mobility was calculated to be

$$\mu_e = \frac{D^2}{V t_{drift,e}} = \frac{(1.05cm)^2}{2500V \times 7.1\mu s} = 62 \pm 2\frac{cm^2}{Vs}. \quad (6.1)$$

The error in the above calcuation was due to the accuracy of the rise time measurement. The jitter of the signal in Figure 6.7 gave an upper and lower bound for the rise time measurement. The μ_e for several detectors were measured and the values ranged from 35-80 cm^2/Vs. The values measured were approximately the same as some previous results using a 4.3 mm thick detector [92]. Similar measurements were performed using the 5 mm thick detectors in this work. For the thinner HgI_2 detectors, the μ_e was calculated to be in the range of 48-70 cm^2/Vs. Therefore, detector thickness had no effect on the mobility measurements.

6.2.2 Measuring Hole Mobility

The hole mobility (μ_h) was estimated in a similar manner. In order to observe a signal that contains a significant amount of hole movement, an interaction that occurred next of the anode was selected. Since holes will not travel far in HgI_2, the cathode signal could not be used to determine μ_h since the signal from the cathode would be too small. However, if holes move away from a pixel for an event near the anode, a significant signal will be induced since the weighting potential has a sharp slope near the pixel. An example signal where the signal on the pixel is mainly due to hole movement is shown in Figure 6.8. The lack of a large pulse on the cathode indicates that the interaction took place near the anode. The pulse on the anode pixel is due to the movement of holes away from the pixel in the region

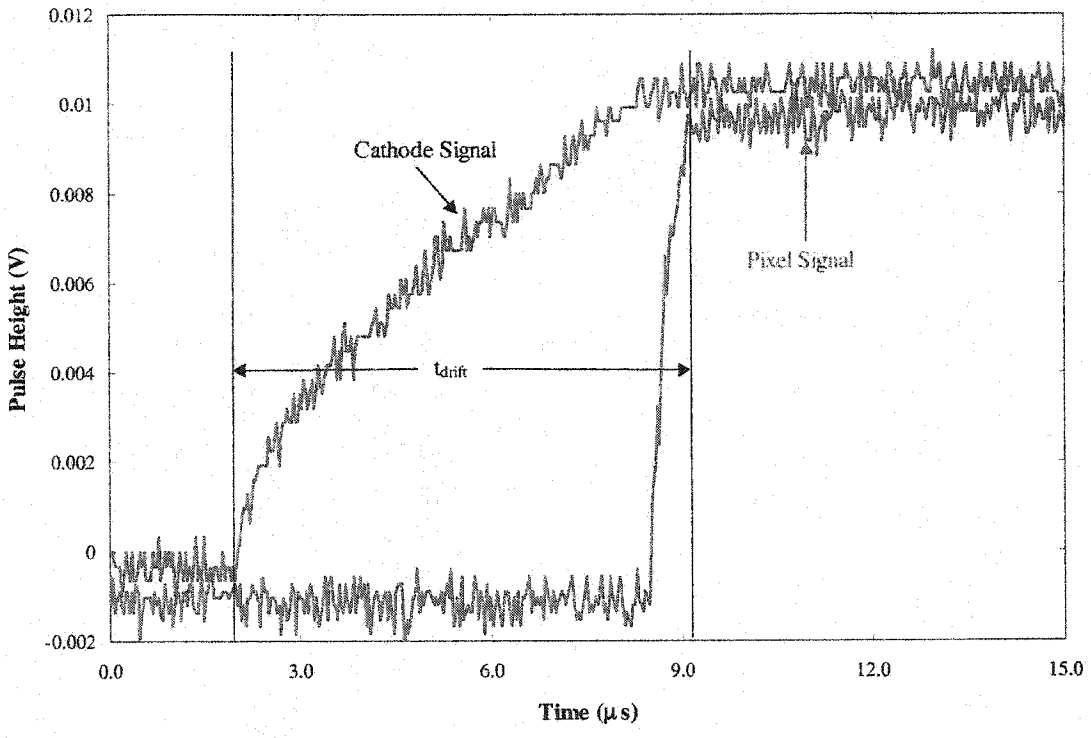

Figure 6.7: Measuring the drift time of electrons for a near cathode event can estimate the electron mobility. The HgI_2 detector used in this case was 93203N91 with a cathode bias of -2500V.

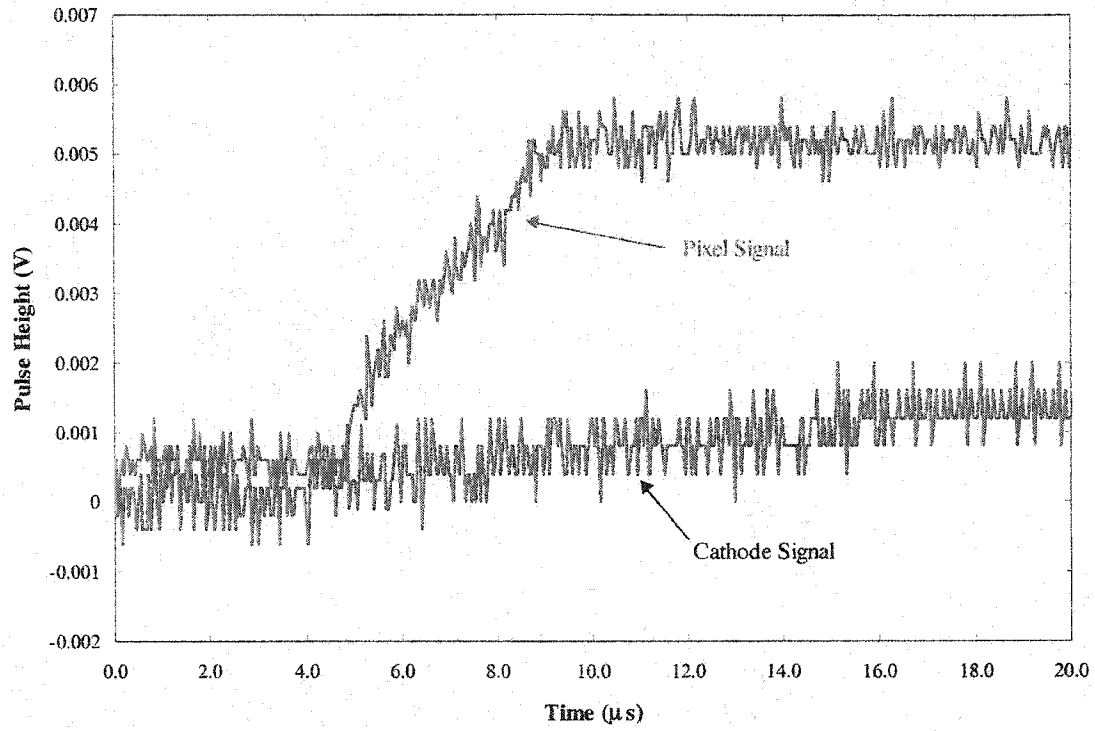

Figure 6.8: Cs-137 signal for an event directly under the anode pixel for 93203N91. The lack of a cathode signal along with a slow rise of the anode pixel signal indicates that this signal was from the movement of holes away from the anode but within the pitch depth of the pixel.

where the weighting potential has a severe depth dependence.

In order to calculate hole mobility, the pitch for the pixel must be estimated. This can be estimated by comparing the rise time of the cathode signal with the rise time of the sharp signal increase for the anode pixel for a near cathode event. Therefore, the pitch depth (d_{pitch}) was estimated to be (using Figure 6.7):

$$d_{pitch} = \frac{t_{pixel}}{t_{cathode}} \times D = \frac{0.63}{7.1} \times 10.5mm = 0.93 \pm 0.03mm \tag{6.2}$$

In this case, the error was due to the jitter associated with both rise times. Using this pitch depth and the measured drift time of 5.0 ± 0.2 μs for holes, the μ_h was estimated:

$$\mu_h = \frac{d_{pitch}}{\vec{E}t_{drift,h}} = \frac{(0.093cm)}{2500V/cm \times 5.0\mu s} = 7.4 \pm 0.4 \frac{cm^2}{Vs}. \quad (6.3)$$

Based upon an electric field of 2500 V/cm, we estimated μ_h to be approximately 7.4 cm^2/V-s. This calculation assumed that the holes travel the entire pitch depth, and provided a maximum possible value for hole mobility. In reality, holes will be severely trapped in the detector before moving the entire pitch depth. If the event in Figure 6.8 is assumed to be a photoelectric event, the average distance that the holes moved d_h can be determined by the ratio of the signals between the cathode-side and anode-side interactions.

$$d_h = \frac{4.8mV}{10.6mV} \times 0.93mm = 0.42 \pm 0.04mm \quad (6.4)$$

Using this value, the hole mobility was calculated to be

$$\mu_h = \frac{(0.042cm)}{2500V/cm \times 5.0\mu s} = 3.4 \pm 0.4 \frac{cm^2}{Vs}. \quad (6.5)$$

This value is similar to the generally accepted value for μ_h of about 4 cm^2/V-s for HgI_2. The hole mobility was measured for several pixels and a mean value of 3.2 ± 0.3 cm^2/V-s was obtained.

6.2.3 Estimation of the Mu-Tau Product for Electrons

The mu-tau product for electrons, $(\mu\tau)_e$, was calculated previously using the method described in Section 2.3.2. By varying the detector bias, the amount of trapping will vary due to changes in the magnitude of the electric field within the detector. This will show up in spectra as a shift in the photopeak amplitude (see Figure 6.9) due to a change in the number of trapped electrons. This shift in photopeak amplitude for near cathode events was then used to estimate $(\mu\tau)_e$.

Two different sources were used in the measurements (one high and one low energy gamma-ray) to determine the electron mobility-lifetime product. In the first measurement, $(\mu\tau)_e$ was calculated using a Cs-137 source. The depth index that had the highest number of peak counts was considered the cathode side, since

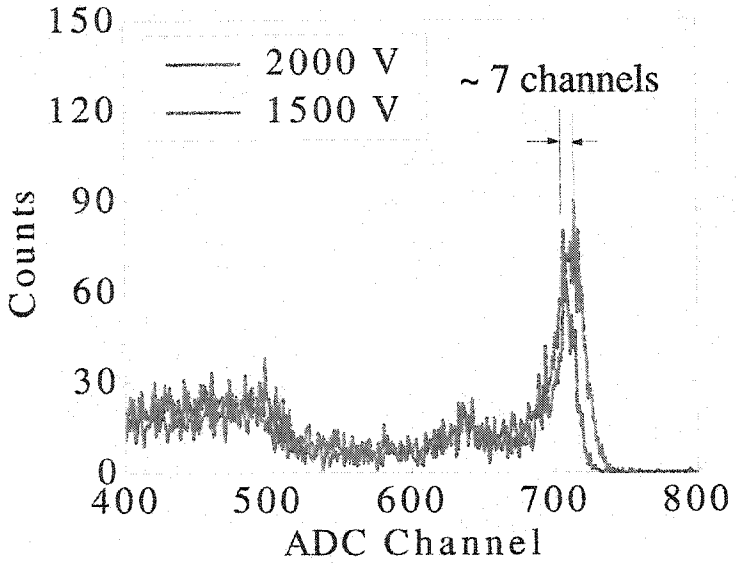

Figure 6.9: Cs-137 photopeak spectra obtained from detector 92512Q92, pixel *No.2*, depth index 20, for two detector voltages. The shift in the photopeak position was used to measure $(\mu\tau)_e$.

the detector was irradiated from the cathode side. For example, the shift in the photopeak in Figure 6.9 was approximately 7 channels. Therefore, the $(\mu\tau)_e$ was estimated to be:

$$(\mu\tau)_e = \frac{5.65^2}{ln(701/708)}(1/2000 - 1/1500) = (5.0 \pm 0.3) \times 10^{-3} cm^2/V \qquad (6.6)$$

The error of this calculation is mostly dependent on the ability to measure the drift distance, which was limited to approximately 5% because the detector was divided into 20 depths. The estimated values for $(\mu\tau)_e$ using this method are shown in Table 6.1, along with the measured depth corrected energy resolutions for each pixel. The $(\mu\tau)_e$ estimation varied by factor of five in magnitude, from 1.3×10^{-3} cm^2/V to 7.0×10^{-3} cm^2/V. It is interesting to note that the pixels that had the higher mu-tau product also had better energy resolution. Thus, a correlation between electron transport properties and energy resolution can clearly be seen for this detector.

A low energy source was used to irradiate the detector from the cathode side,

Table 6.1: $(\mu\tau)_e$ Estimations and Measured Depth Corrected Resolutions for Pixels on Detector 92512Q92

Parameter	Pixel 1	Pixel 2	Pixel 3	Pixel 4
$(\mu\tau)_e$ (cm^2/V)	1.3×10^{-3}	7.0×10^{-3}	4.8×10^{-3}	3.5×10^{-3}
Resolution	4.18%	2.05%	2.58%	2.9%

this case Am-241. With a mean free path of about 300 microns, the 59.5 keV γ-rays emitted by Am-241 are absorbed within 0.7 mm of HgI_2. Thus, most of the events in the overall spectra should also be contained in a depth index corresponding to the cathode side. This is the case as most photopeak events are contained within 3-4 depth indices (Figure 6.10) corresponding to approximately 1 mm thick of the HgI_2 detector. Performing the same calculation procedure as the Cs-137 source, the estimated $(\mu\tau)_e$ ranged from 0.9-3.1 x 10^{-3} cm^2/V for the pixels. The fact that the values for $(\mu\tau)_e$ obtained using either high or low energy gamma-rays were on the same order of magnitude was encouraging and showed that the $(\mu\tau)_e$ can be estimated using high energy gamma-rays when operating pixelated HgI_2 detectors at room temperature.

It should be noted that a potential source of significant error in these calculations is the fact an increase in detector bias can increase the thickness that corresponds to near cathode interactions. The increase is due to the fact that the holes produced in the interaction will travel further at higher biases, increasing the C/A signal ratio. Therefore the thickness of the depth index for near cathode events will increase. This increase in thickness will cause errors in the calculation since the thickness of the depth index is different for the two voltages. This effect must be eventually accounted for and corrected to increase the accuracy of the calculation for $(\mu\tau)_e$. Also, attempts to measure $(\mu\tau)_e$ for the 1 cm thick HgI_2 detectors were not successful because the detectors could not be biased beyond 2800 V without suffering from significant noise and breakdown. Biasing the detector at lower voltages was also considered, however proper depth sensing would not be possible because the electron drift time at lower voltages would have been longer than the amplifier shaping times.

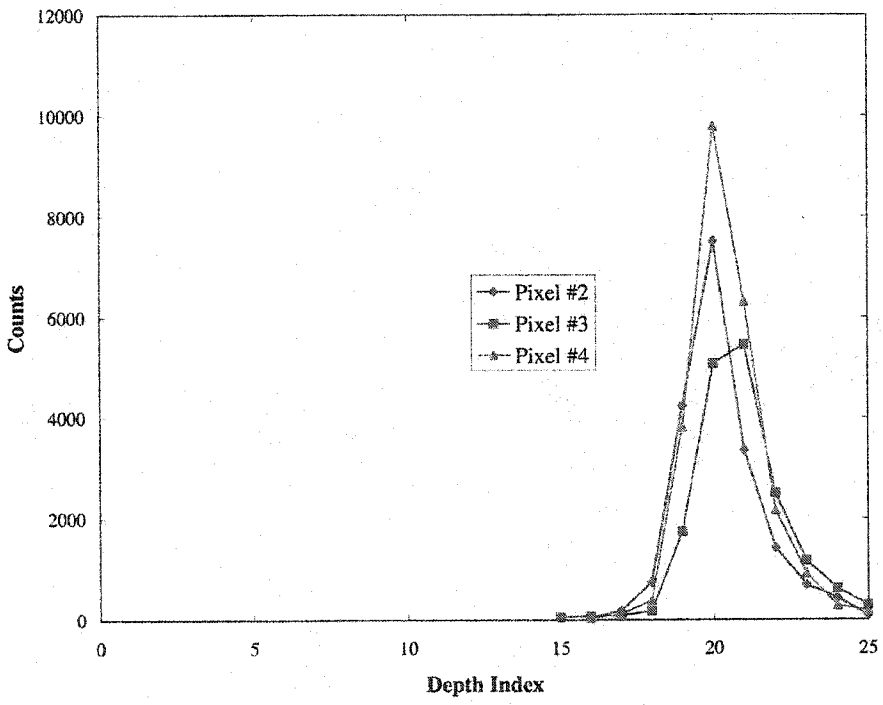

Figure 6.10: The low gamma-ray energy of Am-241 can also be used to determine $(\mu\tau)_e$ using the fact that nearly all of the interactions will occur within 1 mm from the cathode side of the detector.

6.2.4 Estimation of the Mu-Tau Product for Holes

The mu-tau product for holes was determined by comparing the photopeak from Am-241 60 keV gamma-rays when the detector (93203N92) was irradiated from opposite sides and using a planar cathode (Figure 6.11).The cathode irradiation spectra appeared at a much higher ADC channel since electrons can travel virtually the full thickness of the detector. The peak area for the cathode irradiation was channels 50-70, and 2-9 for the anode irradiation. Note that channel 1 was omitted in the anode irradiation case since it had a large number of counts due to noise. Calculating the peak centroids of the peak areas, the ratio between the peaks was determined to be:

$$r = Q_A/Q_C = \frac{5.21}{60.7} = 0.086 \pm 0.001 \tag{6.7}$$

Error propagation analysis of this equation revealed an error of about 1%. Assuming a $(\mu\tau)_e$ of $(5.0 \pm 0.3) \times 10^{-3}$ cm^2/V, a $(\mu\tau)_h$ value of $(3 \pm 0.4) \times 10^{-5}$ cm^2/V was obtained by solving Equation 2.30. The anode irradiation spectrum showed a high energy tailing effect and may have increased the $(\mu\tau)_h$ estimation.

6.2.5 Summary of Charge Carrier Properties

Table 6.2 summarizes the results of the estimation of $(\mu\tau)_e$, $(\mu\tau)_h$, τ_e, and τ_h for the HgI_2 pixelated detectors currently being developed as potential room temperature gamma-ray spectrometers. Table 6.3 summarizes the calculation of drift times for electrons and holes in HgI_2 at three separate biases while ignoring charge trapping. From these results, it is clear that it would be advantageous to be able to develop detectors that can generate spectra using only electron collection for signal generation as shorter collection times could be used and the significant hole trapping problem can be ignored. Considering the lifetime for holes, even with a detector bias of 10 kV on a 1 cm thick device, (electric field of 1000 V/mm), the holes will effectively travel only about 3 mm before being trapped.

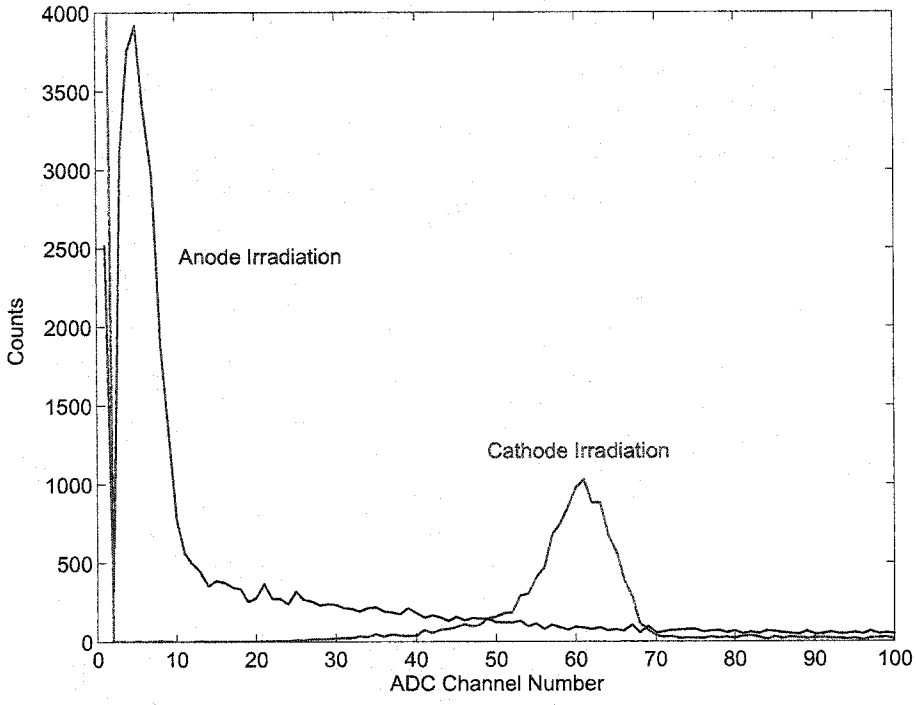

Figure 6.11: Am-241 spectra from reading out the cathode signal for both a cathode-side and anode-side irradiation of detector 93203N92.

Table 6.2: Typical Calculated Electron and Hole Transportation Characteristics for Pixelated HgI_2 Detectors

μ_e (cm^2/V-s)	τ_e (μs)	μ_h (cm^2/V-s)	τ_h (μs)
62	80	3.4	8.6

Table 6.3: Drift Times (in μs) for Electrons and Holes for a 1 cm Thick HgI_2 Detector at Different Applied Biases

Charge Carrier	2500 V	5000 V	7500 V	10000 V
Electrons	6.45	3.23	2.15	1.61
Holes	117	58.8	39.2	29.4

6.3 Long-Term Stability and Polarization of Pixelated HgI_2

Of critical importance to the ability of pixelated HgI_2 detectors to perform in realistic applications is the ability of the detector to operate over time without a significant change in detector response. In the past, conventional planar HgI_2 detectors have shown the debilitating effects of polarization [9] [30]. Thus, it was important to observe the performance of a pixelated HgI_2 over several months of constant operation and irradiation while maintaining a constant temperature of 23 ± 1 °C. Two main time periods were observed: the immediate polarization of a HgI_2 pixel within the first several days after biasing a new detector, and the long-term stability of several pixels on the same detector over the course of several months.

6.3.1 Polarization of HgI_2 Within First Few Days After Applying Bias to the Detector

An eight hour Cs-137 spectrum was collected from detector 93203N98, pixel *No.*2 immediately after applying a cathode bias of -2500 V. As seen in Figure 6.12, the initial depth corrected spectrum had a resolution of approximately 2.7% at 622 keV. The resolution was worse than expected, due to the presence of a large gap between the pixel and the large surrounding anode that will contribute an increase in charge sharing and trapping between the two electrodes, as explained in Section 5.4.2.

In addition to the depth corrected spectra shown above, depth and time dependent data was collected from the pixel. The photopeak position as a function of depth index and time after biasing is shown in Figure 6.13. The peak position decreases slightly with time (approximately 1-2%) across all depths of the detector, but decreases slightly more near the cathode side of the detector (13 channels versus 8 channels for events closer to the anode). A slight shift in the photopeak position can be seen in Figure 6.14, which shows three uncorrected Cs-137 spectra at different times after application of detector bias. There is a slight shift between hours 8 and 80, but the photopeaks 80 hours and 160 hours after biasing the detector appear to be nearly identical. After the first 2-3 days after biasing the detector,

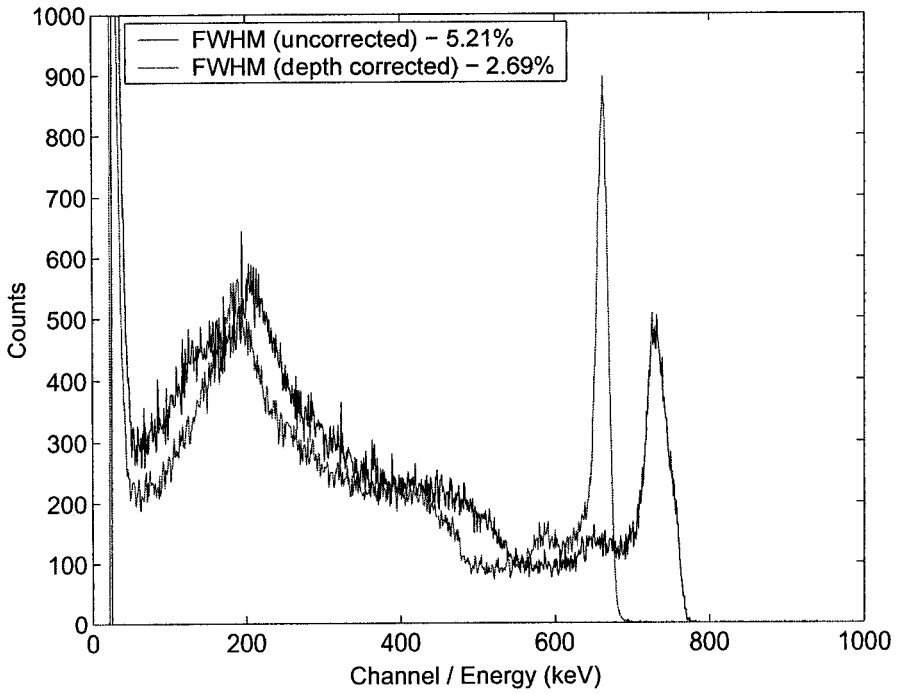

Figure 6.12: Cs-137 spectrum for first 8 hours after biasing the detector to -2500 V. The shaping time used in the long-term stability measurements was 8 μs. Depth correction improved the resolution of the photopeak from 5.3% to 2.7%.

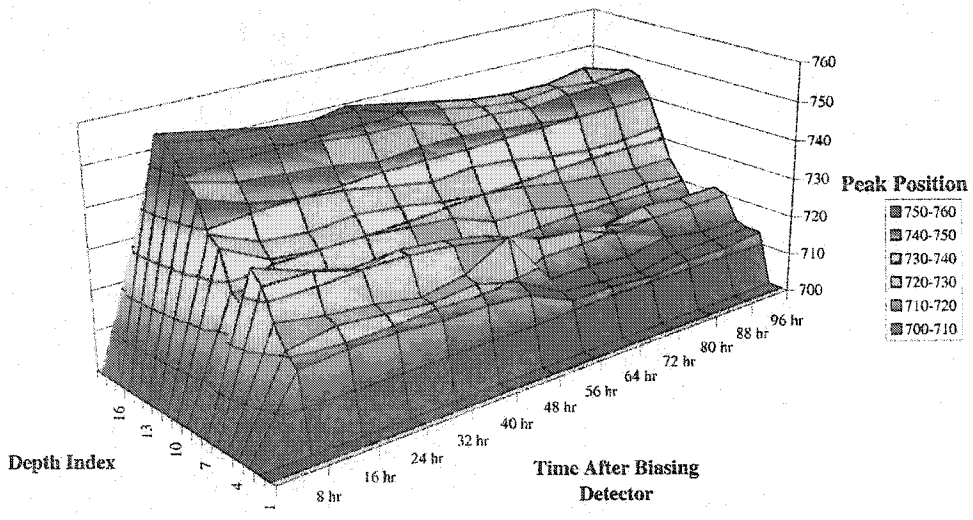

Figure 6.13: Photopeak position as a function of both depth index and time after biasing the detector. There is a slightly larger decrease in the photopeak position for events near the cathode as opposed to near anode events.

the spectra appears to be stable and repeatable for many days afterwards.

The resolution as a function of depth and time remains relatively consistent (Figure 6.15). However, one measurement (56 hours after biasing) showed a worse resolution and may have been due to increased noise during that time. The figure also shows a much worse resolution for photopeak events that had a large C/A ratio. When more electron trapping or charge sharing occurs, the anode signal is reduced which increases the C/A ratio. This suggests that the effects of charge trapping and charge sharing between anodes degraded the resolution as was expected due to the large gap associated with detector 93203N98.

The photopeak count rate as a function of depth and time, as seen in Figure 6.16, was relatively constant during the first 4 days, suggesting that the effective volume of the pixel remained constant. The peak count rate as a function of depth for any given day was different than expected. The source was placed under the cathode side of the detector, and therefore the largest count rate should have appeared at larger depth indices (Depth Index 17 or 18). In this case, the largest count rate appeared in the index closer to the anode side of the detector. In addition, there is

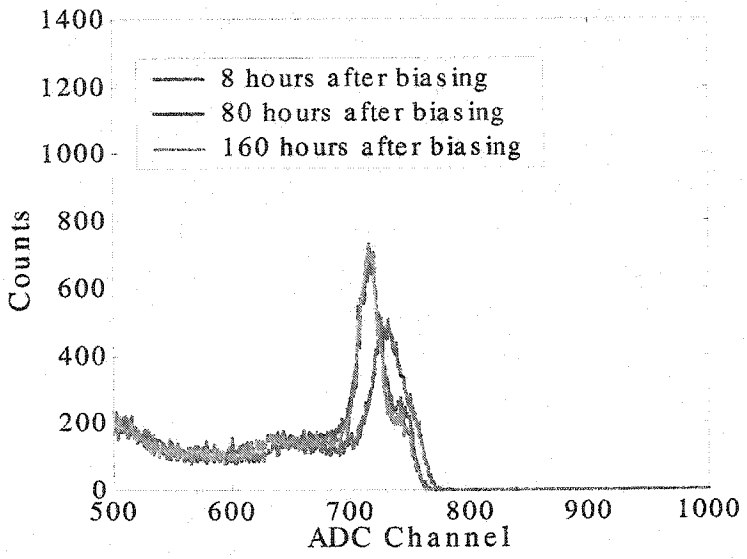

Figure 6.14: Cs-137 pixel anode spectra (magnified to show the photopeak) at three different time periods after biasing the HgI_2 detector. Each measurement was eight hours in duration.

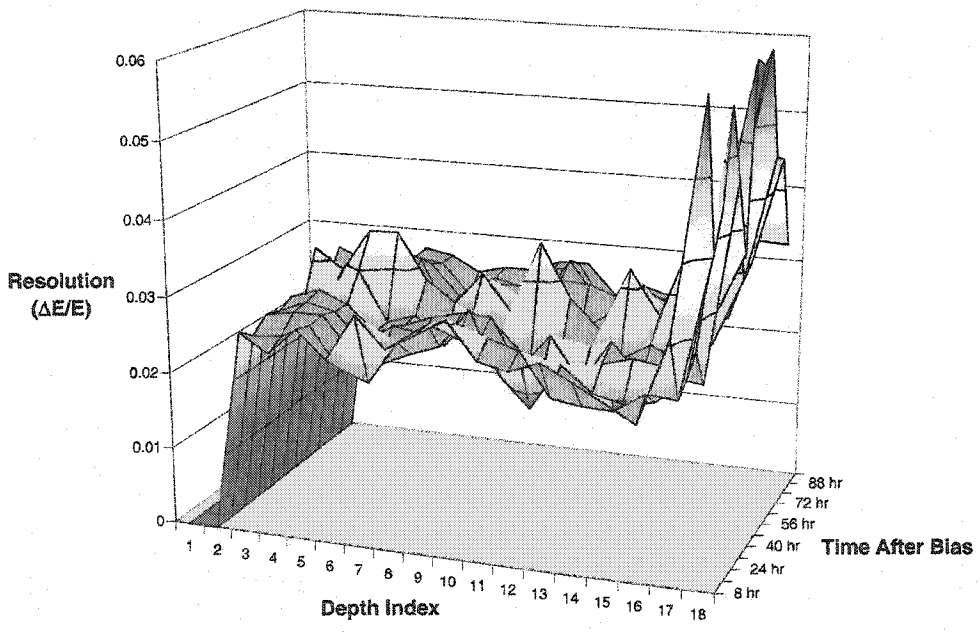

Figure 6.15: Cs-137 photopeak resolution as a function of both the depth index (depth of interaction) and time after biasing the detector.

a large peak count rate at depth index 8. This suggests that the effective volume of the near anode depth indices was much larger than the volume for those closer to the cathode. This phenomenom may have been caused by the large gap. An electron cloud generated near the anode will not diffuse as much as a cloud generated near the cathode due to the distance it must travel to be collected by the pixel. Thus, interactions near (or in) the gap region that occur closer to the anode side of the detector have a better chance of being collected without the effects of charge sharing and charge loss, and the measured peak count rate will be higher near the anode. The higher peak count rate at depth index 8 may have been caused by material defects that caused the weighting potentials to have a non-linear effect in this region of the pixel volume. Thus a larger volume of the pixel region produced a C/A signal ratio around 0.45 than was expected for a perfect linear weighting potential. The results from the first four days of measurements showed that the peak information remained relatively consistent and suggest that polarization only occurred during the first few days after biasing the detector and was not as severe as the results previously presented by others using planar electrodes. However, the previous works concerning polarization of HgI_2 were performed more than 10 years ago, and improvements in the growth of HgI_2 material used in the construction of these pixelated detectors may have contributed in the reduction of polarization effects.

6.3.2 Long-Term Stability of Pixelated HgI_2 Gamma-Ray Spectrometers

In addition to collecting spectra over the first week, spectra were obtained over a several month period in order to observe any long term changes in the response to gamma-rays and the associated spectra obtained from pixelated HgI_2 detectors. After 25 days of measuring only pixel $No.2$, alternating measurements including pixels $No.1$ and $No.4$ were included in the measurements to observe any long term polarization effects on the other working pixels (pixel $No.3$ was grounded directly to the detector box). Figure 6.17 shows the overall photopeak position as a function of time after biasing. The overall peak position on all three pixels remained

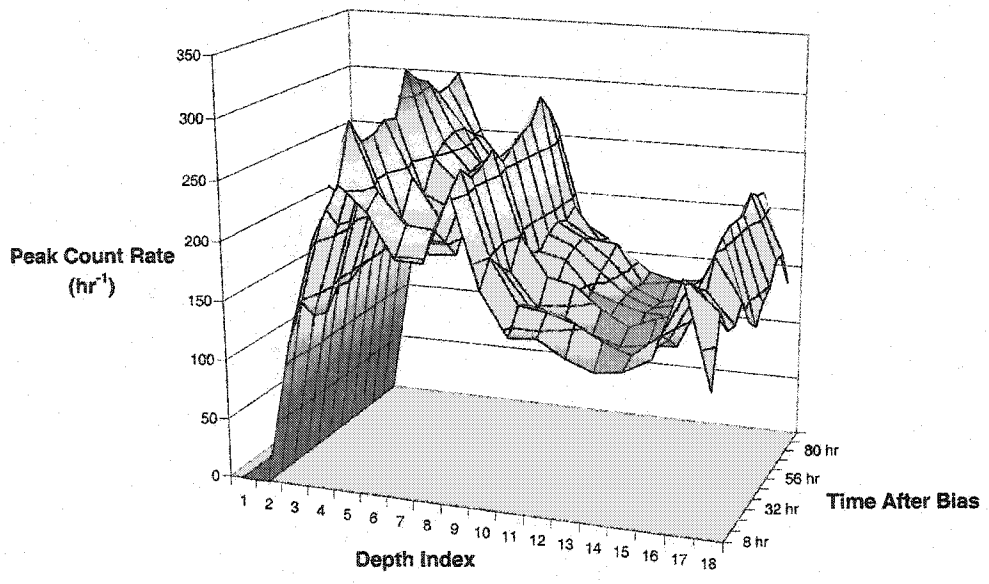

Figure 6.16: Cs-137 photopeak count rate as a function of depth and time after applying the detector bias.

relatively constant over the nearly 4 months of operation. Aside from the decrease on pixel *No.*2 during the first few days of operation, the peak position on all three pixels only varied by no more than 10 channels on any pixel, or about 1.5% over the course of the measurement period. Should a fully pixelated HgI_2 detector be applied in a realistic case, a gradual decrease of this magnitude can be accounted for during a calibration step prior to making the actual measurement.

The depth corrected resolution (Figure 6.18) also remained consistent over the course of operation. Pixel *No.*2's resolution remained near 2.8%, while the other two pixels had depth corrected resolution near 2%, with pixel *No.*4 average about 1.9% FWHM. The photopeak count rate of pixel *No.*4 showed a significant decrease over time of about 35%, as can be seen in Figure 6.19. The results suggest that pixel *No.*4's effective volume is decreasing, while the other two pixels remain constant. The large gap surrounding the pixel may have contributed to the decrease in effective volume if an accumulation of space charge caused a decrease in the electric field in the gap region. This could cause the effective volume of the pixel to decrease. This decrease was not observed on the other two pixels despite

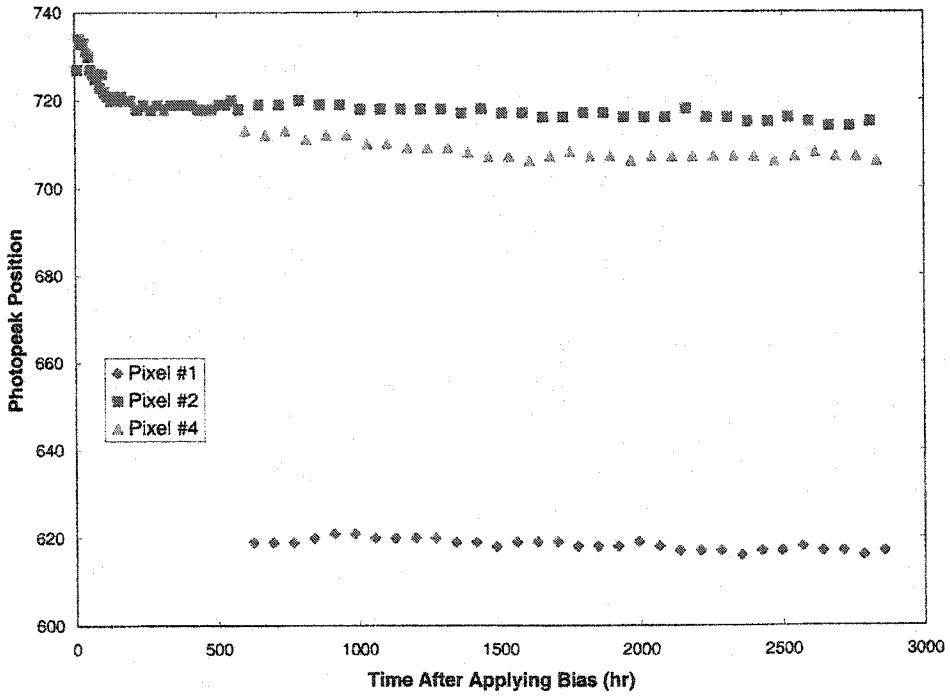

Figure 6.17: The peak position for the three working pixels does not vary much after the first few days once the bias is applied.

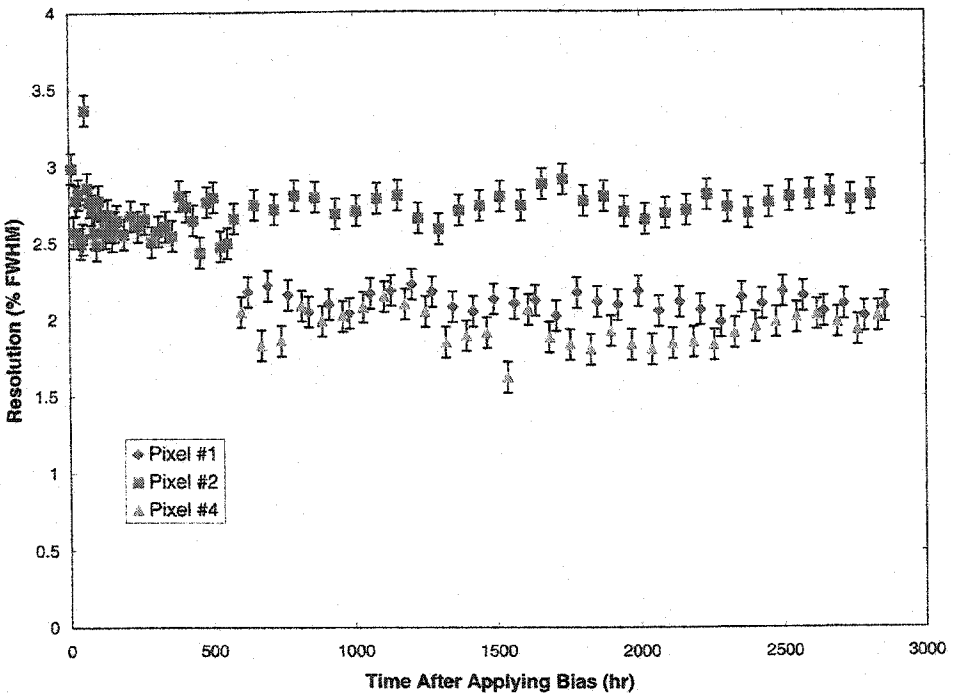

Figure 6.18: The depth corrected resolution remained relatively consistent for all three pixels over the course of the study.

the fact that all three pixels suffered from a large surrounding gap. In order to make a better assessment of polarization of a realistic device, fully pixelated HgI_2 detectors will also need to be tested for polarization effects. The measurements shown here suggest that current HgI_2 material can operate over a long period of time with constant peak position and stable resolution.

6.3.3 Testing a Possible Polarization Model

One advantage of the pixelated HgI_2 detectors is that models for trapping and charge transport can be tested and evaluated and variations on charge transport properties can be measured. Polarization models can also be tested for their validity. One model suggests that Auger recombination, whereby the trapped hole can release an electron into the conduction band, was the cause for polarization [30]. This model was tested using the HgI_2 detector 93203N98. The Auger recombina-

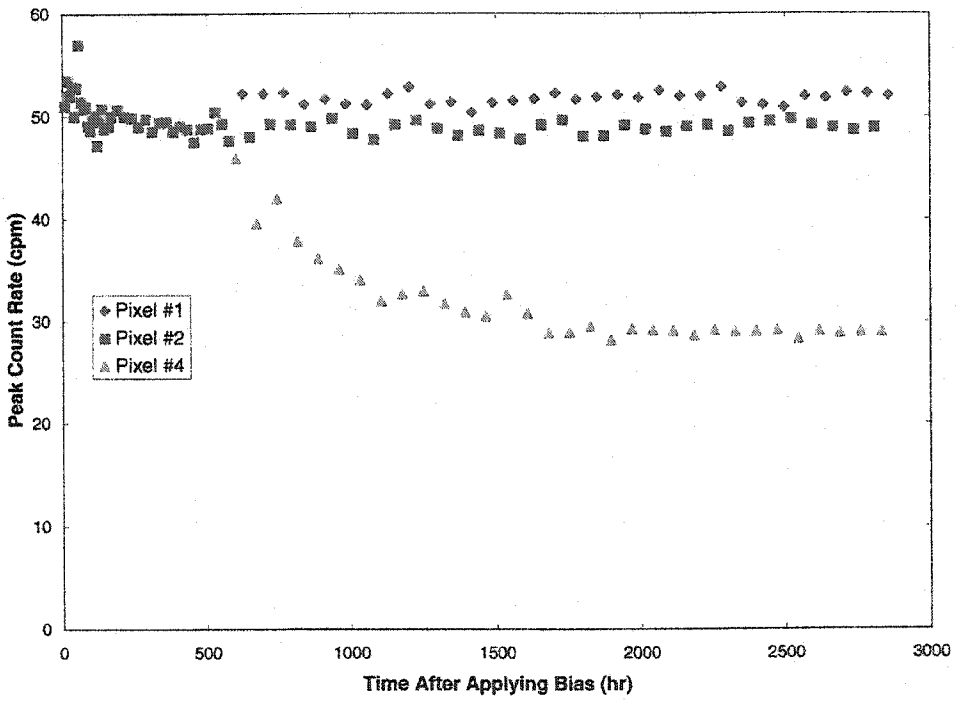

Figure 6.19: While the peak count rate remains relatively constant for pixels *No.*1 and *No.*2, pixel *No.*4 shows a decreasing count rate with time.

tion process can result in two electrons being collected for each electron-hole pair created in an interaction event, and the amount of recombination should decrease over time. Since the signal generated on an anode pixel is mainly determined by the number of electrons collected on the pixel, the induced charge on the pixel can be significantly affected by the amount of Auger recombination in the detector assuming the the timing of the release of the Auger electron is within the charge collection time. Figure 6.20 depicts how the induced charge on the pixel would be affected by different amounts of Auger recombination. The induced charge on the pixel would nearly double if the auger recombination was the main process associated with hole trapping (each trapped hole leads to an auger electron) and is relatively constant over the entire thickness of the detector. The lower induced charge for interactions near the cathode was due to the fact the holes will reach and be collected by the cathode electrode, while the reduced induced charge near the anode was due to the weighting potential effects of the pixel anode.

As Auger recombination slowly reduces, as the model suggests, the induced charge on the pixel will decrease dramatically. Subsequently, a large shift in the photopeak position should be observed for pixelated anodes. However, that was not the case with current pixelated HgI_2 detectors, as the photopeak shift was only on the order of a few percent over several months for any measured pixel. In fact, very little change can be observed from the gamma-ray spectra shown in Figure 6.21. Thus, either Auger recombination was not a valid polarization model, or the process is very minor. Nonetheless, the measurements suggest that polarization may no longer be an important issue that needs to be overcome with current HgI_2 detectors using pixelated anodes.

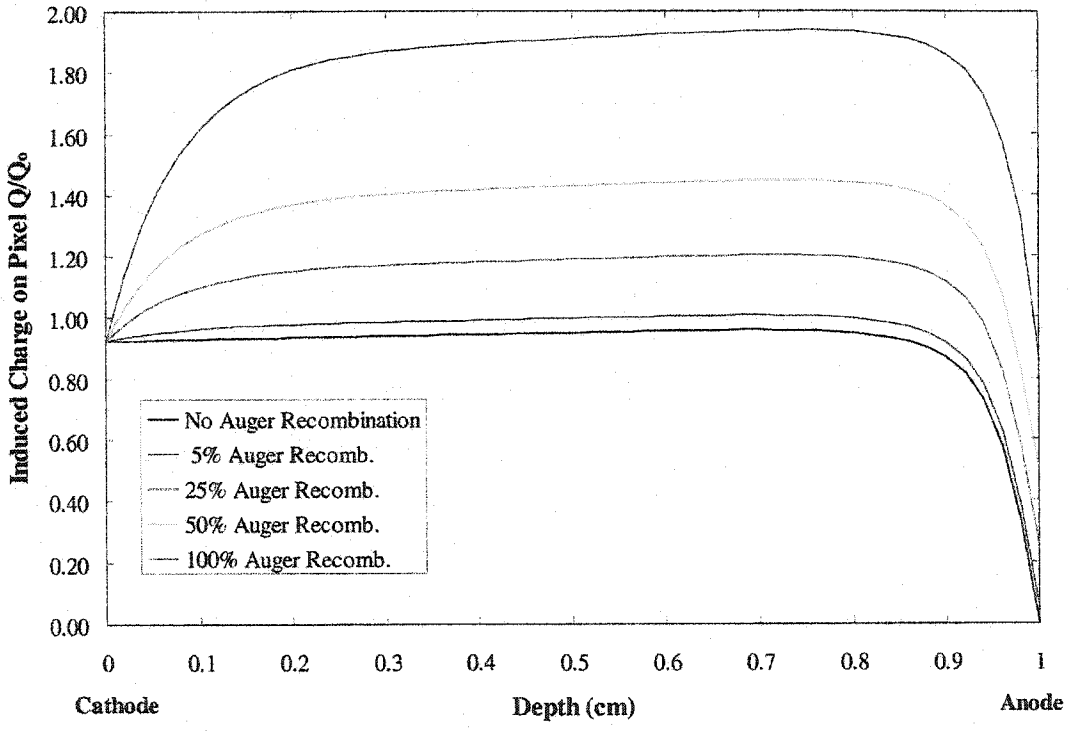

Figure 6.20: The effect of Auger recombination should cause a very large pulse shift over a large portion of the pixel volume.

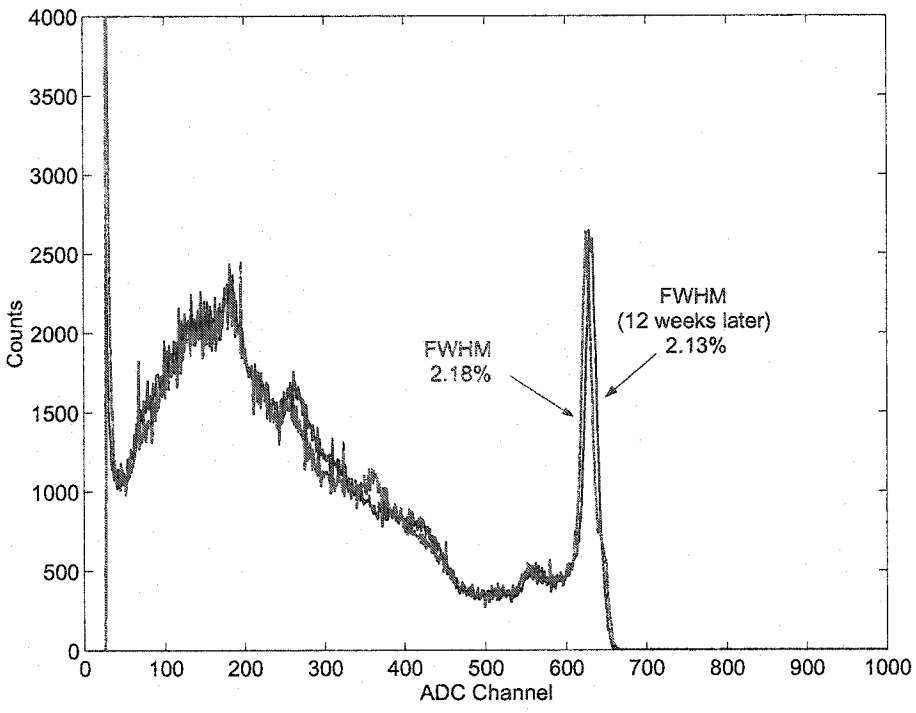

Figure 6.21: Cs-137 Spectra from Pixel *No.*1 on the first day it was measured (25 days after biasing) and 3 months later. There was very little change in the spectra, once again demonstrating that current pixelated HgI_2 detectors can be stable over several months of operation.

Chapter 7

CONCLUSIONS AND FUTURE WORK

7.1 Modeling Results

Simulation models using GEANT have been created to model gamma-ray interactions in a HgI_2 detector. Several parameters can be changed to generate spectra from HgI_2 detectors. The effects of using pixelated anodes versus conventional planar electrodes showed that while the planar electrodes produced spectra from interactions in the entire detector thickness, the pixel anode generated spectra from interactions only within the volume directly underneath the pixel. The lack of hole movement inhibits planar electrode spectra from achieving a photopeak from a 662 keV monoenergetic gamma-ray source. The interactions of gamma-rays above a few hundred keV will occur throughout the detector, and the depth dependence of the signal will prevent the photopeak from being observed. One could use thin (sub-mm) HgI_2 detectors using conventional electrodes and observe a photopeak since the holes in this case can be collected. However, the detector efficiency will limit the use of thin detectors. Only for low energy gamma-rays, where the majority of interactions will occur near the cathode and only photoelectric events occur, will a photopeak be observed with thick (greater than 1 mm) HgI_2 detectors. If the Hecht relation is used, and hole movement accounted for, a strong photopeak cannot be realized even if the applied electric field is greater than 1000 V/mm. Pulse compensation cannot overcome the poor signal-to-noise ratio that would occur in a large portion of the detector and this correction technique will still yield a very broad photopeak.

Pixelated HgI_2 detectors, on the other hand, generate a signal that is relatively independent of the depth of interaction by requiring only electrons to induce charge

on the pixel electrode. The induced signal on the electrode is produced only near the pixel electrode itself. Thus, electron movement near the pixel will induce a large signal and this signal has only a slight dependence on the depth of interaction. The dependence has an inverse relationship with detector thickness. Therefore, it is advantageous to use pixelated anodes with thick HgI_2 detectors. Simulated gamma-ray spectra show that a pixel anode can yield a prominent photopeak. This photopeak can be observed at all detector biases. The efficiency for one anode pixel is obviously much lower than that for the planar detector since the effective volume of the pixel region was only 1% of the total volume of the detector. Once a fully pixelated HgI_2 detector is developed, the photopeak efficiency of this detector will be far superior to the conventional planar electrode detector of similar dimensions.

The efficiency of a fully-pixelated HgI_2 device was compared with a fully-pixelated CdZnTe detector of the same size using three electrode sizes. The simulations showed that a fully-pixelated HgI_2 detector that employs only single pixel photopeak events will be as efficient as a fully-pixelated CdZnTe detector that uses all photopeak events (single pixel and multiple pixel). Once a HgI_2 detector can use multiple pixel events to generate gamma-ray spectra, this detector material will hold a significant efficiency advantage over CdZnTe due to the increased effective atomic number of HgI_2. The photopeak efficiency using all single and multiple pixel events for mercuric iodide is approximately 20% versus only 8.6% for CdZnTe. For gamma-rays with energies higher than a few hundred keV, a 1 cm thick HgI_2 detector is equivalent to a 2-3 cm thick CdZnTe detector.

7.2 Experimental Results

Several HgI_2 detectors, each with four pixels, have been tested for their spectroscopic capabilities. 5 mm thick detectors yielded resolutions less than 3% for 6 of 8 pixels tested after incorporating depth sensing and correction. Without depth sensing the resolution of the 662 keV photopeak would have been quite poor, and more varied across each pixel on a single detector (in some cases the resolution was

greater than 20%). Once depth correction was incorporated the photopeak and the Hg x-ray escape photopeak could both be easily separated. A resolution of 1.61% was achieved on one pixel of a 5 mm thick detector that also yielded an energy resolution under 1% for one individual depth index.

1 cm thick detectors were also tested and showed even better spectroscopic results. Without depth correction, resolutions less than 5% were easily achieved, and in some cases the resolution was approximately 2% for the 662 keV gamma ray from Cs-137. In addition to the flatter weighting potential for the 1 cm thick HgI_2 detectors, electron trapping may have compensated for the small depth dependence of the weighting potential, producing a relatively uniform induced charge for all 662 keV photoelectric interactions across the entire thickness of the detector (with exception to the pitch depth). Depth correction further improved the photopeak resolution. The best measured resolution was 1.4% for a 1 cm thick HgI_2. It should be noted that without pixelated anodes and single polarity charge sensing, a photopeak from Cs-137 could not be achieved with a HgI_2 detector of this thickness. Several other pixels yield depth corrected resolutions better than 2%, as 8 of 11 pixels tested (one pixel did not have a signal) were able to reach this milestone. One pixel even showed a photopeak resolution less than 2% without depth correction, while several others showed resolutions less than 3% without depth correction. If slightly worse energy resolution is acceptable, the use of depth correction may not be necessary, making the potential system much easier to operate for the end user. These results were achieved using relatively modest shaping times (generally 4-8 μs) and using a low electric field (250 V/mm) compared with typical values used with HgI_2 employing conventional planar electrodes (24 μs or higher with an electric field of at least 1000 V/mm). The use of a low energy gamma-ray source (Am-241) shows that the entire thickness of the detector was active and used in the acquisition of spectra. These detectors can also be used in cases where multiple gamma-ray lines can be observed and depth correction will improve the spectrum across all energies. However, the gap between electrodes needs to remain relatively small, as one 1 cm thick detector showed increase charge

sharing, Compton continuum, and slightly degraded resolution due to in part the 500 micron wide gap between the pixel region and the large surrounding anode.

The measurements of charge transportation properties of mercuric iodide detectors showed that there can be significant variation in electron transport across a single detector. The $(\mu\tau)_e$ product was calculated by comparing the peak centroids obtained from each pixel at different cathode biases. Values on the order of 10^{-3} cm^2/V were obtained for several pixels. These values were generally higher than those found in literature and may have been the result of better detector crystal growth and fabrication techniques. The results also showed that $(\mu\tau)_e$ can vary by close to an order of magnitude across a single detector. This may help explain why HgI_2 detectors cannot perform well spectroscopically when coplanar anodes are employed. The use of both high and low energy gamma-rays showed that it may be possible to use any gamma-ray energy can be used to measure $(\mu\tau)_e$, so long as depth sensing can be used to determine the interaction location. An assessment of hole transportation properties was also performed and revealed that hole transport is much worse than that for electrons. The mobility and lifetime for holes were each an order of magnitude lower than those for electrons and the values were consistent with previous studies. Eliminating the need to collect holes (single polarity charge sensing) is the only way thick HgI_2 detectors can be used to produce good spectral resolution.

Pixelated HgI_2 detectors were also tested for the ability to operate over the course of several months without any degradation in response. After a small amount of polarization (observed as a shift in the photopeak position) during the first couple of days the detector was biased, the pixelated HgI_2 detector operated well over the entire measurement time. The peak position and resolution remained relatively constant for all three pixels that were measured. One pixel (pixel No. 4 of detector 93203N98) suffered from a reduced photopeak count rate with time, suggesting the effective volume of the pixel was changing. This pixel suffered from a wide gap between the pixel and surrounding anode, and was adjacent to the non-working pixel. The other two pixels each had a count rate that remained

stable throughout the measurement period. In addition to charge transportation and trapping measurements, pixelated HgI_2 using depth sensing and single polarity charge sensing can be used to study many characteristics of detector physics, such as polarization models. A previously proposed model for polarization, Auger recombination, has been evaluated and shown not to be applicable to current pixelated HgI_2 detectors, possibly due to improvements in the growth and manufacturing of the detector material. In fact, polarization was, at most, only a small factor that can be accounted for in pixelated HgI_2.

7.3 Suggested Future Work

The future objectives for pixelated HgI_2 should be aimed towards the development of fully-functional 3-D detectors that can be used for high resolution, high efficiency gamma-ray spectroscopy. Thus, much of the future work suggested here is focused on achieving a 1 cm thick, fully-pixelated HgI_2 detector.

While the detector packaging was acceptable for the work presented here, several improvements are required to increase the rigidity of the detector. This will enable the pixelated HgI_2 to be handled in a more rugged manner. The current anode lead wires are very long, run down the sides of the detector, and are glued onto the ceramic substrate near the cathode. This is not ideal because the lead wires are very thin and therefore fragile. Several wires have broken throughout the use of several detectors, usually at the glue point on the ceramic substrate. In addition, at higher detector biases, the signals from the pixels seemed to suffer from breakdown, noted as a large voltage spike (saturating the preamp at 6 V) and as severe crosstalk between the cathode and pixel. This breakdown may have occurred next to the cathode or from breakdown at the sides of the detector crystal. Moving the lead wires away from the sides of the detector and not gluing them next to the cathode, should remove these breakdown events.

While the results obtained in the work showed a marked improvement over conventional HgI_2 gamma-ray spectrometers, the detectors were not operated at an ideal applied electric field. Generally, other work with HgI_2 used an electric

field around 500-1000 V/mm. Thus, the applied bias should be increased from 2-2.5 kV to 5-10 kV. Increasing the detector bias will decrease the electron drift time. Subsequently, shorter shaping times could be used with the associated electronics, allowing for faster processing of the signals. This in turn could allow for the analysis of highly radioactive materials. In addition, increasing the detector bias will reduce the amount of electron trapping and charge sharing that degrade the anode pixel signal. The reduction of these effects should improve the overall photopeak resolution by improving the S/N ratio and reducing tailing effects on the low-energy side of the photopeak.

Engineering efforts should be made towards improving the structure of the anode pixels. Several pixels and detectors suffered from a very wide gap between anode electrodes, particularly between the pixels and large surrounding anode. Keeping the pixel gap small (approximately 150 μm) should help suppress charge sharing events by reducing the number of inter-pixel gamma-ray interactions.

The primary focus of the work was single-pixel events within the detectors. In order to accomplish the large photopeak efficiency advantage over pixelated CdZnTe detectors, the incorporation of multiple pixel events is required. Spectra can then be collected from multiple pixel interactions, which is key to significantly improving efficiency of the pixelated detectors. Measuring-multiple pixel interactions can also improve the single pixel event spectra by suppressing the Compton continuum through coincidence measurements.

In addition to gamma-ray spectroscopy applications, it would be interesting to investigate the use of pixelated HgI_2 detectors as a thermal neutron detector. HgI_2 has an appreciable thermal neutron cross section (approximately 370 b) and the capture with Hg-199 leads to a (n,γ) reaction yielding a 368 keV gamma-ray. This gamma-ray can then be detected by absorption in the detector. The superior energy resolution of pixelated anodes over conventional planar electrodes will allow for a more accurate determination of this peak from neutron capture from other gamma-ray sources.

Finally, in order to use a fully pixelated HgI_2 detectors, the discrete electronics

used in this work cannot be used. If a large array of pixels is to be read simultaneously, size and power constraints will prohibit the use of discrete electronics. Thus, an application-specific integrated circuit (ASIC) needs to be developed and incorporated into the detection system. Fortunately, ASICs have been developed for pixelated CdZnTe that provide both depth sensing by measuring the C/A signal ratio and the timing of the signal. Thus, current ASICs will only need to be slightly modified to account for the lower mobility and longer pulse rise time for HgI_2 detectors. The slower rise of the HgI_2 signal could possibly lead to better position sensing than using the C/A signal ratio. All of the suggestions here should help in the development of thick HgI_2 detectors that can achieve gamma-ray energy resolutions near those of current pixelated CdZnTe detectors (far superior to conventional HgI_2 detectors), while providing a more efficient detector over CZT.

References

1. G. F. Knoll. *Radiation Detection and Measurement*. John Wiley and Sons, Inc., New York, third edition, 2000.

2. Y. Eisen. Current state-of-the-art industrial and research applications using room-temperature CdTe and CdZnTe solid state detectors. *Nuclear Instruments and Methods in Physics Research A*, 380:431–439, 1996.

3. K. Hitomi, T. Murayama, T. Shoji, T. Suehiro, and Y. Hiratate. Improved spectrometric characteristics of thallium bromide radiation detectors. *Nuclear Instruments and Methods in Physics Research A*, 428:372–378, 1999.

4. M. Cuzin. Some new developments in the field of highg atomic number materials. *Nuclear Instruments and Methods in Physics Research A*, 253:407–417, 1987.

5. Shin Watanabe, Tadayuki Takahashi, Yuu Okada, Goro Sato, Manabu Kouda, Takefumi Mitani, Yoshihito Kobayashi, Kazuhiro Nakazawa, Yoshikatsu Kuroda, and Mitsunobu Onishi. CdTe stacked detectors for gamma-ray detection. *IEEE Transactions on Nuclear Science*, 49(3):1292–1296, 2002.

6. R. O. Bell, G. Entine, and H.B. Serreze. Time-dependent polarization of CdTe gamma-ray detectors. *Nuclear Instruments and Methodes in Physics Research*, 117:267–271, 1974.

7. P. Siffert, J. Berger, C. Scharager, A. Cornet, and R. Stuck. Polarization in cadmium telluride nuclear radiation detectors. *IEEE Transactions on Nuclear Science*, 23(1):159–170, February 1976.

8. J. F. Butler, C. L. Lingren, and F. P. Doty. $Cd_{1-x}Zn_xTe$ gamma-ray detectors. *IEEE Transactions on Nuclear Science*, 39:605–609, August 1992.

9. T. Mohammed-Brahim, A. Friant, and J. Mellet. Structure mis effects on polarization of HgI_2 crystals used for /*gamma*-ray detection. *IEEE Transactions on Nuclear Science*, 32:581–584, February 1985.

10. L. T. Jones and P. B. Woollam. Resolution improvement in CdTe gamma detectors using pulse-shape discrimination. *Nuclear Instruments and Methodes in Physics Research*, 124:591–595, 1975.

11. A. Beyerle, V. Gerrish, and K. Hull. Parallel pulse processing for mercuric iodide gamma-ray detectors. *Nuclear Instruments and Methods in Physics Research A*, 242:443–449, 1986.

12. Vern M. Gerrish, Derek J. Williams, and Albert G. Beyerle. Pulse filtering for thick mercuric iodide detectors. *IEEE Transactions on Nuclear Science*, 34:85–90, February 1987.

13. P. Olmos, G. Garcia-Belmonte, and J. M. Perez. Large volume HgI_2 counters: a novel technique for pulse discrimination. *Nuclear Instruments and Methods in Physics Research A*, 322:557–561, 1992.

14. O. Frisch. *British Atomic Energy Report*. Br-49, 1944.

15. P. N. Luke. Unipolar charge sensing with coplanar electrodes – application to semiconductor detectors. *IEEE Transactions on Nuclear Science*, 43(4):207–213, August 1995.

16. P. N. Luke and E. E. Eissler. Performance of CdZnTe coplanar-grid gamma-ray detectors. *IEEE Transactions on Nuclear Science*, 43(3):1481–1486, June 1996.

17. H. H. Barrett, J. D. Eskin, and H. B. Barber. Charge transport in arrays of semiconductor gamma-ray detectors. *Physical Review Letters*, 75(1):156–159, 1995.

18. W. Li, Z. He, G. F. Knoll, D. K. Wehe, and J. E. Berry. Spatial variation of energy resolution in 3-D position sensitive CZT gamma-ray spectrometers. *IEEE Transactions on Nuclear Science*, 46(3):187–192, June 1999.

19. M. Hage-Ali, J. M. Koebel, R. Régal, P. Siffert, V. Prat, and H. Simon. Cadmium telluride small probes for gamma-ray spectrometry. *Nuclear Instruments and Methods in Physics Research A*, 380:427–430, 1996.

20. D. S. McGregor, Z. He, H. A. Seifert, R. A. Rojeski, and D. K. Wehe. CdZnTe semiconductor parallel strip Frisch grid radiation detectors. *IEEE Transactions on Nuclear Science*, 45(3):443–449, June 1998.

21. D. S. McGregor, R. A. Rojeski, Z. He, D. K. Wehe, M. Driver, and M. Blakely. Geometrically weighted semiconductor Frisch grid radiation spectrometers. *Nuclear Instruments and Methods in Physics Research A*, 422:164–168, 1999.

22. K. Parnham, J. B. Glick, Cs. Szeles, and K. G. Lynn. Performance improvement of CdZnTe detectors using modified two-terminal electrode geometry. *Journal of Crystal Growth*, 214:1152–1154, 2000.

23. A. Shor, Y. Eisen, and I. Mardor. Spectroscopy with CdZnTe γ- and x-ray detector by modifying the electron trapping to compensate for incomplete charge collection caused by large hole trapping. *Nuclear Instruments and Methods in Physics Research A*, 426:491–496, 1999.

24. Zhong He, Glenn F. Knoll, David K. Wehe, Ronald Rojeski, Carlos H. Mastrangelo, Mark Hammig, Carla Barrett, and Akira Uritani. 1-D position sensitive single carrier semiconductor detectors. *Nuclear Instruments and Methods in Physics Research A*, 380:228–231, 1996.

25. Z. He, G. F. Knoll, D. K. Wehe, and J. Miyamoto. Position-sensitive single carrier CdZnTe detectors. *Nuclear Instruments and Methods in Physics Research A*, 388:180–185, 1997.

26. M. Amman, P. N. Luke, and J. S. Lee. CdZnTe material uniformity and coplanar-grid gamma-ray detector performance. *IEEE Transactions on Nuclear Science*, 47(3):760–767, June 2000.

27. Z. He, W. Li, G. F. Knoll, D. K. Wehe, J. Berry, and C. M. Stahle. 3-D position sensitive CdZnTe gamma-ray spectrometers. *Nuclear Instruments and Methods in Physics Research A*, 422:173–178, 1999.

28. Wen Li. *Three-Dimensional Position Sensitive CdZnTe Gamma Ray Spectrometers*. PhD thesis, University of Michigan, 2001.

29. A. Holzer and M. Schieber. Reduction of polarization in mercuric iodide nuclear radiation detectors. *IEEE Transactions on Nuclear Science*, 27:266–271, February 1980.

30. Vernon Gerrish. Polarization and gain in mercuric iodide gamma-ray spectrometers. *Nuclear Instruments and Methods in Physics Research A*, 322:402–413, 1992.

31. W. R. Willig. Mercury iodide as a gamma spectrometer. *Nuclear Instruments and Methodes in Physics Research*, 96:615–616, 1971.

32. K. Hull, A. Beyerle, B. Lopez, J. Markakis, C. Ortale, W. Schnepple, and L. van den Berg. Recent developments in thick mercuric iodide spectrometers. *IEEE Transactions on Nuclear Science*, 30:402–404, February 1983.

33. S. P. Swierkowski, G. A. Armantrout, and R. Wichner. High-resolution HgI_2 x-ray spectrometers. *Applied Physics Letters*, 23:281–282, September 1973.

34. Andrzej J. Dabrowski, Jan S. Iwanczyk, Jeffrey B. Barton, Richard Whited Gerald C. Huth, Carol Ortale, Thanasis E. Economou, and Anthony L. Turkevich. Performance of room temperature mercuric iodide (HgI_2) detectors in the ultralow-energy x-ray region. *IEEE Transactions on Nuclear Science*, 28:536–540, February 1981.

35. M. Schieber, I. Beinglass, G. Dishon, A. Holzer, and G. Yaron. State-of-the-art of crystal growth and nuclear spectroscopic evaluation of mercuric iodide radiation detectors. *Nuclear Instruments and Methodes in Physics Research*, 150:71–77, 1978.

36. P. Olmos, G. Garcia-Belmonte, J. M. Perez, and J. C. Diaz. Use of thick HgI_2 detectors as intelligent spectrometers. *Nuclear Instruments and Methods in Physics Research A*, 299:45–50, 1990.

37. B. E. Patt, A. Del Duca, R. Dolin, and C. Ortale. Mercuric iodide x-ray camera. *IEEE Transactions on Nuclear Science*, 33:523–526, February 1986.

38. B. E. Patt, J. S. Iwanczyk, Y. J. Wang, M. P. Tornai, C. S. Levin, and E. J. Hoffman. Mercuric iodide photodetector arrays for gamma-ray imaging. *Nuclear Instruments and Methods in Physics Research A*, 380:295–300, 1996.

39. F. D. Becchetti, R. S. Raymond, R. A. Ristinen, W. F. Schnepple, and C. Ortale. Mercuric iodide (HgI_2) semiconductor devices as charged particle detectors. *Nuclear Instruments and Methodes in Physics Research*, 213:127–132, 1983.

40. Albert G. Beyerle and Kenneth L. Hull. Neutron detection with mercuric iodide detectors. *Nuclear Instruments and Methods in Physics Research A*, 256:377–380, 1987.

41. J. P. Ponpon, R. Stuck, P. Siffert, B. Meyer, and C. Schwab. Properties of vapour phase grown mercuric iodide single crystal detectors. *IEEE Transactions on Nuclear Science*, 22:182–191, February 1975.

42. M. Schieber, W. F. Schnepple, and L. van den Berg. Vapor growth of HgI_2 by periodic source or crystal temperature oscillation. *Journal of Crystal Growth*, 33:125–135, 1976.

43. Vernon Gerrish and Ludewijk van den Berg. Improved yield of high resolution mercuric iodide gamma-ray spectrometers. *Nuclear Instruments and Methods in Physics Research A*, 299:41–44, 1990.

44. L. van den Berg. Recent developments in mercuric iodide technology at EG&G Energy Measurements, Inc., Santa Barbara Operations. *Nuclear Instruments and Methods in Physics Research A*, 322:453–456, 1992.

45. A. Burger, D. Nason, L. van den Berg, and M. Schieber. *Growth of Mercuric Iodide*, volume 43 of *Semiconductors and Semimetals*, pages 85–110. Academic Press, San Diego, 1995.

46. H. Hermon, M. Roth, and M. Schieber. Improved technique for HgI_2 crystal growth. *Nuclear Instruments and Methods in Physics Research A*, 322:432–434, 1992.

47. A. Friant, J. Mellet, C. Saliou, and T. Mohammed Brahim. HgI_2 detectors from solution grown crystals. *IEEE Transactions on Nuclear Science*, 27:281–285, February 1980.

48. I. F. Nicolau and J. P. Joly. Solution growth of sparingly soluble single crystals from soluble complexes. *Journal of Crystal Growth*, 48:61–73, 1980.

49. Samuel P. Faile, Andrzej J. Dabrowski, Gerald C. Huth, and Jan S. Iwanczyk. Mercuric iodide (HgI_2) platelets for x-ray spectroscopy produced by polymer controlled growth. *Journal of Crystal Growth*, 50:752–756, 1980.

50. Weitang Li, Zhenghui Li, Shifu Zhu, Shujun Yin, Beijun Zhao, and Guanxiong Chen. Improved method for HgI_2 crystal growth and detector fabrication. *Nuclear Instruments and Methods in Physics Research A*, 370:435–437, 1996.

51. M. Schieber. Fabrication of HgI_2 nuclear detectors. *Nuclear Instruments and Methodes in Physics Research*, 144:469–477, 1977.

52. M. Schieber, A. Zuck, S. Sanguinetti, M. Montalti, M. Braiman, L. Melekhov, J. Nissenbaum, E. Grilli, M. Guzzi, R. Turchetta, W. Dulinski, D. Husson, and J. L. Riester. Characterization studies of purified HgI_2 precursors. *Nuclear Instruments and Methods in Physics Research A*, 428:25–29, 1999.

53. Eilene S. Cross, George Buffleben, Ed Soria, Ralph James, Michael Schieber, Raj Natarajan, and Vern Gerrish. The effect of elemental and hydrocarbon impurities on mercuric iodide gamma ray detector performance. *Nuclear Instruments and Methods in Physics Research A*, 380:23–25, 1996.

54. K.-T. Chen, L. Salary, A. Burger, E. Soria, A. Antolak, and R. B. James. Chemical analysis of metal impurity distribution of zone-refined mercuric iodide by ICP-AES and DSC. *Nuclear Instruments and Methods in Physics Research A*, 380:53–57, 1996.

55. J. P. Ponpon, M. Amann, and M. Sieskind. Influence of water and water vapour on the characteristics of KI treated HgI_2 detectors. *Nuclear Instruments and Methods in Physics Research A*, 412:104–108, 1998.

56. L. van den Berg. Growth of single crystals of mercuric iodide on the ground and in space. In *Semiconducotrs for Room-Temperature Radiation Detector Applications*, volume 302, pages 73–78. Materials Research Society, 1993.

57. Y. F. Nicolau and M. Dupuy. Study of */alpha*-HgI_2 crystals grown in space by differential scanning calorimetry, scanning cathodoluminescence microscopy and optical microscopy. *Nuclear Instruments and Methods in Physics Research A*, 283:355–362, 1989.

58. L. van den Berg and W. F. Schnepple. Mercuric iodide crystal growth in space. *Nuclear Instruments and Methods in Physics Research A*, 283:335–338, 1989.

59. Ronald S. Scott and George E. Fredericks. Evaporative degradation of HgI_2 x-ray detectors. *Applied Physics Letters*, 27:99–100, July 1975.

60. J. S. Iwanczyk, Y. J. Wang, J. G. Bradley, A. L. Albee, and W. F. Schnepple. Advances in the development of encapsulants for mercuric iodide x-ray detectors. *IEEE Transactions on Nuclear Science*, 37:2214–2218, December 1990.

61. M. R. Squillante, K. S. Shah, and L. Moy. Stabilization of HgI_2 x-ray detectors. *Nuclear Instruments and Methods in Physics Research A*, 288:79–81, 1990.

62. C. Ortale, L. Padgett, and W. F. Schepppple. Mercuric iodide imaging detectors. *Nuclear Instruments and Methodes in Physics Research*, 213:95–101, 1983.

63. Bradley E. Patt, Jan S. Iwanczyk, Martin P. Tornai, Craig S. Levin, and Edward J. Hoffman. Development of a mercuric iodide detector array for medical imaging applications. *Nuclear Instruments and Methods in Physics Research A*, 366:173–182, 1995.

64. J. S. Iwanczyk, B. E. Patt, Y. J. Wang, M. Croft, Z. Kalman, and W. Mayo. Mercuric iodide detector systems for identifying substances by x-ray energy dispersive diffraction. *IEEE Transactions on Nuclear Science*, 42:606–610, August 1995.

65. Y. J. Wang, J. S. Iwanczyk, and W. R. Graham. Evaluation of HgI_2 detectors for lead detection in paint. *IEEE Transactions on Nuclear Science*, 40:846–850, August 1993.

66. T. E. Economou, J. S. Iwaczyk, and R. Rieder. A HgI_2 x-ray instrument for the Soviet Mars '94 mission. *Nuclear Instruments and Methods in Physics Research A*, 322:633–638, 1992.

67. J. S. Iwanczyk, Y. J. Wang, N. Dorri, A. J. Dabrowski, T. E. Economou, and A. L. Turkevich. Use of mercuric iodide x-ray detectors with alpha backscattering spectrometers for space applications. *IEEE Transactions on Nuclear Science*, 38:574–579, April 1991.

68. G. R. Ricker, J. V. Vallerga, and D. R. Wood. A mercuric iodide detector system for x-ray astronomy. *Nuclear Instruments and Methodes in Physics Research*, 213:133–154, 1983.

69. Alain Friant, Jena Mellet, Gérard Barrandon, and Etienne Csakvary. HgI_2 detector for Pu contamination monitoring and radiological protection measurements. *Nuclear Instruments and Methods in Physics Research A*, 283:227–231, 1989.

70. C. Manfredotti. Dosimetry with HgI_2. *Nuclear Instruments and Methodes in Physics Research*, 225:173–178, 1984.

71. S. Caine, A. Holzer, I. Beinglass, M. Schieber, and E. Lowenthal. Fabrication and evaluation of HgI_2 miniature probes for in-vivo medical applications. *IEEE Transactions on Nuclear Science*, 25:649–652, February 1978.

72. J. S. Iwanczyk, J. B. Barton, A. J. Dabrowski, J. H. Kusmiss, and W. M. Szymczyk. A novel radiation detector consisting of an HgI_2 photodetector coupled to a scintillator. *IEEE Transactions on Nuclear Science*, 30:363–367, February 1983.

73. Y. J. Wang, B. E. Patt, and J. S. Iwanczyk. High efficiency CsI(Tl)/HgI_2 gamma ray spectrometers. *IEEE Transactions on Nuclear Science*, 42:601–605, August 1995.

74. Y. J. Wang, B. E. Patt, and J. S. Iwanczyk. Detector optimization for hand-held CsI(Tl)/HgI_2 gamma-ray scintillation spectrometers applications. *IEEE Transactions on Nuclear Science*, 43:1277–1281, June 1996.

75. M. Dahlbon, M. A. Mandelkern, E. J. Hoffman, A. R. Ricci, and J. B. Barton. Hybrid mercuric iodide (HgI_2) - gadolinium orthosilicate (GSO) detector for PET. *IEEE Transactions on Nuclear Science*, 32:533–537, February 1985.

76. M. Schieber, A. Zuck, L. Melekov, J. Nissenbaum, R. Turchetta, W. Dulinski, D. Husson, and J. L. Riester. Radiation-hard polycrystalline mercuric iodide semiconductor particle counters. *Nuclear Instruments and Methods in Physics Research A*, 410:107–110, 1998.

77. U. N. Roy, Y. Cui, G. Wright, C. Barnett, A. Burger, L. A. Franks, and Z. W. Bell. Polycrystalline mercuric iodide films: deposition, properties and detector performance. *IEEE Transactions on Nuclear Science*, 49:1965–1967, August 2002.

78. W. Shockley. Currents to conductors induced by a moving point charge. *Journal of Applied Physics*, 9:635–636, October 1938.

79. S. Ramo. Currents induced by electric motion. *Proceedings of the I.R.E.*, page 584, September 1939.

80. Z. He. Potential distribution within semiconductor detectors using coplanar grid electrodes. *Nuclear Instruments and Methods in Physics Research A*, 365:572–575, 1995.

81. K. Hecht. Zum mechanismus des lichtelektrischen primarstromes in isolierenden kristallen. *Z. Phys.*, 77:235, 1932.

82. P. N. Luke. Single-polarity charge sensing in ionization detectors using coplanar electrodes. *Applied Physics Letters*, 65(22):2884–2886, 1994.

83. Clair Sullivan. *Single Polarity Charge Sensing in High Pressure Xenon Using a Coplanar Anode Configuration*. PhD thesis, University of Michigan, 2002.

84. Zhong He. Review of the Shockley-Ramo theorem and its applications in semiconductor gamma-ray detectors. *Nuclear Instruments and Methods in Physics Research A*, 365:250–267, 2001.

85. Z. He, G. F. Knoll, and D. K. Wehe. Direct measurement of product of the electron mobility and mean free drift time of CdZnTe semiconductors using position sensitive single polarity charge sensing detectors. *Journal of Applied Physics*, 84(10):5566–5569, November 1998.

86. James E. Baciak and Zhong He. Spectroscopy on thick HgI_2 detectors: A comparison between planar and pixelated electrodes. *IEEE Transactions on Nuclear Science*, 50(4):1220–1224, August 2003.

87. European Organization for Nuclear Research, CERN, CH-1211, Geneve, 23, Switzerland.

88. J. W. Jerome. *Analysis of Charge Transport*. Springer, Verlag Berlin Heidelberg, 1996.

89. Constellatoin Technology Corporation, 7887 Bryan Dairy Road, Suite 100, Largo, Florida 33777.

90. Amptek Inc., 6 De Angelo Drive, Bedford, Massachusetts 01730.

91. National Instruments Corporation, 11500 North Mopac Expressway, Austin, Texas 78759.

92. Z. He and R. D. Vigil. Investigation of pixelated HgI_2 γ-ray spectrometers. *Nuclear Instruments and Methods in Physics Research A*, 492:387–401, October 2002.

93. F. V. Wald and G. Entine. Crystal growth of CdTe for γ-ray detectors. *Nuclear Instruments and Methodes in Physics Research*, 150:13–24, 1978.

94. G. Ramunno, E. Caroli, G. De Cesare, A. Donati, W. Dusi, D. Grassi, P. Chirco, P. Siffert, M. Amann, and J. M. Koebel. Investigation of the behaviour of a mercuric iodide detector under unusual irradiation conditions. *Nuclear Instruments and Methods in Physics Research A*, 380:223–227, 1996.

95. M. Schieber, A. Zuck, M. Braiman, J. Nissenbaum, R. Turchetta, W. Dulinski, D. Husson, and J. L. Riester. Novel mercuric iodide polycrystalline nuclear particle counters. *IEEE Transactions on Nuclear Science*, 44:2571–2575, December 1997.

96. J. S. Iwanczyk, N. Dorri, M. Wang, R. W. Szczebiot, A. J. Dabrowski, B. Hedman, K. O. Hodgson, and B. E. Patt. 20-element HgI_2 energy dispersive x-ray array detector system. *IEEE Transactions on Nuclear Science*, 39:1275–1280, October 1992.